

**Rheinische Friedrich-Wilhelms-Universität,
Bonn**

Math.-Nat.-Fakultät, Fachgruppe Physik/Astronomie

Clumpy Dust Tori in Active Galactic Nuclei

Inaugural-Dissertation

zur Erlangung des Doktorgrads (Doctor rerum naturalis)

Sebastian Florian Hönig

aus

Schwäbisch Gmünd, Deutschland

Januar 2008

Diese Arbeit wurde angefertigt mit Genehmigung der
Mathematisch-Naturwissenschaftlichen Fakultät der
Rheinische Friedrich-Wilhelms-Universität, Bonn

Gutachter: Prof. Dr. Gerd Weigelt¹
Prof. Dr. Pavel Kroupa²

¹ Max-Planck-Institut für Radioastronomie, Bonn

² Argelander-Institut für Astronomie, Bonn

Tag der mündlichen Prüfung: 24. Januar 2008

Diese Dissertation ist auf dem Hochschulschriftenserver der ULB Bonn
http://hss.ulb.uni-bonn.de/diss_online elektronisch publiziert.

Clumpy Dust Tori in Active Galactic Nuclei

Dissertation by Sebastian F. Hönig

© Sebastian F. Hönig, Bonn 2007
All rights reserved.

dedicated to my parents

Clumpy Dust Tori in Active Galactic Nuclei

Sebastian F. Hönig

ABSTRACT

Active Galactic Nuclei (AGN) are amongst the most luminous objects in the universe. The source of their activity is accretion onto a supermassive black hole in the center of the galactic nucleus. The various phenomena observed in AGN are explained in a common unification scheme. The cornerstone of this unification scheme of AGN is the presence of an optically and geometrically thick dust torus which surrounds the central accretion disk and broad-line region (BLR). This parsec-scaled torus is responsible for the apparent difference between type 1 and type 2 AGN. If the line-of-sight intersects with the torus, the accretion disk and BLR are not visible and the AGN is classified as a type 2 object. On the other hand, if the torus is seen nearly face-on, the accretion disk and BLR are directly exposed to the observer, so that the galaxy appears as a type 1 AGN.

Near- (NIR) and mid-infrared (MIR) interferometry has resolved, for the first time, the dust torus around the nearby prototypical Seyfert 2 AGN NGC 1068. These observations provided an insight into the structure of the torus: Apparently, the dust is not smoothly distributed in the torus but arranged in clumps — contrary to what has been commonly used in models.

We developed a new radiative transfer model of clumpy dust tori which is a key tool to interpret NIR and MIR observations of AGN. The model accounts for the 3-dimensional arrangement of dust clouds. Model SEDs and images can be obtained for a number of different physical parameters (e.g., radial and vertical dust density distribution, cloud radii, optical depths, etc.). It was shown that the model SEDs are in agreement with observed spectral properties. Moreover, we applied our new model to the data of NGC 1068. It was possible, for the first time, to simultaneously reproduce NIR and MIR interferometry and photometry of the nucleus of NGC 1068. In particular, the model follows the trend of the deeper $9.7\mu\text{m}$ silicate absorption features in the correlated fluxes than in the total fluxes, as observed with VLTI/MIDI in the $8 - 13\mu\text{m}$ band. Comparison with the NGC 1068 multi-wavelength SED from Radio to the infrared shows that most of the unresolved MIR flux comes from thermal dust emission inside the torus, while in the NIR a possible synchrotron source or the accretion disk might be seen through “holes” in the clumpy torus.

To get a better idea how much the accretion disk contributes to the NIR emission of AGN, we studied NIR colors of a sample of type 1 AGN which were observed in J -, H -, and K -band with HST/NICMOS. By comparing the observed colors with those expected from torus models, we found out that the accretion disk contributes typically $< 25\%$ to the K -band flux. The observed colors also indicate that the sublimation temperature is probably close to $\sim 1500\text{K}$, but not significantly higher. In addition, reverberation radii of type 1 AGN were compared to theoretical predictions for the dust sublimation radius. Apparently, the reverberation radii are about a factor of 3 smaller than the expected sublimation radius for standard ISM dust grains. This discrepancy can be solved if the inner torus region is dominated by large carbon grains.

We studied the feedback of AGN radiation on the dust torus. It was found out that dust which is smoothly distributed cannot withstand the radiation pressure from the AGN. On the other hand, self-gravitating clouds in clumpy tori can efficiently compensate the AGN radiation pressure. A physically-motivated clumpy torus model was used to study the impact of the AGN radiation on obscuration properties of the torus. We showed that below an AGN luminosity of $\sim 10^{42} \text{ erg s}^{-1}$, the associated low accretion rates can no longer support an obscuring torus. In the high-luminosity regime, large clouds become unbound so that the torus is dominated by smaller clouds. As a result, the covering factor and apparent scale height decrease with luminosity, so that the fraction of type 1 AGN should become larger at higher luminosities (and high radiative efficiencies). This picture offers a physical explanation for the long-standing “receding torus” phenomenon.

One of the major astronomical discoveries within the last year was the identification of type 2 counterparts of QSOs. These objects were the “missing link” in the unification scheme. We studied restframe optical-to-MIR SEDs of a sample of 21 obscured QSOs with our clumpy torus model. It was found out that the observed SEDs favor models with compact geometries and, apparently, no flaring. In some objects, the combination of blue NIR color and very deep silicate absorption is in contradiction to expectations from torus models. We propose that in such cases, the torus is actually seen face-on, and a detached cold absorber in the host galaxy (e.g., a dust lane or cloud) is responsible for the deep silicate absorption feature. According to this picture, some of the obscured QSOs are mimicking type 2 AGN although their torus orientation might be similar to a type 1 AGN.

Contents

1	Introduction	1
1.1	Seyfert galaxies	1
1.2	The source of energy in active galaxies	3
1.3	Unification Scheme of AGN	3
1.4	The dusty torus	5
1.4.1	The dust content and its spectral signatures	5
1.4.2	Obscuration in the X-rays	6
1.4.3	Geometrical thickness	6
1.4.4	The size of the torus	6
1.4.5	Direct imaging of the torus	8
1.5	Torus models	8
1.5.1	Smooth dust models	8
1.5.2	Clumpy torus models	10
1.5.3	Alternative models	10
1.6	Interferometry of AGN dust tori	10
1.7	Open questions and outline of the thesis	13
2	A Three-Dimensional Radiative Transfer Model of Clumpy Dust Tori	15
2.1	Overview and Context	15
2.2	Monte Carlo simulation of individual dust clouds	16
2.2.1	AGN primary radiation	16
2.2.2	Geometry and properties of individual dust clouds	17
2.2.3	Radiative Transfer Code	17
2.2.4	Quality checks of Monte Carlo simulations	18
2.2.5	Cloud SEDs	20
2.3	Torus assembly	23
2.3.1	Torus parameters	23
2.3.2	Torus SED compilation and geometric peculiarities	24
2.3.3	Physical torus models and cloud properties	25
2.4	Results	26
2.4.1	Statistical cloud distribution	29
2.4.2	Radial Distribution function	30
2.4.3	The effect of flaring	30
2.4.4	The outer radius of the torus	33
2.5	Discussion and assessments of the method	33
2.5.1	Energy conservation	34

2.5.2	SED shape	35
2.5.3	Improved method	36
2.6	Summary and conclusions	37
3	NGC 1068 – the Seyfert 2 Prototype for Torus Studies	39
3.1	Overview and Context	39
3.2	Simultaneous modeling of the IR SED and IR visibilities of NGC 1068	42
3.3	Improvement of the visibility fit	46
3.4	Summary and Conclusions	50
4	A Multi-wavelength Analysis of the NGC 1068 SED	53
4.1	Introduction	53
4.2	Observations	54
4.3	Models	55
4.3.1	IR torus model	55
4.3.2	Radio models	56
4.4	The influence of the Radio components to the IR	58
4.5	Quantifying the contribution of the accretion disk	60
4.6	Summary and Conclusions	61
5	Dust Tori in Type 1 AGN	63
5.1	Overview and context	63
5.2	HST/NICMOS images and point source flux	64
5.2.1	Sample description and data reduction	64
5.2.2	Nuclear flux measurements	64
5.3	The spectral components of the NIR point sources	69
5.3.1	Hot dust emission and contribution from the putative accretion disk	69
5.3.2	The NIR colors of clumpy torus models	69
5.3.3	The NIR spectral shape of the big blue bump	72
5.3.4	Other components	72
5.4	The inner boundary of AGN tori	73
5.4.1	Dust sublimation radius	73
5.4.2	The near-IR reverberation radius	74
5.4.3	Implications	75
5.5	The NIR interferometry of Type 1 nuclei	77
5.5.1	Simulated interferometric observations	77
5.5.2	Comparison with existing measurements	79
5.6	Summary and conclusions	80
6	Clumpy Dust Tori at Low and High Luminosities	81
6.1	Overview and context	81
6.2	The Eddington limit for the torus	82
6.2.1	Smooth dust distribution	82
6.2.2	Clumpy dust torus	83
6.3	The torus at low AGN luminosities	85

6.4	The dust torus in the high luminosity regime	86
6.5	Mismatch between AGN type and X-ray obscuration	89
6.6	Summary and Conclusions	89
7	Dust Tori in Obscured QSOs	91
7.1	Introduction	91
7.1.1	Obscured AGN at high luminosities	91
7.1.2	The obscuring matter in AGN	91
7.2	Sample description	93
7.3	Observations and Data Analysis	95
7.3.1	Sample Data	95
7.3.2	Luminosities, redshift, and optical depth	98
7.4	Modeling the SEDs with clumpy torus models	98
7.4.1	Torus Models	98
7.4.2	Introducing a cold absorber	100
7.4.3	Model parameters	105
7.5	Composite IR spectra	108
7.6	X-ray properties	110
7.6.1	Available data	110
7.6.2	X-ray absorption and IR extinction	110
7.7	Obscuration at high luminosities	112
7.8	Summary and Conclusions	114
8	Summary of the thesis and outlook	117
A	Radiation in a Dusty Medium	121
A.1	Radiative Transfer Equations	121
A.2	Absorption and thermal re-emission of dust	121
	Bibliography	123

List of Tables

2.1	Temperature gradients in dust clouds	20
2.2	Torus model relations and parameters	23
2.3	Relations for parameters study	26
3.1	Photometric data for the nuclear region of NGC 1068 from high-resolution observations	43
3.2	Parameters of the NGC 1068 clumpy torus model	43
3.3	Comparison between observed interferometric and modeled torus sizes	44
4.1	High spatial resolution observations of the nuclear emission of NGC 1068 from the Radio to the infrared regime.	54
5.1	Radio-quiet Type 1 object sample	66
7.1	Optical and infrared data of the obscured QSOs sample	96
7.2	IRS Low resolution Spectroscopy Observation Log	97
7.3	Redshift, observed $6\mu\text{m}$ luminosity, and optical depths of our QSO2 sample.	99
7.4	Torus model parameters	106
7.5	X-ray properties of some of our sample objects.	111

List of Figures

1.1	Optical spectra of several AGN types	2
1.2	Unification Scheme of AGN	4
1.3	The nuclear environment of the Circinus galaxy in the NIR.	7
1.4	Geometry of smooth dust torus models.	9
1.5	Reconstructed K -band Speckle image of the NGC 1068 nucleus and the Radio jet.	11
1.6	K -band visibilities of NGC 1068.	12
2.1	Sketch of a clumpy torus	16

2.2	AGN source spectrum	17
2.3	Comparison of a hot-side cloud SED between <code>mcsim_mpi</code> and DUSTY	18
2.4	Temperature profile of a simulated dust cloud	19
2.5	SEDs of spherical dust clouds	21
2.6	Cloud model SEDs for unilluminated side	22
2.7	Inclination study of our torus model	27
2.8	L -band images of the clumpy torus	28
2.9	K -band image of torus with non-isotropic central radiation source	29
2.10	Torus model SEDs for different radial cloud distributions	31
2.11	Torus model SEDs for different flaring parameters	32
2.12	Torus model SEDs for two different outer radii.	33
3.1	Spectro-polarimetry of NGC 1068 at optical wavelengths	40
3.2	NGC 1068 in a nutshell	41
3.3	Comparison between the observed and modeled SED of NGC 1068	45
3.4	Comparison between the observed and modeled K -band visibilities	45
3.5	Comparison between the observed and modeled MIR visibilities	46
3.6	NGC 1068 model images of the clumpy torus model	47
3.7	Alternative model SED for NGC 1068.	48
3.8	Improved model fit to K and N -band visibilities of NGC 1068.	49
4.1	Multi-wavelength SED of NGC 1068 in comparison to a Synchrotron model.	57
4.2	Same as Fig. 4.1 but with a free-free emission model.	59
4.3	Accretion disk in NGC 1068 and its contribution to the IR SED.	61
5.1	Observed $J - H$ and $H - K$ colors for the Type 1 sample	67
5.2	PSF flux fraction in F160W filter image.	68
5.3	Color-Color diagram to determine the accretion disk fraction	71
5.4	Observed reverberation radii and expected sublimation radius in physical units	75
5.5	Observed reverberation radii and expected sublimation radius in angular sizes	76
5.6	Visibilities for type 1 objects at different accretion disk contribution fractions (1.2 mas ring)	78
5.7	Visibilities for type 1 objects at different accretion disk contribution fractions (0.4 mas ring)	78
6.1	Observed and expected type 1 AGN fraction	88
7.1	Observed and modeled SED of obscured QSO (torus-only models).	101
7.1	102
7.2	Rest-frame SEDs and best-fit torus models.	104
7.3	Comparison between observed and modeled optical depth.	107
7.4	Composite IR spectra for T and T+C models	109
7.5	Comparison between τ_{S_i} and N_H	112

8.1	Nuclear MIR spectrum of ESO 428–G14 as observed with <i>Spitzer</i> and VLT/VISIR	119
-----	---	-----

1. Introduction

*The diversity of the phenomena of Nature is so great,
and the treasures hidden in the heavens so rich,
precisely in order that the human mind shall
never be lacking in fresh nourishment.*

Johannes Kepler,
in *Mysterium Cosmographicum*

1.1. Seyfert galaxies

Among the large variety of galaxies, a certain class of objects with very luminous bolometric emission in their central regions ($\gtrsim 10^{42}$ erg s $^{-1}$) is outstanding. The first close investigation to identify and characterize these objects was done by Seyfert (1943). He found out that several galaxies show strong emission lines coming from their nuclear regions, which are not associated with stellar activity but ionized gas. In addition, these galactic nuclei are optically bright and starlike. Khachikian & Weedman (1974) studied a sample of 71 “Seyfert galaxies”. They found out that these galaxies can be separated into two groups:

Seyfert 2 galaxies show forbidden atomic lines and slightly broader Balmer lines, the latter having a width of approximately 500–1000 km/s. On the other hand, the line width of “normal” galaxies is usually not broader than ~ 200 km/s.

Seyfert 1 galaxies also show Balmer and forbidden lines as Seyfert 2 objects, but the Balmer lines have broad bases of several 1000 km/s line width. It was noted that from spectral properties, the Seyfert 1 objects seem to be scaled-down versions of Quasi-stellar objects (QSOs), which are very luminous galactic nuclei with luminosity $L_{\text{bol}} > 10^{45}$ erg s $^{-1}$.

Based on the relative strength of broad and narrow lines, Osterbrock (1981) introduced subgroups (originally 1.8, 1.9; now also 1.2, 1.5) which are considered as intermediate Seyfert types.

There are certain differences between Seyfert galaxies and normal galaxies. One important point is the [OIII]/H β -ratio. In Seyfert galaxies, this ratio is significantly higher than in other galaxies which points towards a different ionization mechanism in the Seyfert galaxies as compared to normal galaxies. Finally, Seyfert galaxies have strong UV excesses – often referred to as the “big blue bump”. It has been speculated if the origin of the UV excess is due to emission from hot stars (more likely in type 2 objects) or originates from other thermal or non-thermal processes (e.g., an accretion disk, as suggested for type 1 objects). The observed high UV/optical, IR, and X-ray

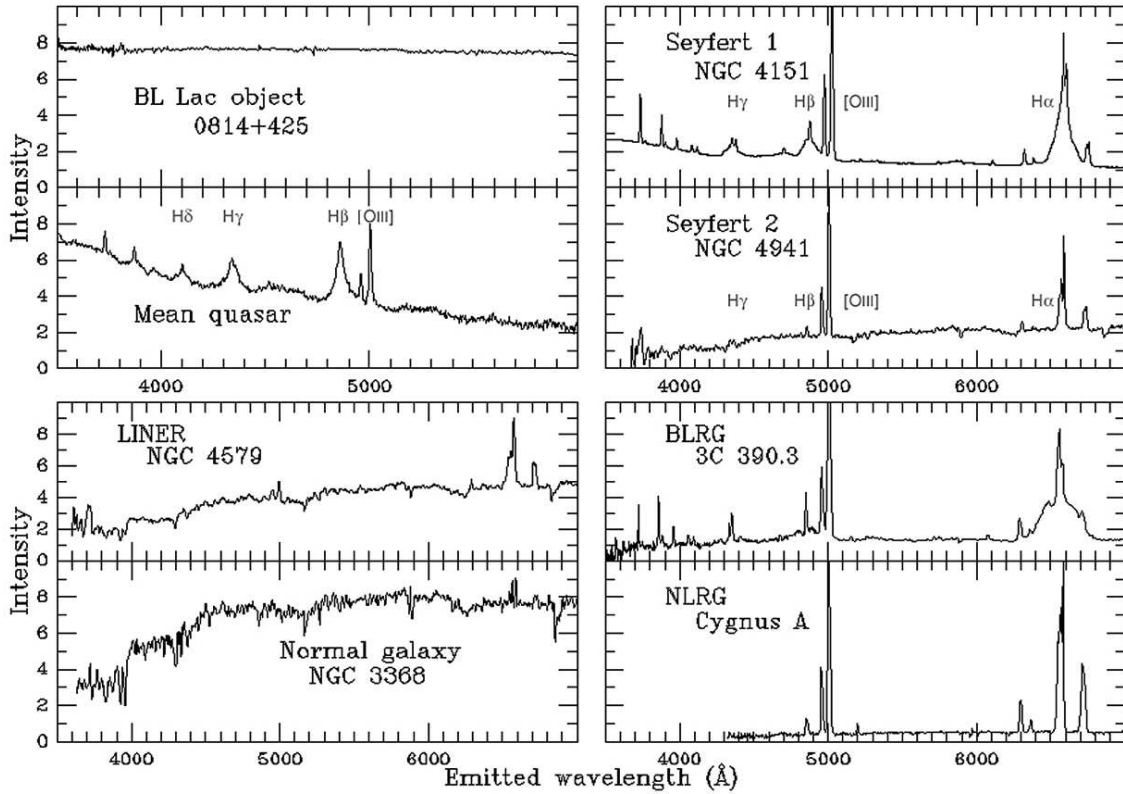


Figure 1.1.: Optical spectra of various types of galactic nuclei in the 3500-8000 Å range. The classical Seyfert galaxies show strong emission lines which clearly distinguish them from the normal galaxies. Seyfert 1 AGN have broad components in the wings of the permitted Balmer lines (analog to Quasars/QSOs), while Seyfert 2 AGN show only narrow lines. A similar dichotomy can be seen between broad-line (BLRG) and narrow-line radio galaxies (NLRG). LINERS are presumably the scaled down version of Seyfert galaxies. The individual spectra have been put together by William C. Keel (<http://www.astr.ua.edu/keel/agn/spectra.html>): NGC 4941 & 4579: Keel (1983); NGC 3368: Kennicutt (1992); Cyg A: Owen et al. (1990); 3C 390.3 & 0814+425: Lawrence et al. (1996); mean QSO: Francis et al. (1991); NGC 4151: compilation by Keel from several sources.

luminosities, however, do not favor significant contribution from stars to the overall emission.

Yet, it was still not clear if Seyfert 1 and Seyfert 2 objects share a common origin. A break-through to solve this question was achieved by Antonucci & Miller (1985). They found broad Balmer lines in the polarized spectrum of the prototypical Seyfert 2 galaxy NGC 1068. This indicated that Seyfert 2 galaxies host Seyfert 1 nuclei which are hidden presumably by a dust structure – an idea that triggered the *Unification Scheme* of Active Galactic Nuclei (AGN) (see Sect. 1.3) which considers various types of AGN, including Radio galaxies.

1.2. The source of energy in active galaxies

Since it appears unlikely that stars can produce the observed energies of Seyfert nuclei from X-rays to Radio wavelengths, a different source of energy has to be present in AGN. This becomes a compelling argument when considering quasi-stellar objects (QSOs), which show similar characteristics as Seyfert 1 galaxies but are even more luminous ($L_{\text{bol}} \sim 10^{45} - 10^{48} \text{ erg s}^{-1}$). The nuclei of QSOs are usually so bright that the host galaxies are outshined by several orders of magnitude. In addition, short time scale variability in the optical and X-rays suggests that the source of energy is a single compact object, rather than a cluster of stars.

As an alternative to nuclear fusion in stars, an even more efficient source of energy is the gravitational accretion of matter, in particular onto black holes. The presence of a supermassive black hole in AGN was suggested due to the observed broad emission lines which indicate gas velocities $>1000 \text{ km/s}$. Accretion of matter onto a black hole is believed to take place in a geometrically thin accretion disk. The maximum energy that can be transformed into radiation by accretion through the disk is $E_{\text{rad}} = \frac{1}{2} \frac{GMm}{R}$, where M is the mass of the central object and m the mass of the accreted matter. The other $1/2$ of the gravitational energy is conserved in Keplerian orbital motion within the disk (for the presented estimate, the factor $1/2$ is omitted though). In terms of luminosity, $L = dE_{\text{rad}}/dt$, we obtain

$$L = \frac{GM\dot{M}}{R} = \eta\dot{M}c^2 \quad (1.1)$$

where \dot{M} is the mass accretion rate, and $\eta = GM/(Rc^2) = R_S/(2R)$ is the efficiency of the process. In this picture, matter can approach the Schwarzschild radius, R_S , of the black hole up to a certain distance $R > R_S$ before the (orbital) motion becomes unstable and the matter vanishes beyond the event horizon. Depending on the actual metric of the black hole – rotating (Kerr) or static (Schwarzschild) –, the efficiency is $\eta = 0.06 - 0.42$ (see Unsöld & Baschek 2005). To support luminosities $\sim 10^{45} \text{ erg s}^{-1}$ as observed in some Seyfert AGN, of the order of $0.5 M_{\odot} \text{ yr}^{-1}$ have to be accreted.

1.3. Unification Scheme of AGN

The Unification Scheme tries to explain the known phenomena related to activity in galactic nuclei in a common picture (e.g., Antonucci 1993; Urry & Padovani 1995, see Fig. 1.2). Aside from the already discussed Seyfert galaxies and QSOs, it also incorporates galaxies with strong Radio emission (Radio-loud galaxies and Quasars), the starlike BL Lac objects which have blue, featureless spectra, and the low-ionization nuclear emission line (LINER) galaxies which are presumably the low-activity version of Seyfert galaxies. According to the Unification Scheme, the very high luminosities of AGN are produced by matter which is accreted onto a central supermassive black hole, as described in Sect. 1.2. The matter is arranged in an accretion disk which extends from the last stable orbit around the black hole outwards. The typical emission of an accretion disk is peaked in the UV (temperatures $T \sim 10^5 \text{ K}$) and declines in the optical towards the IR ($F_{\nu} \propto \lambda^{-1/3}$, Shakura & Sunyaev 1973). This picture is in

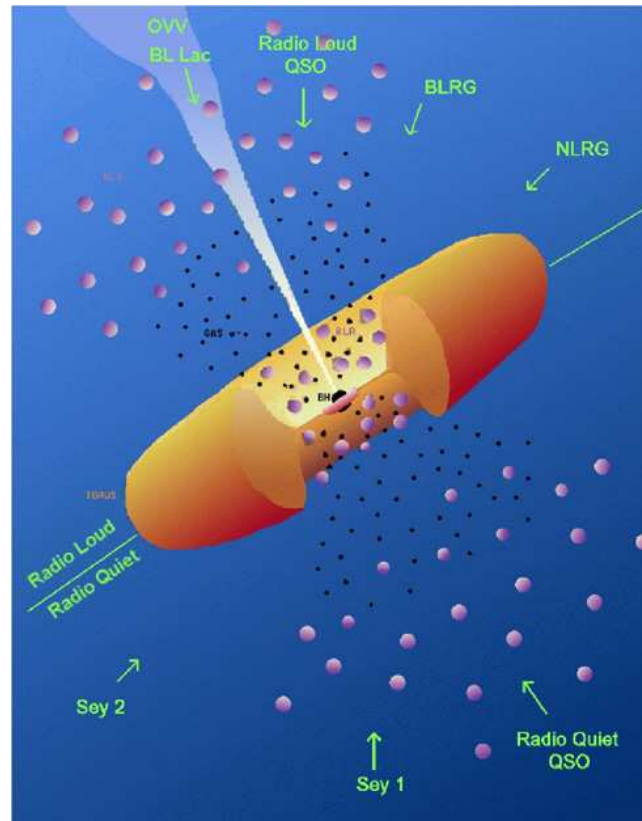


Figure 1.2.: Illustration of the Unification Scheme for AGN (Urry & Padovani 1995). For details, see text.

good agreement with observed composite QSO spectra which show UV/optical SEDs as theoretically expected (e.g. Elvis et al. 1994). The accretion disk emission is responsible for the “big blue bump” in the multi-wavelength spectrum of AGN.

Above and below the accretion disk, gas clouds are rotating around the supermassive black hole. The gas in these clouds is ionized by the radiation coming from the accretion disk. Assuming Keplerian motion, the hot clouds which are close to the accretion disk have high orbital velocities which cause the observed broad lines (“broad line region”; BLR). Cooler clouds at larger distances contribute the narrow lines to the spectrum (“narrow line region”; NLR).

The hot plasma in the accretion disk and the BLR are surrounded by an optically thick molecular structure containing a large mass of dust (“dust torus”). If the line of sight from the accretion disk to the observer is passing through the torus, the UV/optical accretion disk emission and the BLR are obscured. This suppresses the UV/optical continuum as well as the broad lines in the spectrum, so that the nucleus appears as a type 2 AGN. If the line of sight is not obscured by the torus, the accretion disk and BLR are directly seen and the AGN is classified as type 1. Intermediate Seyfert types correspond to different inclination angles of the torus towards the line-of-sight. The dust in the torus is heated up by absorbing parts of the accretion disk emission,

and thermally re-emits the received energy in the infrared (IR). This results in a second peak of the multi-wavelength AGN SED which is sometimes referred to as the “big red bump”, in reference to the big blue bump from the accretion disk emission.

In some AGN, the accretion process results in the ejection of energy in relatively narrow jets (Radio galaxies). These jets are usually seen at Radio wavelengths, but the resulting non-thermal continuum radiation can well extend into the IR and optical regime. In these Radio galaxies, the orientation of the torus is responsible for the difference between broad-line Radio galaxies and narrow-line Radio galaxies, which are the “Radio loud” counterparts of Seyfert 1 and Seyfert 2 AGN. In addition, beaming of the jet can change the appearance of the Radio galaxy. E.g., if the jet axis is oriented into the observer’s direction, the AGN spectrum is dominated by Doppler-boosted jet emission which we identify as featureless BL Lac objects (only continuum emission).

1.4. The dusty torus

As mentioned in the previous section, the cornerstone of the Unification Scheme is the presence of the dusty molecular torus around the accretion disk and BLR. It provides the obscuration of the AGN as seen in type 2 objects and probably provides the reservoir for feeding the accretion disk and the central black hole. The presence of the dusty, molecular torus has several direct and indirect impacts on the observed SED and structure of AGN in many wavelengths regimes. By combining observational evidence and theoretical considerations, some fundamental properties of the torus can be derived.

1.4.1. The dust content and its spectral signatures

According to the unification scheme, the accretion disk is hidden behind the torus in type 2 AGN. Thus, the UV/optical disk continuum is suppressed, resulting in a lack of the typical big blue bump. By comparing the intrinsic AGN UV/optical continuum in type 1 and type 2 objects, it is obvious that the dust torus has to be optically thick (optical depth of the dust $\tau_V > 1$), and that the UV/optical accretion disk continuum is the main source for heating the dust in the torus.

Beside the big red bump from the thermal emission, the dust in the torus (typically silicates and carbon grains as in the ISM) leaves a typical fingerprint in the MIR spectra of AGN. Silicates have strong rotation bands which absorb and emit at $9.7 \mu\text{m}$ and $\sim 18 \mu\text{m}$ ¹. Depending on the actual viewing angle of the torus, a silicate feature can be seen in emission or absorption. In Type 1 objects, the inner rim of the torus is directly visible to the observer. This inner rim is dominated by hot dust of temperatures $>1000 \text{ K}$. As a consequence, the silicate feature appears in emission. In type 2 AGN, the line of sight intersects with the torus. The hot region is seen through much colder dust ($T \sim 200 - 300 \text{ K}$) in the torus’ outskirts. This optically thick, cold dust absorbs most of the silicate emission feature produced by the inner hot dust. Thus, the silicate feature is seen in absorption.

¹Since the $9.7 \mu\text{m}$ silicate feature is narrower and has larger Q_{abs} than the $18 \mu\text{m}$ feature, it is more pronounced in model simulations, and easier accessible by ground based observations. Thus, the term “silicate feature” (or “ $10 \mu\text{m}$ feature”) usually refers to the $9.7 \mu\text{m}$ rotational bands of silicates.

1.4.2. Obscuration in the X-rays

In general, the dust in the torus is coupled to gas. Actually, assuming standard galactic dust-to-gas mass ratios of approximately 1:100, a significant part of the torus should consist of gas, mainly hydrogen. This results in typical hydrogen column densities, N_{H} , of $> 10^{22} \text{ cm}^{-2}$ when the AGN is seen through the torus. The effect of the high hydrogen column densities can be seen in X-ray spectra of type 2 objects. Due to the photo-electric effect, the low-energy X-ray spectrum ($E \lesssim 10 \text{ keV}$) is suppressed when looking through the torus. In cases of a nearly edge-on view of the torus, N_{H} can exceed 10^{25} cm^{-2} so that the gas becomes Compton thick and the soft X-ray spectrum is completely absorbed. As predicted by the Unification Scheme, observations show that the average column density in Type 1 AGN is much less than in Type 2 objects.

1.4.3. Geometrical thickness

The unification scheme of AGN assigns the difference between type 2 and type 1 AGN to the geometric situations that the line of sight intersects the torus or not. Thus, number statistics of AGN types allow for an estimation of the covering factor of the torus. Observations have shown that the ratio between type 1 and type 2 AGN is approximately between 1:1 and 1:3 (Osterbrock & Martel 1993; Maiolino & Rieke 1995; Lacy et al. 2004; Martínez-Sansigre 2005; Akylas et al. 2006). This means that the torus fills $\sim 2/3$ of the solid angle around an AGN. From the filling factor, f_{T} , it is possible to derive a representative torus opening angle, θ_{OA} ,

$$f_{\text{T}} = \frac{\Omega_{\text{torus}}}{4\pi} = \cos \frac{\theta_{\text{OA}}}{2}. \quad (1.2)$$

For a filling factor of $\sim 2/3$, the opening angle of the torus is in the range of $\theta_{\text{OA}} = 90^\circ$. Thus, the scale height, H/R , of the torus is approximately unity. This shows that the torus is indeed not only optically thick (obscuration) but also geometrically.

1.4.4. The size of the torus

Inner radius. The dust content of the torus sets a certain limit on its minimum inner radius. Standard dust compositions as observed in the Galactic interstellar matter (ISM) contain different species of Carbon (amorphous structure, crystalline graphite, etc.) and silicates (Olivine, Pyroxene, Silicon-carbide, etc.). Each of the species have different sublimation temperatures at which the grains are destroyed. The inner boundary of the torus is thus set by the maximum temperature, T_{sub} , which the dust can resist. Radiative equilibrium calculations for individual dust grains allow to estimate the sublimation radius, r_{sub} (e.g., Barvainis 1987). A dust grain is in radiative equilibrium if the incoming total luminosity equals the re-emitted luminosity:

$$\pi a^2 \int Q_{\text{abs};\text{UV}} F_{\nu}^{+}(r) d\nu = 4\pi a^2 \int Q_{\text{abs}} \pi B_{\nu}(T) d\nu, \quad (1.3)$$

where a is the grain size, Q_{abs} is the absorption efficiency of the dust, $F_{\nu}^{+}(r) = L_{\nu}/(4\pi r^2)$ is the incoming flux from the AGN, and $B_{\nu}(T)$ is the black body reemission

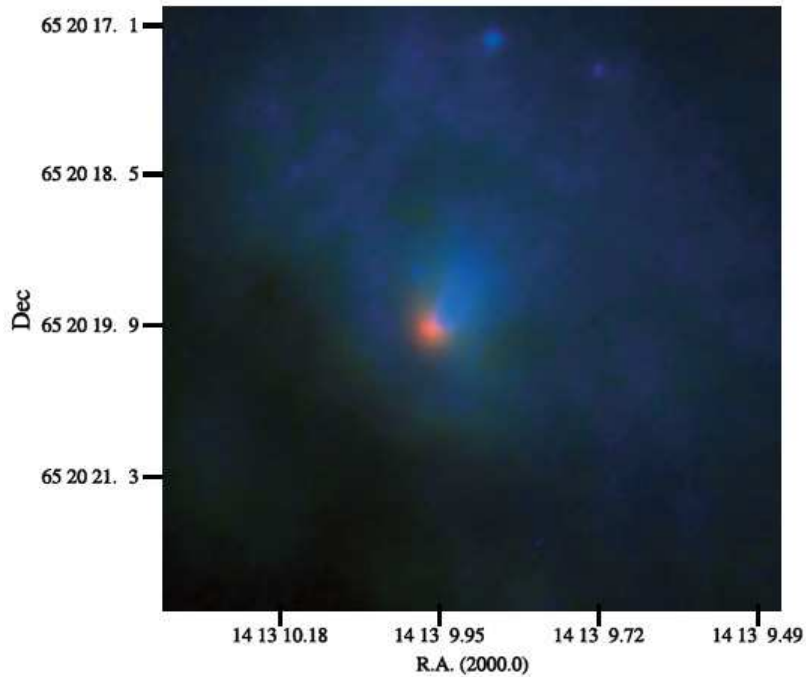


Figure 1.3.: Combination of a HST/WFPC image at $0.8 \mu\text{m}$ (blue), and VLT/NACO J (green) and K -band (red) images of the nuclear environment of the Circinus galaxy. The nucleus is marginally resolved in the K -band with a size of $1.9 \pm 0.6 \text{ pc}$. The declination refers to Southern latitudes. *Image: Prieto et al. (2004).*

at temperature T (Planck function). On the left side, we already assumed that most of the absorption occurs in the UV/optical where the absorption efficiency of dust, Q_{abs} , is approximately unity. Thus, the absorption cross section equals the geometrical cross section of the dust grain. For Q_{abs} , one usually assumes a power law $Q_{\text{abs}}/a = q_0 \nu^\gamma$ with $\gamma = 8/5$, which reproduces the laboratory results for graphite quite well. Dust opacity calculations (e.g., with DUSTY, Ivezić et al. 1999) of graphite grains with a size $a = 0.04 \mu\text{m}$ fix $q_0 = 2.29 \times 10^{-17} \text{ m}^{-1} \text{ Hz}^{-8/5}$ at $\nu = 3 \times 10^{14} \text{ Hz}$, so that we obtain

$$T = 1136 \text{ K} \times L_{45}^{5/28} r_{\text{pc}}^{-10/28} a_{0.04 \mu\text{m}}^{-5/28} \quad (1.4)$$

If we assume a typical sublimation temperature of graphite dust grains of $T_{\text{sub}} = 1500 \text{ K}$, a sublimation radius for the torus can be derived:

$$r_{\text{sub}} = 0.46 \text{ pc} \times L_{45}^{1/2} T_{\text{sub};1500 \text{ K}}^{14/5} a_{0.04 \mu\text{m}}^{1/2} \quad (1.5)$$

This shows that the dust torus is residing on parsec scales around the AGN. For the hottest dust emission in the NIR coming from the inner part of the torus, it can be expected that it has a size of few parsecs. Resolving these scales is challenging for current observational facilities.

Outer radius. Although there are several references to an “outer radius” of the torus (e.g., Pier & Krolik 1992; Granato & Danese 1994; Granato et al. 1997; Nenkova et al.

2002), it is difficult to set initial constraints. It is well possible that the dust smoothly connects to the host galaxy with a density gradient, instead of having a hard outer edge (Beckert & Duschl 2004). Thus, giving a wavelength/temperature-dependent outer radius inspired by Eqn. (1.4) is probably more appropriate. From the observed MIR emission in the big red bump, it can be concluded that the torus extends at least to scales of tens of parsecs.

1.4.5. Direct imaging of the torus

Despite strong indirect indications for the existence of the obscuring torus, the most convincing evidence would be a direct image or, at least, resolving the nuclear IR emission of AGN. As shown in Sect. 1.4, most of the NIR and MIR emission of the torus comes from a parsec scale region. This makes it a very difficult task for current (single-dish) telescope facilities without using interferometry (see Sect. 1.6). Since most AGN are more distant than 10 Mpc ($1'' \Leftrightarrow > 50$ pc), a scale of 1 pc corresponds to an angular size of < 20 mas. In fact, only one of the closest AGN – the Circinus galaxy – was marginally resolved in the continuum by direct imaging with a single 8 m telescope (Prieto et al. 2004). In the K -band, the size is reported as 1.9 ± 0.6 pc. Inferring a bolometric luminosity of 3×10^{43} erg s $^{-1}$ (e.g., Schartmann et al. 2005) with a sublimation radius $r_{\text{sub}} \sim 0.1$ pc (see Eqn. (1.5)), the size of the K -band emission would be $(9 \pm 3) \times r_{\text{sub}}$.

1.5. Torus models

Several torus models have been developed to compare the predictions of the unification scheme with observations. Most of these models are based on radiative transfer simulations of toroidal dust structures which are illuminated by the central AGN. They aim for reproducing the observed IR SED of AGN in agreement with the unification scheme. The models can be distinguished into two different types: smooth dust models (Sect. 1.5.1) and clumpy torus models (Sect. 1.5.2). Aside from these “classical” models, alternative approaches have also been presented (Sect. 1.5.3).

1.5.1. Smooth dust models

Several models have been presented where dust is smoothly distributed within the torus. These models are generally characterized by a cylindric symmetric geometry. They can consist of a radial and vertical dust density gradient and a homogeneous dust distribution in angular direction.

Pioneer work has been presented by Pier & Krolik (1992, 1993). They studied a compact torus with constant high dust density, which is embedded in a larger torus with lower dust density (see Fig. 1.4, left). It was shown that edge-on geometries (= type 2 AGN) tend to have more prominent absorption features than face-on cases (= type 1 AGN). They compared their model with an arcsec-scale SED of NGC 1068 and concluded that their torus model, together with some dust scattering in the outflow, reproduces the SED. It was predicted that the torus should have a total size of the order of 100 pc.

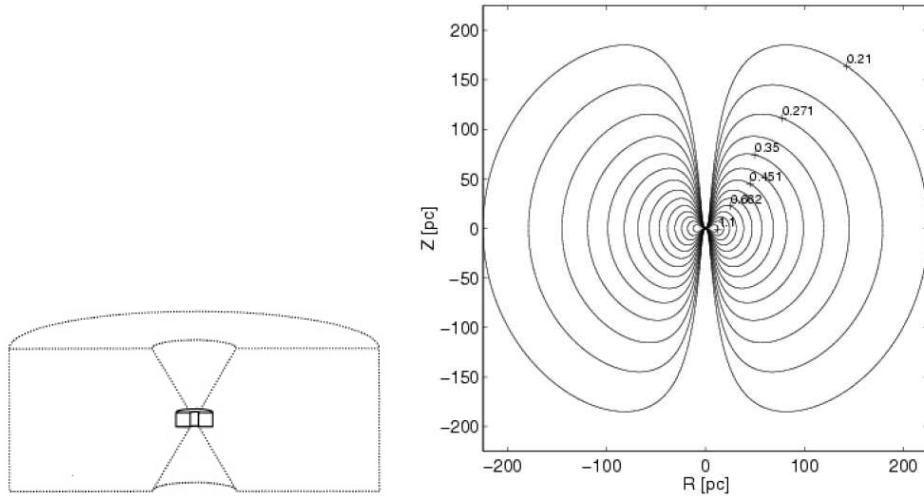


Figure 1.4.: Geometry of smooth dust distributions. *Left:* The pioneer work of Pier & Krolik (1992, 1993) used a compact torus with high dust density which is embedded in a larger torus with lower dust density. *Right:* Schartmann et al. (2005) studied a dust distribution which was motivated by a physical model for the formation of the torus.

Granato & Danese (1994) and Granato et al. (1997) developed a model which includes a radial density power law and an exponential density gradient along the vertical direction. Based on comparison with observations, they concluded that the main IR emission should come from a region of the order of tens of parsecs. They confirm that the torus models are in general agreement with the unification scheme.

More recently, Schartmann et al. (2005) studied a physically motivated dust distribution (see Fig. 1.4). In this model, the torus is residing within the gravitational potential of the supermassive black hole and a central stellar cluster. AGB stars within the cluster form the dust which is released by massive outflows. In the influence of the gravitational potential of black hole and stellar cluster, the dust gathers in a toroidal geometry with a narrow outflow funnel. Radiative transfer simulations of different chemical compositions of the dust and physical parameters of the environment agree with earlier smooth torus models. In particular, the high resolution IR SEDs of sub-arcsec scale of the Circinus galaxy and NGC 1068 have been reproduced.

Several authors who studied smooth dust torus models note that the modeled NIR colors are redder than what has been observed. Suggestions have been made that this may be the result of dust within the outflow cone or NLR which scatter radiation coming from the AGN and torus (e.g., Pier & Krolik 1993; Efstathiou & Rowan-Robinson 1995). A second issue concerns the silicate features: While smooth dust distributions generally predict prominent absorption features for edge-on geometries and emission features for face-on cases, MIR observations suggest that they are much less pronounced. In fact, it appears difficult to model simultaneously NIR and MIR photometry together with spectra of the $10\ \mu\text{m}$ silicate feature (e.g., Schartmann et al. 2005) with this kind of models.

1.5.2. Clumpy torus models

As an alternative to smooth dust distributions, it was proposed that the dust around AGN may be arranged in discrete clouds. Initially, Krolik & Begelman (1988) studied the physical conditions in the region of the torus. They note that if the observed velocity dispersions in the galactic nuclei is due to thermal motion, the corresponding gas temperature of $\sim 10^6$ K would be too high for dust to survive. If the gas would be cooler, the motion would be highly supersonic. These arguments led to the idea that the cool molecular gas is arranged in clouds which collide approximately once per orbit.

Since it is difficult and time-consuming to solve the radiative transfer equations for cloud distributions, straight-forward simulations of clumpy tori are challenging and special methods have to be developed. Before the start of this thesis, only one radiative transfer model of clumpy tori had been presented. Nenkova et al. (2002) used a statistical approach to characterize the average emission of an ensemble of clouds (Natta & Panagia 1984). They used a radial power law for the distribution of clumps, and a Gaussian distribution along the latitudinal angle of a spherical distribution. Beckert (2005) applied the same method, but used a physically motivated model for the properties of the dust clouds and torus (Beckert & Duschl 2004, see also Chapters 2 & 6). The general characteristics of the model SEDs are in agreement with the unification scheme. In particular, they found out that the modeled NIR colors do not need any major contribution from dust in the outflow cone to reproduce the observations. Furthermore, the silicate features are only moderately pronounced.

1.5.3. Alternative models

Alternatively to the torus models, other geometries have been suggested. As an example, Pringle (1996) suggests that warped accretion disk may explain the IR emission of AGN. Quillen (2001) proposed that this scenario is particularly interesting for objects which experience energetic outflows. In these cases, the wind can drive instabilities which cause the warping. For NGC 1068, a warped disk model was studied based on CO maps and polarization observations (Schinnerer et al. 2000). Although these models seem to successfully reproduce kinematic data of the AGN environment, it has not yet been shown that observed SEDs can be explained.

1.6. Interferometry of AGN dust tori

A powerful tool to study AGN dust tori is IR interferometry. With interferometry it is possible to spatially resolve the required small parsec scales at which the torus resides. This adds an important constraint for torus models: A successful torus model should be able to reproduce both the observed SED *and* the (wavelength-dependent) size of an object. Two kinds of interferometric techniques have been applied to AGN: Speckle interferometry and long-baseline interferometry. The Speckle method uses single telescope data to obtain visibilities and Fourier phases which are the prime interferometric observables. This allows to measure the sizes of structures which are smaller than the nominal diffraction limit of a single telescope, and it is possible to reconstruct diffraction-limited images (Speckle masking; Weigelt 1977; Lohmann et al. 1983).

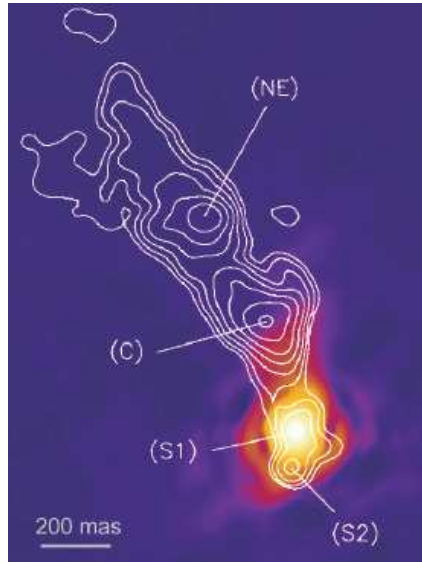


Figure 1.5: Reconstructed K -band image of the nucleus of NGC 1068 using the bispectrum Speckle interferometry method (Weigelt et al. 2004). Overlaid is a 5 GHz map which shows the Radio jet (Gallimore et al. 1996). The nucleus is resolved with a size of $18 \text{ mas} \perp \text{ jet}$ and $39 \text{ mas} \parallel \text{ jet}$. Image: Weigelt et al. (2004).

Wittkowski et al. (1998) report that the nucleus of the Seyfert 2 galaxy NGC 1068 has been resolved in the K -band, for the first time, using Speckle masking methods on data from the 6 m Special Astrophysical Observatory (SAO; Russia). With additional follow-up observations on the object, H - and K -band images were reconstructed with the bispectrum Speckle image reconstruction method (Weigelt et al. 2004). The images show an elongation of the nucleus of approximately $18 \times 39 \text{ mas}$ (error $\pm 4 \text{ mas}$) in both bands (see Fig. 1.5). Assuming a distance of 14.4 Mpc for NGC 1068, this corresponds to a physical size of $1.3 \times 2.8 \text{ pc}$.

In addition to Speckle interferometry, long-baseline interferometers in the infrared have become available. They aim for coherently combining the beams of two or more telescopes to detect interferometric fringes. By comparing the observed fringe contrast to a reference star, visibilities can be extracted. For image reconstruction, it is also necessary to obtain Fourier phase information. This is only possible with 3 or more telescopes. Current interferometric facilities, however, which have successfully detected AGN used only 2 telescopes (VLTI/VINCI, VLTI/MIDI, Keck interferometer). Thus, the visibilities at different baseline configurations are usually interpreted by fitting simple (e.g., one or multi-component Gaussian, uniform disk) or more complex emission models to derive sizes and elongations of the targets.

The first successful attempt to detect an AGN with IR long-baseline interferometry was reported by Swain et al. (2003). They observed the Seyfert 1 AGN NGC 4151 in the K -band using the two 10 m telescopes of the Keck interferometer. Due to the relatively high visibility of 0.92 ± 0.03 , interpretation of these observations is difficult (Swain et al. 2003; Kishimoto et al. 2007, and Chapter 5). With the VLT interferometer (VLTI), several AGN have been clearly resolved. The most intriguing example is the Seyfert 2 galaxy NGC 1068. Wittkowski et al. (2004) used a 46 m baseline together with the K -band VLTI instrument VINCI. They resolved the nuclear K -band emission and found a surprisingly high visibility of 0.4 ± 0.16 . Together with the Speckle results, this strongly suggest the presence of substructure within the nuclear emission region. In a

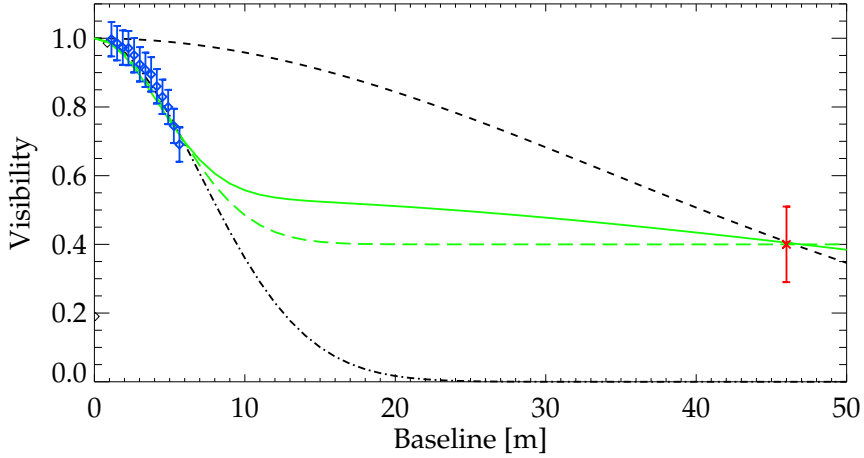


Figure 1.6.: *K*-band visibilities of NGC 1068. The short baseline data (0-6 m) was obtained by Speckle interferometry with the 6 m SAO telescope (Weigelt et al. 2004). In addition, VLTI/VINCI observed NGC 1068 at a baseline of 46 m (Wittkowski et al. 2004). The dashed-dotted line shows a single Gaussian fit (FWHM 26 mas) to the Speckle data, while the dashed line is a Gaussian model for the VINCI data only (FWHM 5 mas). The green curves combine 2 Gaussian models. Green dashed line: 36 mas FWHM (60% flux contribution) + 0.1 mas (40%); green solid line: 44 mas (46%) + 3 mas (54%).

fit with 2 Gaussians, they give an upper limit for the size of the unresolved emission source of 3 mas or 0.2 pc (see Fig. 1.6). Since the data is not consistent with a smooth dust torus, it was suggested that the flux is either coming from an ensemble of dust clouds, or that part of the accretion disk is visible through the torus. It has to be noted that both interpretations would favor a clumpy torus instead of a smooth dust distribution.

Supporting observations came from the mid-infrared VLTI instrument MIDI. Jaffe et al. (2004) report on spectrally dispersed total and correlated fluxes of NGC 1068 in the *N*-band. These were the first observations that resolved an AGN in the MIR. The interferometric data were interpreted by means of a two-component Gaussian model fit of thermal dust emission to the data. The model corresponds to a small hot object of $0.7 \times < 1$ pc with a temperature of > 800 K, which is embedded in a larger 2.1×3.4 pc component of ~ 320 K. The orientation of the well-extended emission is reported as approximately perpendicular to the jet. It has to be noted that the measured size is consistent with the estimation from Sect. 1.4. A striking result of these VLTI/MIDI observation was the presence of deeper silicate absorption features in the correlated fluxes than in the total flux. Some comparison to torus models (Jaffe et al. 2004, see also Sect. 1.5) let them suggest that this result is not consistent with expectations of a smooth dust torus. It was speculated that this is a signature for clumpiness inside the torus.

In addition to NGC 1068, further AGN have been studied using VLTI/MIDI. Tristram (2007) reports on recent, yet unpublished, results of a sample of 9 AGN with successful fringe detections. Essentially, the nucleus of the Circinus galaxy was the only one which showed unequivocal extension. A 2-dimensional Gaussian model fit suggests an N -band diameter of ~ 1.7 pc, with some dependence on direction and wavelength. This result is approximately consistent with the measured K -band size as reported by Prieto et al. (2004) (see Sect. 1.4.5). A detailed study of MIDI visibilities at several baselines and position angles suggests that the dust torus has a clumpy structure, as in the case of NGC 1068 (Tristram 2007).

1.7. Open questions and outline of the thesis

IR interferometry adds an important piece of information to test the unification scheme of AGN. It allows to resolve dust tori and, together with model fits, opens a window to their internal structure. Thus, it is of great importance to include this spatial and structural information to SED fits of AGN torus models. As mentioned in Sect. 1.5, several different torus models can reasonably reproduce the IR photometric SED of AGN. Nevertheless, at the beginning of this PhD thesis, the models had not been thoroughly tested against the interferometric data.

One of the key results from IR interferometry of AGN is the suggestion that the torus has a clumpy structure. On the other hand, most of the available torus models consider smoothly distributed dust. Thus, it is important to study tori which consist of dusty clouds. As of the beginning of this thesis, only one clumpy torus model had been presented (Nenkova et al. 2002). The problem is that the probabilistic approach of this model does not consider effects due to the random distribution of dust clouds in the torus. In particular, only limited predictions can be made for what has to be expected from interferometric measurements.

While IR interferometry has the potential of resolving few of the nearest dust tori, a general picture for the evolution with time and the AGN-torus feedback is still lacking. Several studies of large AGN samples have shown that there might be a evolutionary trend of torus covering factor and AGN luminosity. For low luminosities, the number of type 2 AGN seems to be a factor of ~ 4 higher than the number of type 1 objects. When going to QSO luminosities ($\lesssim 10^{46}$ erg s $^{-1}$), the type-1/type-2 ratio becomes approximately unity. Although it is still debated if some selection effects have to be taken into account for the number statistics of both types of AGN, this illustrates that physically motivated models for the formation and structure of dust tori are needed for the interpretation of various kinds of observational data.

In the framework of this PhD thesis, some of the open questions are addressed:

In Chapter 2, a new radiative transfer model for clumpy dust tori is presented. It accounts for 3-dimensional statistical effects due to the random arrangement of clouds inside the torus. With the resulting model images, it is possible to model simultaneously the photometric SED and spatial information from interferometry. For that, a new 2-step method for the radiative transfer simulations was developed.

In Chapter 3, the radiative transfer model is used to study the torus around NGC 1068. The combination of relatively small distance and high Seyfert luminosity makes it a perfect laboratory for torus studies. With high-angular resolution photometric data from 8 m class telescopes and visibilities for baselines up to 80 m, data are available for the parsec and sub-parsec scales at which the torus resides. With the clumpy torus model, it was possible, for the first time, to simultaneously reproduce the available photometric and interferometric data of NGC 1068.

In Chapter 4, the IR torus model of NGC 1068 is compared to multi-wavelength data, in particular in the Radio and millimeter regime. It is investigated to which degree emission processes which dominate at other wavelengths can contribute to the IR SED, in order to make progress towards understanding the broad picture of AGN activity in NGC 1068.

In Chapter 5, the case of Seyfert 1 AGN is examined. Since the central regions are seen face-on, the IR emission may consist of contributions from the torus, accretion disk, and Synchrotron sources. The question is: Can we learn something about the torus by observing type 1 AGN, or is the confusion with other emission sources too strong? By using HST/NICMOS observations of Radio-quiet Seyfert 1 AGN and predictions from the clumpy torus model, it was possible to determine the accretion disk contribution in the NIR for several objects.

In Chapter 6, some theoretical aspects concerning dust around AGN are highlighted. In particular, the influence of AGN luminosity on the dust in the torus is studied. As shown here, it is difficult to bind smoothly distributed dust to the central supermassive black holes if the accretion disks radiate close ($L/L_{\text{edd}} \gtrsim 0.1$) to the Eddington limit. On the other hand, the strong internal self-shielding allows dust clouds to withstand the strong AGN radiation. A physical model for clumpy dust tori is used to study consequences for the torus appearance at low and high AGN luminosities.

In Chapter 7, IR SEDs of obscured QSOs are modeled and interpreted with the radiative transfer simulations. Obscured QSOs (or type 2 QSOs, QSO2s) have been found only recently in X-ray and IR surveys. They are presumably the torus-obscured counterparts of “normal” type 1 QSOs. Here, the currently largest set of QSO2s with IR observations is used to study the nature of the obscuring matter in QSOs. Implications of this modeling effort can be compared to theoretical expectations for high-luminosity AGN.

In Chapter 8, results from this PhD thesis are summarized and an outlook for future work is given.

Publications related to the individual chapters are noted. Where necessary, the most significant contributions in the framework of this PhD thesis have been indicated at the beginning of the chapter.

2. A Three-Dimensional Radiative Transfer Model of Clumpy Dust Tori

This chapter is based on work published in the paper

Hönig, S. F., Beckert, T., Ohnaka, K., Weigelt, G. 2006, A&A, 452, 459

2.1. Overview and Context

Interferometric observations of NGC 1068 and the Circinus galaxy suggest that their tori have a clumpy structure. The original idea that the dust around AGN are arranged in clouds comes from Krolik & Begelman (1988). They argued that smooth dust distributions probably cannot survive in the vicinity of an AGN. According to them, the observed velocity dispersion is actually a result of the orbital motion of clouds within the gravitational potential.

First results of radiative transfer calculations of such a clumpy medium were reported by Nenkova et al. (2002) and Dullemond & van Bemmelen (2005). Nenkova et al. (2002) use a probabilistic approach to simulate SEDs of the dust tori. First, they used the DUSTY (Ivezić et al. 1999) radiative transfer code to simulate SEDs of dust slabs which are illuminated by an external source (AGN). The main parameters for these calculations are the distance of the slab from the source and the optical depth of the slab. The slab SEDs are used to evaluate the mean emission of clouds at a certain position (r, ϕ, θ) (spherical coordinates; origin is the AGN) in the torus. By using a density law for the distribution of clouds inside the torus, the mean emission coming from the torus could be simulated. For that, the escape probability of a photon at position (r, ϕ, θ) through the average number of obscuring clouds is calculated (Poisson statistics; see Natta & Panagia 1984). This procedure has the advantage that it is faster than, e.g. full Monte Carlo simulations. On the other hand, the probabilistic nature results in average SEDs and brightness profiles, which is unfavorable to determine effects from the actual random arrangement of distinct clouds.

A second attempt to model clumpy tori was reported by Dullemond & van Bemmelen (2005). They took a 2-dimensional geometry of 20-40 large clumps and simulated a cylindrical symmetric geometry with a Monte Carlo radiative transfer code. It was noted that the dust clouds are actually annuli around the symmetry axis. A comparison of the clumpy SEDs to smooth dust SEDs shows significant differences. Especially in the NIR, the clumpy torus models have bluer colors than the non-clumpy models.

In the following, we present our 3-dimensional Monte Carlo radiative transfer modeling of clumpy AGN tori. A method has been developed which allows us to perform high-resolution Monte Carlo simulations with relatively short computation times. We calculate the radiation fields of individual clouds at various distances from the AGN

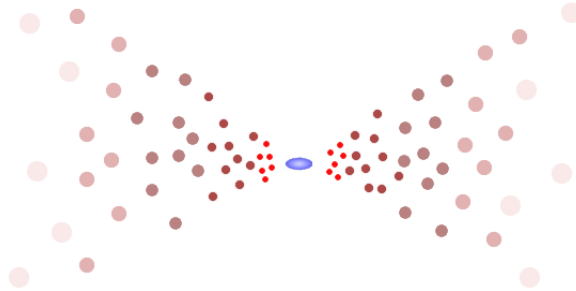


Figure 2.1.: Sketch of a clumpy torus. The hot and cold clouds are randomly distributed around a central accretion disk (blue). The size and optical thickness varies with radial distance.

and distribute these clouds within the torus region. After discussing the principle of our method, we present model spectra and images of clumpy tori and analyze the influence of various parameters.

2.2. Monte Carlo simulation of individual dust clouds

This section gives an overview of the Monte Carlo radiative transfer treatment with our code `mcsim_mpi` (Ohnaka et al. 2005) and describes its application to dust clouds. In the following, we present cloud SEDs and discuss some aspects of the Monte Carlo treatment.

2.2.1. AGN primary radiation

We consider a central super-massive black hole (smBH) which is fed by an accretion disk. The smBH and its accretion disk are surrounded by an optically and geometrically thick dust torus. Krolik & Begelman (1988) argue that the temperature has to be $\sim 10^6$ K if the velocity dispersion is of the order of 100 km s^{-1} . This temperature greatly exceeds the dust sublimation temperature. Thus, we arrange the dust in clouds. In Fig. 2.1, we illustrate the clumpy composition of the torus.

The primary source of radiation is the accretion disk. We approximate the SED of the accretion disk by a broken power law:

$$\lambda F_\lambda \propto \begin{cases} \lambda & \lambda < 0.03 \mu\text{m} \\ \text{constant} & 0.03 \mu\text{m} \leq \lambda \leq 0.3 \mu\text{m} \\ \lambda^{-3} & \lambda > 0.3 \mu\text{m} \end{cases} \quad (2.1)$$

It is illustrated in Fig. 2.2. The SED is a fit to QSO spectra (Manske et al. 1998) with a characteristic steep decline towards the MIR.

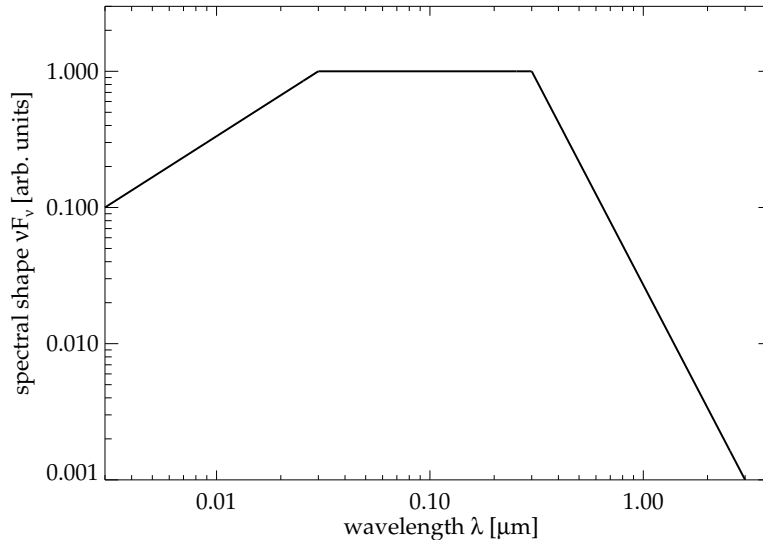


Figure 2.2.: AGN source spectrum as used in our Monte Carlo simulations.

2.2.2. Geometry and properties of individual dust clouds

Our radiative transfer code `mcsim_mpi` allows the modeling of dust distributions of arbitrary 3-dimensional geometry. Since there is no knowledge about the shape of dust clouds around AGN, we model spherically symmetric clouds. For our calculations, we assume a standard galactic dust composition of 53% astronomical silicates and 47% graphite (Draine & Lee 1984). The absorption and scattering efficiencies Q_{abs} and Q_{sca} for standard distributions of grain sizes (Mathis et al. 1977) have been calculated with the DUSTY code (Ivezić et al. 1999). In our Monte Carlo code, we use an average grain size of $0.1 \mu\text{m}$ representing the whole distribution (e.g. Efstathiou & Rowan-Robinson 1994; Wolf 2003).

For the characterization of the cloud radiation field, three main parameters are needed: the bolometric AGN luminosity L_{AGN} , the cloud optical depth τ_{cl} , and its distance r from the central source. τ_{cl} is taken at the reference visual wavelength of $0.55 \mu\text{m}$ and denotes the optical depth through the cloud center. At other wavelengths, the optical depth is derived from Q_{abs} . Within a cloud, the dust is distributed homogeneously. We generally model optically thick dust clouds ($\tau_{cl} \gg 1$). The high optical depths are needed to account for optically thick obscuration of the AGN in the UV/optical in a clumpy medium with small volume filling factors (Nenkova et al. 2002), and motivated by physical models for self-gravitating clouds (Beckert & Duschl 2004).

2.2.3. Radiative Transfer Code

Our radiative transfer code `mcsim_mpi` is based on the Monte Carlo approach by Bjorkman & Wood (2001). A detailed description of the code is given in Ohnaka et al. (2005). Here we briefly summarize the concept. As for any Monte Carlo approach in

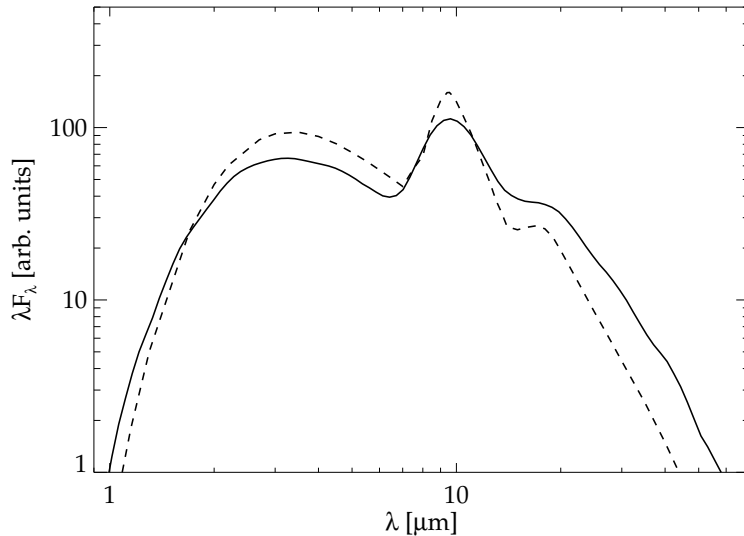


Figure 2.3.: Comparison of a hot-side cloud SED simulated with our Monte Carlo code `mcsim_mpi` (solid line) and a SED of a dust sphere with external isotropic illumination (obtained with the `DUSTY` code; dashed line). The Monte Carlo calculations were performed with 5×10^8 photon packages (see Sect. 2.2.4).

radiative transfer simulations, the luminosity of the central radiation source is divided into monochromatic photon packages. If a photon package hits a dust particle, it is either scattered or absorbed. In case the photon package is scattered, a random scattering angle is determined according to the differential cross section. If it is absorbed, the dust particle is heated up and the photon is re-emitted at a frequency determined by the dust temperature. The approach by Bjorkman & Wood has the advantage that it is non-iterative for fixed opacities and thus requires less computing time. As output, the code provides SEDs for scattered and absorbed photons, which are then added to a complete cloud SED. Furthermore, it is possible to obtain a number of cloud SEDs for different observer positions (=phase angles ϕ).

The code has been tested intensively and was recently applied to the modeling of VLTI MIDI visibilities of the evolved star IRAS 08002–3803 (Ohnaka et al. 2005). For testing our specific cloud geometry, we compared our cloud SEDs to results obtained with the `DUSTY` code. `DUSTY` allows the modeling of a dust sphere in an external isotropic radiation field. Although this is not exactly the same geometry as our external illumination by a central source, we use the resulting SEDs for comparison with the hot-side SEDs of our `mcsim_mpi` clouds. While the overall SED shapes are quite similar (see Fig. 2.3), the resulting differences are expected due to different illumination patterns.

2.2.4. Quality checks of Monte Carlo simulations

Depending on τ_{cl} , the temperature within a cloud decreases from the hot to the cold side. If the number of grid cells is too small, this temperature profile will not be reproduced

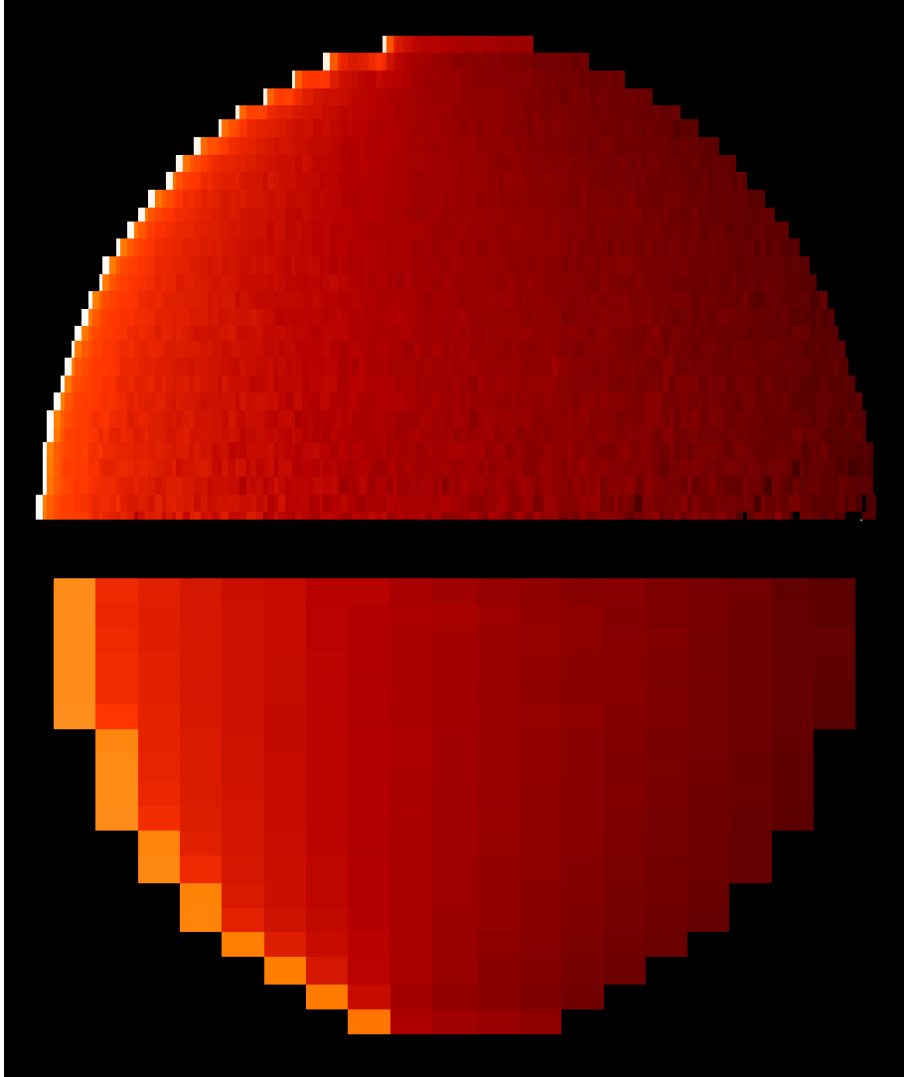


Figure 2.4.: Temperature profile of a simulated cloud ($\tau_{cl} = 150$) with a high-resolution grid (150×32 cells; top) and a low-resolution grid (20×20 cells; bottom). The number of photon packages are 5×10^8 for both simulations. The cloud was placed close to the dust sublimation radius, where the AGN is to the left. The hottest temperatures are ~ 1400 K (white), the coolest are ~ 200 K (dark red).

Table 2.1.: Temperature gradient variations for increasing numbers of radial cells within a cloud ($T_{\text{hot}} = 1500$ K).

number radial cells	$\Delta T(0.1 R_{cl})$ [K]	$\Delta T(R_{cl})$ [K]
10	560	660
20	580	800
40	600	980
70	610	1090
100	640	1160
150	640	1180

properly and parts of the cloud are either too cold or too hot. This specifically applies to clouds with high τ_{cl} since the temperature gradients can be steep. In Table 2.1 we show Monte Carlo temperature gradients for a cloud with $\tau_{cl} = 100$ at a distance of $r = r_{\text{sub}}$ ($T(r_{\text{sub}}) = 1500$ K) from the AGN. We list the temperature gradient from the hot side to one tenth of the cloud diameter inward, as well as the complete gradient from the front to the back side. As can be seen, the temperature gradients converge once a certain number of radial cells is used. Therefore, it is quite important to use enough radial cells to sample the temperature profile within a wide range of τ_{cl} values. In Fig. 2.4 we show the comparison of a cloud simulated with high and low resolution. For both simulations we used 5×10^8 photon packages (see next paragraph). In the low-resolution simulation, the temperatures on the hot side are too cold compared to the high-resolution simulation.

Furthermore, we have to ensure that enough photon packages interact in each grid cell. As discussed above, we use 100–150 grid cells in radial direction. Since the temperature gradients in the plane perpendicular to the radial direction do not need a very high resolution, we use only 32 cells. The 3-dimensional radiation field results from the rotational symmetry around the central radial axis. Thus, our clouds consist of $\sim 5 \times 10^3$ grid cells. Tests with the code show that the results are quite good for $10^6 - 10^7$ photon packages interacting in the cloud grid cells. If we take less than $\sim 10^6$ photon packages, the resulting SED becomes too noisy.

2.2.5. Cloud SEDs

We performed calculations for a number of different cloud parameters to study their SEDs and consequences for a clumpy torus. For the simulations we used 10^9 photon packages and $\sim 5 \times 10^3$ grid cells for each cloud.

In Fig. 2.5 we show our results for clouds with $\tau_{cl} = 70$. The clouds were placed at different distances from the AGN (1, 2, 4, and $8 r_{\text{sub}}$). For each cloud we show SEDs for three different phase angles ϕ . The phase angle is defined as the angle between the direction from the cloud to the observer and the direction from the cloud to the AGN, as seen from the cloud. $\phi = 0^\circ$ corresponds to a cloud that appears fully illuminated, while $\phi = 180^\circ$ represents the backside view of the cloud without direct AGN illumination. This concept is similar to the phases of the moon: depending on where the cloud is

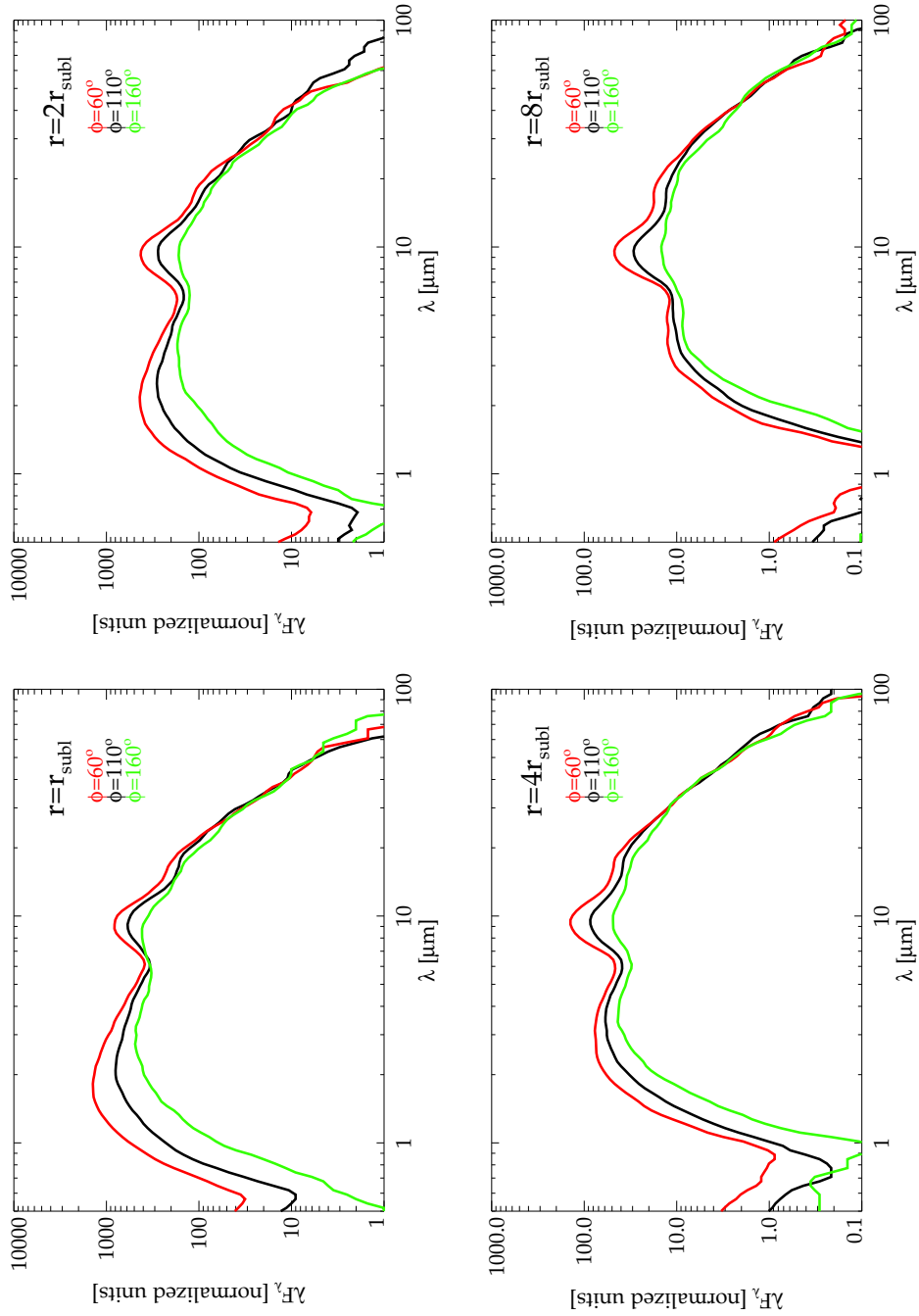


Figure 2.5: SEDs of spherical dust clouds with optical depths of $\tau_{cl} = 70$ simulated with our Monte Carlo code `mcsim_mpi`. In the upper row, the panels represent clouds at distances $r = r_{\text{sub}}$ and $r = 2 r_{\text{sub}}$; in the lower row they represent clouds at distances $r = 4 r_{\text{sub}}$ and $r = 8 r_{\text{sub}}$. For each cloud three SEDs are shown, as seen under phase angles of $\phi = 160^\circ$ (green), $\phi = 110^\circ$ (black), and $\phi = 60^\circ$ (red). In terms of illumination, these phase angles correspond to 3%, 33%, and 75%, respectively. The absolute flux values are normalized to the cloud surfaces.

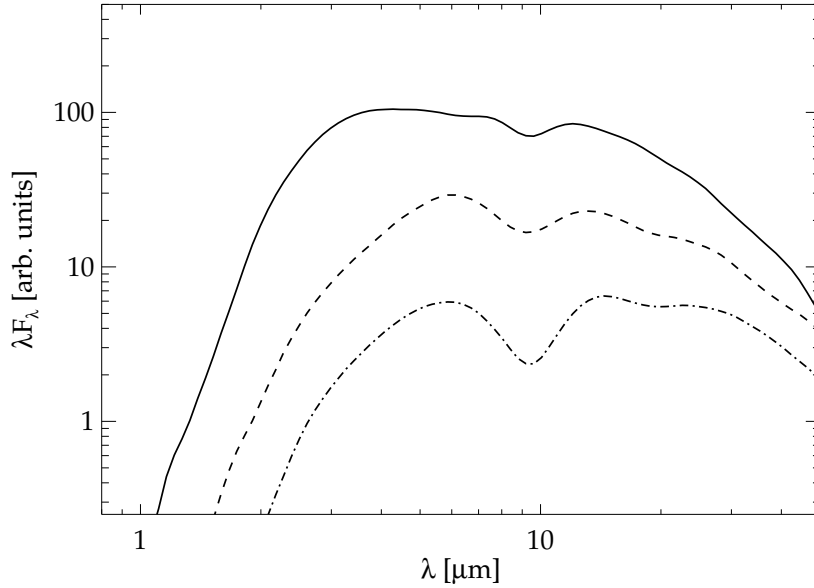


Figure 2.6.: Model SEDs of the unilluminated side of dust clouds at two different distances from the central source. The silicate feature is in absorption. The solid and the dashed SEDs represent clouds at $2 r_{\text{sub}}$ with $\tau_{cl} = 100$ and $\tau_{cl} = 400$, respectively. The dashed-dotted SED comes from a cloud at $4 r_{\text{sub}}$ and $\tau_{cl} = 250$.

located around the AGN, only a fraction of its surface seen by the observer is directly illuminated by the AGN.

The different panels in Fig. 2.5 show the dependence of the continuum peak on the distance to the AGN. The peak emission of the SED continuum shifts to longer wavelengths for larger distances. In addition, the absolute flux decreases. At larger distances from the AGN, the relative flux of the silicate emission at $\sim 10 \mu\text{m}$ increases with respect to the continuum. Furthermore, it is remarkable that the silicate emission feature is not as pronounced as in torus model SEDs of smooth dust distributions. Although the SEDs of Fig 2.5 are model SEDs of individual clouds, the implications for a torus spectrum are evident: because of the clumpy structure, the emission feature will not become very strong (see Sect. 2.4 and 3.2).

It is interesting to follow the SED development from the hot frontside to the cold backside view of each cloud. The cloud with the smallest distance to the AGN (cf. upper left panel in Fig. 2.5) shows a clear shift of the continuum peak from around $1.7 \mu\text{m}$ on the hot side to around $3 \mu\text{m}$ on the cold side. In addition, the silicate feature in emission starts to decrease with respect to the continuum. This is a result of the temperature gradient within the cloud. On the hot side, the temperature is high enough to produce an emission feature. The emission basically takes place in the upper dust layers of the hot parts. When the cloud is seen from the cold side, the hot side's emission has to pass through colder layers within the cloud and suffers from absorption. Furthermore, the colder layers produce less or no silicate emission. As a result, the overall feature gets

weaker. At larger distances (cf. lower right panel in Fig. 2.5), the emission from the hot side barely compensates for the absorption within the cloud, so the silicate emission disappears in the SED of the cloud's cold side. In the case of high τ_{cl} , large distances r , or no direct illumination, the emission may even turn into absorption. This effect is illustrated in Fig. 2.6, where SEDs from the cold side of clouds are shown for such cases.

2.3. Torus assembly

We will now present a simple parametrization of the torus. In the following, we describe our method for arranging the clouds within the torus. This method allows us to obtain model SEDs and model images of tori using the simulated cloud SEDs which have been calculated before. Afterwards, a physical model for the cloud properties is outlined. To distinguish between properties of clouds and the torus, we will label all cloud parameters with the subscript cl , while non-subscripted parameters always apply to the torus as a whole.

2.3.1. Torus parameters

To assemble the clumpy torus, it is necessary to get information about the cloud properties and the cloud distribution within the torus. A very simple approach to this problem is the modeling of these properties with free parameters and corresponding power laws. Geometric torus input parameters are the total number of clouds within the torus N_{tot} , their distribution $\eta_r(r)$ and $\eta_\varphi(\varphi)$ in radial and azimuthal direction, respectively, the scale height of the torus $H(r)$, which also determines the cloud distribution in z -direction $\eta_z(r, z)$, and its outer rim r_o (Nenkova et al. 2002).

For the radial distribution, we use a power law $\eta_r(r) \propto r^a$. The z - and r -dependencies of η_z are parameterized by a Gaussian-like ansatz; i.e., $\eta_z(r, z) = \exp(z^2/2H(r)^2)$. This accounts for a higher cloud density towards the equatorial plane and flaring of the torus. For simplicity, $\eta_\varphi(\varphi)$ is set to unity so that $\eta(r, z, \varphi) = \eta_r(r) \cdot \eta_z(r, z)$ and $\int \eta(r, z = 0, \varphi) dr = 1$. For convenience, we substitute the total number of clouds within the torus N_{tot} by the number of clouds N_0 along the line of view to the AGN in

Table 2.2.: Parameters of the *free parameter model* and the *accretion scenario* model.

model parameter	free parameter model	accretion scenario
clouds in equat. LOV N_0	free	free
optical depth $\tau_{cl}(r)$	$\tau_0 \times (r/r_{\text{sub}})^t$	$\propto M(r)^{1/2} r^{-3/2}$
cloud distribution $\eta_r(r)$	$\frac{1+a}{(r_{\text{out}}/r_{\text{sub}})^{1+a} - 1} \times (r/r_{\text{sub}})^a$	$\propto \left(\frac{M(r)}{\dot{M}}\right)^{1/2} r^{-3/2}$
cloud size $R_{cl}(r)$	$R_{cl0} \times (r/r_{\text{sub}})^b$	$\propto M(r)^{-1/2} r^{3/2}$
scale height $H(r)$	$hr_{\text{sub}} \times (r/r_{\text{sub}})^d$	$\propto \left(\frac{\dot{M}}{M(r)}\right)^{1/2} r^{3/2}$
outer radius r_{out}	free	—

the equatorial plane. The relation between N_{tot} and N_0 is given by

$$N_{\text{tot}} = N_0 \cdot \int \frac{\eta(r, z, \varphi)}{\pi R_{\text{cl}}^2} dV. \quad (2.2)$$

In this picture, $N_0\eta/(\pi R_{\text{cl}}^2)$ denotes the cloud number density per unit volume, and R_{cl} the cloud radius. After integrating with the definitions from Table 2.2, we obtain

$$N_{\text{tot}} = 8\pi N_0 h \frac{r_{\text{sub}}^2}{R_{\text{cl}0}^2} \frac{1+a}{2+a-2b+d} \frac{(r_{\text{out}}/r_{\text{sub}})^{2+a-2b+d} - 1}{(r_{\text{out}}/r_{\text{sub}})^{1+a} - 1} \quad (2.3)$$

It has to be noted that in this treatment, r refers to the radius in the equatorial plane (“cylindric r ”).

The basic torus parameters N_0 , $\eta(r, z, \varphi)$, $H(r)$, and r_{out} are supplemented by the properties of the clouds; in particular, their optical depth $\tau_{\text{cl}}(r)$ and radius $R_{\text{cl}}(r)$. Both parameters are written as r -dependent. Actually, whether τ_{cl} changes with distance or not is unclear. Theoretical arguments exist for a τ_{cl} gradient (see Sect. 2.3.3). Henceforth, a simple model with the power law parameters described above and listed in Table 2.2 is called a *free parameter model*.

2.3.2. Torus SED compilation and geometric peculiarities

Once a distribution function for the clouds is selected, random positions for N_{tot} clouds are determined according to $\eta(r, z, \varphi)$. Every position is labeled with the corresponding cloud properties τ_{cl} and R_{cl} , and a template spectrum from the database is associated with this position. As it happens, some of the clouds are not directly illuminated by the AGN since another cloud is along the line of sight to the AGN. Such clouds, however, can be indirectly illuminated by the radiation coming from surrounding clouds. Therefore, we must distinguish between these indirectly illuminated clouds (*Second Order Clouds; SOC*s) and clouds that are directly illuminated by the AGN (*First Order Clouds; FOC*s).

The treatment of FOCs and SOC is quite different. For FOCs we simply take the SEDs from the Monte Carlo output, as described in Sect. 2.2.5. Since there is no direct AGN illumination for a SOC, one has to approximate the illumination caused by all other clouds. Given the grid resolution that is needed for proper handling of the clumps, the necessary distances between the clouds, and the total number of clouds of several 10^4 , an approximation cannot be avoided since, otherwise, the number of photon packages would be $10^{13} - 10^{15}$ and more (see Sect. 2.2.4). This is difficult to achieve with current computation power.

In general, a SOC is located within the radiation field of the surrounding clouds. To approximate this diffuse radiation, we follow the scheme proposed by Nenkova et al. (2002). The main contribution to a SOC’s ambient radiation comes from the hot side of FOCs in the vicinity of the SOC. If we consider the diffuse radiation field to be isotropic, it is possible to approximate its SED at a given distance r from the AGN by averaging a FOC SED over all phase angles ϕ . To finally obtain the SED of a SOC, the average FOC spectrum can be taken as the input spectrum for an ambient radiation field in our Monte Carlo code. The strength of the ambient radiation field

is derived by taking into account the fraction of the sky covered by FOCs as seen by a SOC near the sublimation radius, where the FOC density is highest (= maximum SOC contribution estimate; see also Sect. 2.5). Because the ambient radiation field is assumed to be isotropic, the simulated SOC shows an identical SED for all phase angles ϕ . The results obtained from these calculations form the database for SOC templates. The method is discussed in Sect. 2.5 in more detail.

When all clouds have been associated with template SEDs from the FOC and SOC database, the torus SED can be compiled. For this purpose, a torus inclination angle i has to be chosen. A torus seen pole-on has $i = 0^\circ$, while the edge-on view corresponds to $i = 90^\circ$. As predicted by the Unification Scheme, type 1 AGN should have small i , whereas i should be larger (e.g., $> 45^\circ$) for type 2 objects. The inclination i also defines a line of view (LOV) from the observer to the torus clouds. With respect to this LOV, each cloud is seen under a specific phase angle ϕ , depending on its position in the torus. The corresponding SED as seen by the observer is taken from the templates, and the LOV between each cloud and observer is checked for obscuring clouds along the LOV. If there are other clouds, the template SED is attenuated according to the wavelength-dependent τ_{cl} -profile and the fraction of coverage. The resulting SED of this single cloud is added to the total torus SED. Once all clouds are considered, the torus SED is complete. Since this method of compiling the torus spectrum does not demand any special symmetry, it is also applicable to non-axisymmetric cloud distributions or other geometries. Actually, the statistical process of distributing clouds already introduces asymmetries.

2.3.3. Physical torus models and cloud properties

Power law models, as described in Sect. 2.3.1, are widely used in torus studies, although it would be desirable to have the parameters fixed by theoretical arguments. For example, Camenzind (1995) describes a smooth dust torus where the dust is produced in stars of a circumnuclear stellar cluster (cnSC). The toroidal geometry is a result of the effective gravitational potential coming from the smBH and the cnSC (Schartmann et al. 2005).

A physically motivated model for *clumpy* dust tori was proposed by Vollmer et al. (2004) and Beckert & Duschl (2004)¹. Its basic idea is that the dust clouds within the torus are self-gravitating. Their size is close to the shear limit given by the gravitational potential of the cnSC and the smBH. Actually, the torus is in a region where the influences of both the cnSC and the smBH are important. The cnSC is supposed to be spherically symmetric and isothermal; i.e., the relation of the enclosed mass of the cnSC is given by $M^{\text{SC}}(r) \propto r$. In this torus model, the material that forms the torus is accreted from large distances of more than $100 r_{\text{sub}}$. The *accretion scenario* assumes effective angular momentum transfer due to cloud collisions. This leads to large scale heights for high accretion rates above the Eddington limit of the central smBH. Since the enclosed mass in the torus is a combination of smBH and cnSC mass, the Eddington limit within the torus is higher than in the accretion disk. An advantage of this model is

¹For a more detailed description and further application of this physically motivated clumpy torus model, see Chapter 6.

that it reduces the number of free torus parameters. In addition to the AGN bolometric luminosity L_{AGN} and its black hole mass M_{BH} , one has to specify the mass accretion rate \dot{M} through the torus and the properties of the cnSC. The latter is defined by its core radius $R_{\text{core}}^{\text{SC}}$ and the core mass $M_{\text{core}}^{\text{SC}}$. The dependencies of the accretion scenario are listed in Table 2.2, in comparison to the free parameter model and constraints coming from observations. In the table, $M(r)$ denotes the sum of cnSC and smbBH masses. Furthermore, the accretion scenario doesn't need an outer radius for the torus. Since it predicts $R_{\text{cl}} \propto r^{3/2} \cdot M(r)^{-1/2}$, and $M_{\text{cl}} \propto r^{3/2} \cdot M(r)^{-1/2}$, the optical depth of a cloud is given by

$$\tau_{\text{cl}}(r) \propto \frac{M_{\text{cl}}}{R_{\text{cl}}^2} \propto M(r)^{1/2} \cdot r^{-3/2}.$$

For an isothermal cnSC, as observed in the center of our galaxy (e.g. Schödel et al. 2003), $M(r)$ is proportional to r so that $\tau_{\text{cl}}(r) \propto r^{-1}$. This implies that $\tau_{\text{cl}}(r)$ steadily decreases with increasing distance from the AGN. At larger distances, the clouds become larger and less dense so that they connect to the surrounding galactic ISM.

Some interesting predictions of the accretion scenario are the cloud sizes and masses. The total mass for clouds – gas and dust – close to the sublimation radius r_{sub} should be of the order of $1 \dots 5 M_{\odot}$, while the cloud radius is approximately 0.01 to 0.05 pc. Since R_{cl} and M_{cl} weakly depend on the enclosed mass, these values are similar for a wide range of smbBH and cnSC masses. Henceforth, for the modeling we use cloud properties which are consistent with the accretion scenario.

2.4. Results

In this section we present model SEDs and model images obtained from our torus simulations. The effect of the clumpy structure on the torus is analyzed by parameter studies. We briefly discuss the impact of clumpiness on the modeling of observations. For our parameter studies, we have chosen parameters listed in Table 2.3. Changes and variations to this set of parameters are noted in the text.

Table 2.3.: Parameters as used in our parameter studies.

Torus	Model Value	Clouds	Model Value
L_{AGN}	$2 \times L_{12}$	$R_{\text{cl}}(r)$	$0.02 \text{ pc} \times \left(\frac{r}{r_{\text{sub}}}\right)^{1.5}$
r_{sub}	0.8 pc	N_0	8
d	10 Mpc	τ_{cl}	$40 \times \left(\frac{r}{10 r_{\text{sub}}}\right)^{-0.8}$
$\eta_r(r) \propto r^a$	$a = -1.5$		
$H(r)$	$0.6 r_{\text{sub}} \times \left(\frac{r}{r_{\text{sub}}}\right)$	dust	see Sect. 2.2.2
r_{out}	$70 r_{\text{sub}}$		

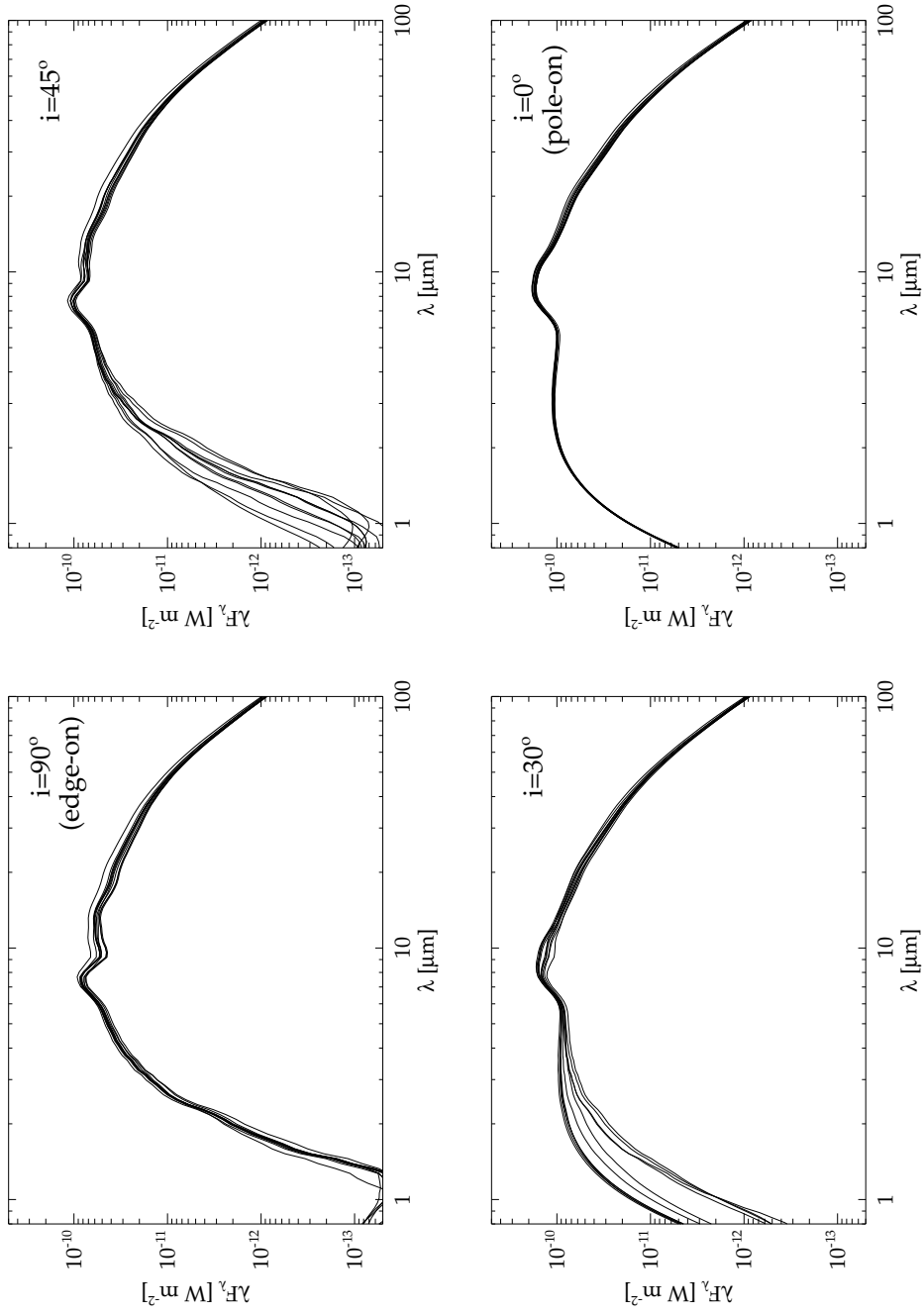


Figure 2.7: Torus SEDs of 10 different random cloud arrangements for the set of parameters listed in Table 2.3. The panels in the first row show SEDs for inclinations of $i = 90^\circ$ (edge-on; left) and $i = 45^\circ$ (right); the panels in the second row show $i = 30^\circ$ (left) and $i = 0^\circ$ (pole-on; right).

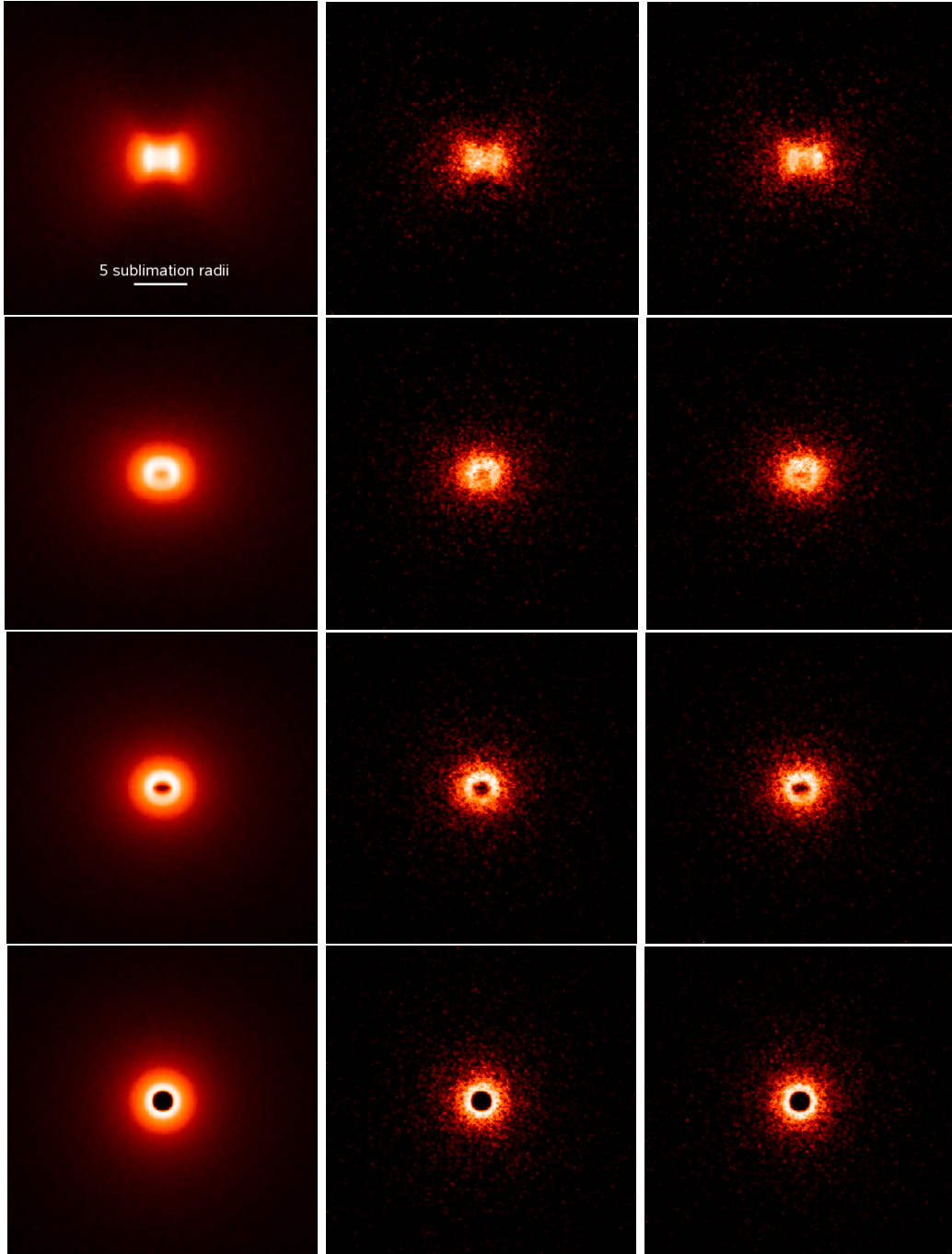


Figure 2.8.: *L*-band model images of the torus described by the parameters listed in Table 2.3 (same parameters as used for the SED calculations shown in Fig. 2.7). Left column: images obtained by averaging model images of ~ 200 different random cloud arrangements. Middle and right columns: model images for two particular random cloud arrangements. From top to bottom: $i = 90^\circ$, 45° , 30° , and 0° .

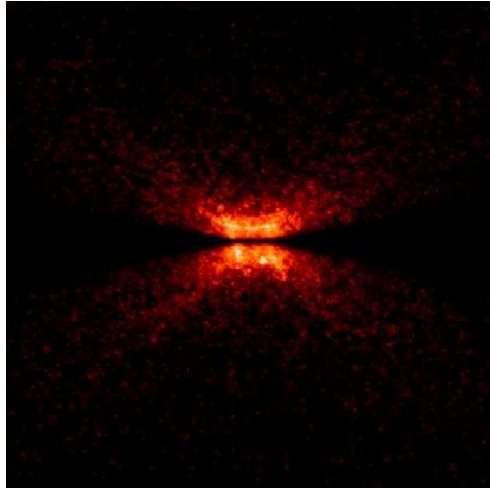


Figure 2.9.: *K*-band model image for *non-isotropic, sinusoidal radiation* from the accretion disk for one particular random cloud arrangement, edge-on view, and model parameters listed in Table 2.3

2.4.1. Statistical cloud distribution

The distribution of clouds follows a statistical process. Thus, it is expected that different statistical realizations of this distribution will change the torus SED. Since recent studies of clumpy tori use statistical averages (Nenkova et al. 2002), it is also worth investigating the scatter that has to be expected. In Fig. 2.7 we show the SED variation for one set of parameters (listed in Table 2.3). The only difference between the SEDs is the random arrangement of the clouds, following the same distribution function $\eta(r, z, \varphi)$. Analyzing the data shows that the slope of the NIR flux is comparable for all random cloud arrangements. The absolute fluxes and the silicate feature differ by a factor of 2 – 3 for the edge-on view. The large SED scatter at $i = 30^\circ$ is a result of the transition from edge-on to pole-on view. The FIR fluxes get close to each other at longer wavelengths since the optical depth of the torus becomes smaller than unity, so that obscuration no longer plays an important role.

We investigated the origin of the dependence of the SED on the random cloud arrangement. As we found out, these variations are caused by the FOCs. They are the main contributors at the shorter wavelengths of the SED. A few bright FOCs at high latitudes can change the SED considerably since high-latitude clouds are usually less obscured.

In Fig. 2.8 we present model images for inclinations $i = 90^\circ, 45^\circ, 30^\circ$, and 0° . For each inclination angle, we show two different kinds of images: the left column presents an average image derived from ~ 200 different random cloud arrangements; the mid and right columns show images calculated for two individual random cloud arrangements (wavelength range $4.65 - 4.95 \mu\text{m}$; for model parameters as listed in Table 2.3). In all images, the assumed faint emission from the central AGN is not shown (see Sect. 2.2.1 and Fig. 2.2). The images obtained for particular random cloud arrangements show a similar overall appearance with distinct differences in the substructure. The *grainy*

structure in the images is a result of the *clumpiness* of the torus and not related to noise of the radiative transfer simulations. It illustrates the appearance of a clumpy torus for very high-angular resolution observations.

In the average image for $i = 90^\circ$, a polar cavity with an X-shaped structure is visible. At $i = 45^\circ$ and 0° , a bright inner structure is the dominant source of emission, which is caused by the inner torus rim. At $i = 30^\circ$, parts of the inner rim of the torus can be seen as a crescent structure. The central dark region for $i = 30^\circ$ and 0° is the inner dust-free region. The apparently well-defined brightness steps in the averaged images will disappear as more different clouds are added to the database of SOCs.

The model images presented in Fig. 2.8 were calculated for an isotropic radiation of the accretion disk. Fig. 2.9 shows a model image obtained for a *non-isotropic*, sinusoidal radiation field of the accretion disk. If the torus is illuminated by this non-isotropic radiation, a dark apparent dust lane appears in the disk plane when the torus is viewed edge-on.

2.4.2. Radial Distribution function

To illustrate the effect of the radial cloud distribution function $\eta_r(r)$ on the SED, we keep all parameters in Table 2.3 constant, except for exponent a of the radial power law. Fig. 2.10 shows the resulting SEDs for $a = -1.0$ (accretion scenario), $a = -1.5$, and $a = -2.0$ for both the edge-on and pole-on views of the torus. The relative depth of the silicate feature in absorption becomes larger with growing a . Additionally, the NIR flux decreases for both the pole-on and edge-on views, and the variations become stronger. This can be explained by the higher density of clouds with large τ_{cl} close to r_{sub} . As a result, the obscuration of the FOCs in that area becomes higher and their total flux decreases. Small differences in the arrangement can then lead to higher variations.

It is interesting to look at the evolution of the silicate emission feature in the pole-on view. The feature is quite flat and less pronounced than for smooth dust distributions, and it decreases for larger a . This effect comes from the higher cloud density of FOCs close to r_{sub} when emission and absorption in that region become equally important. Tori with $a \gtrsim 2$ can flatten out the emission feature for small i or even show moderate absorption.

2.4.3. The effect of flaring

The z -dependence of the cloud distribution function is assumed to follow a Gaussian distribution, $\eta_z \propto \exp(-z^2/2H(r)^2)$ (see Sect. 2.3.1). Thus, the toroidal structure flares depending on the r -dependence of H . In Fig. 2.11 we show the model SEDs for $H \propto r^{0.5}$, $r^{1.0}$, $r^{1.2}$, and $r^{1.5}$. For the edge-on geometry, the flaring has some effect on the relative depth of the silicate feature. For small flaring the feature is deeper, and the overall flux is also lower by a factor of $\sim 3 - 4$. This can be explained by the absence of clouds at higher latitudes which are usually less obscured and thus contribute significantly to the NIR and MIR fluxes.

For the pole-on view, the importance of flaring is more evident. The NIR and MIR fluxes decrease significantly when the flaring becomes stronger since there are more

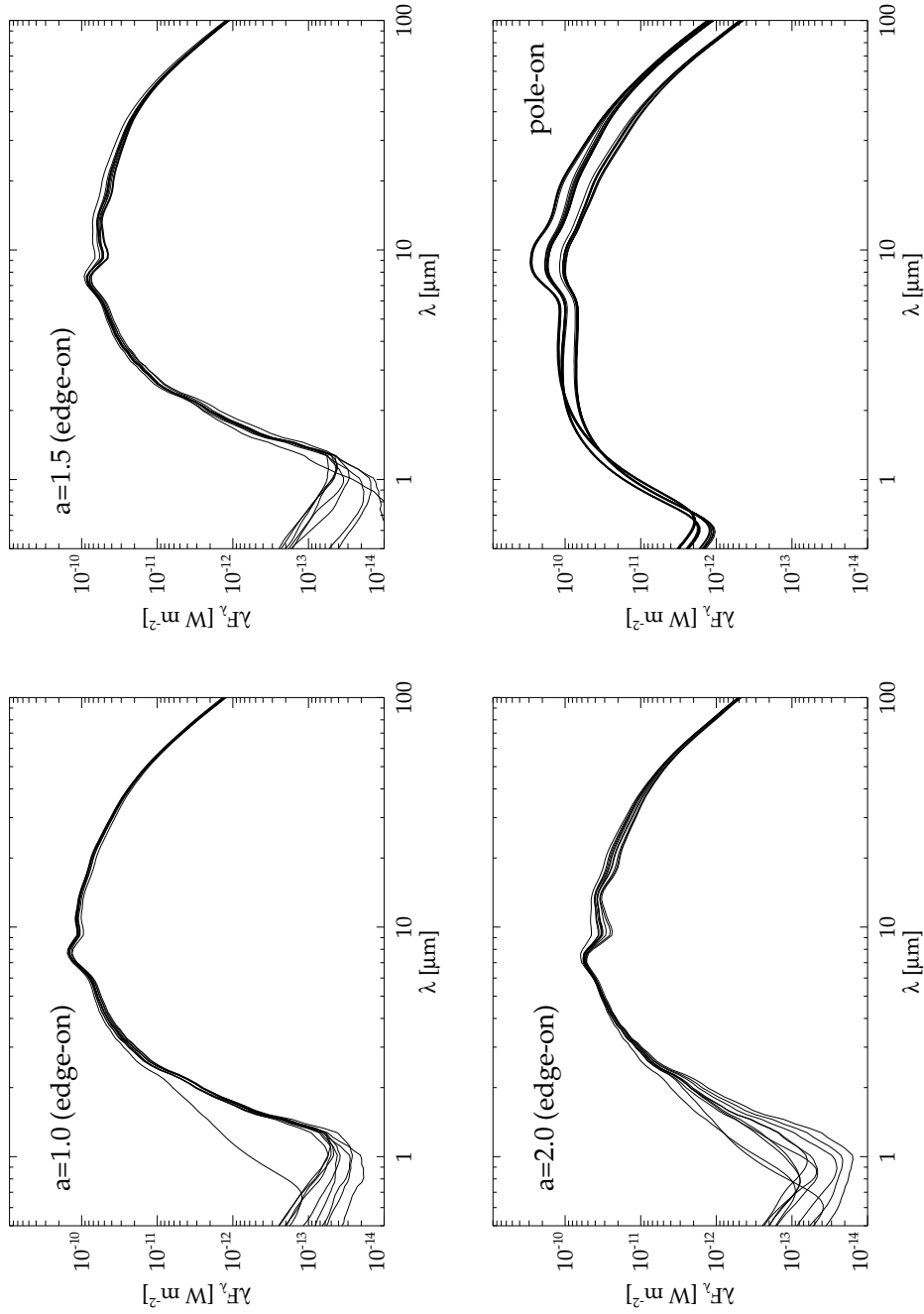


Figure 2.10: The dependence of the SED on η_r (model parameters in Table 2.3). The upper panels show edge-on SEDs for 10 different random cloud arrangements for $a = -1.0$ (left) and $a = -1.5$ (right). In the lower left panel we present the edge-on view for $a = -2.0$, while the lower right panel combines pole-on views of the three models with $a = -1.0$ (top), $a = -1.5$ (middle), and $a = -2.0$ (bottom).

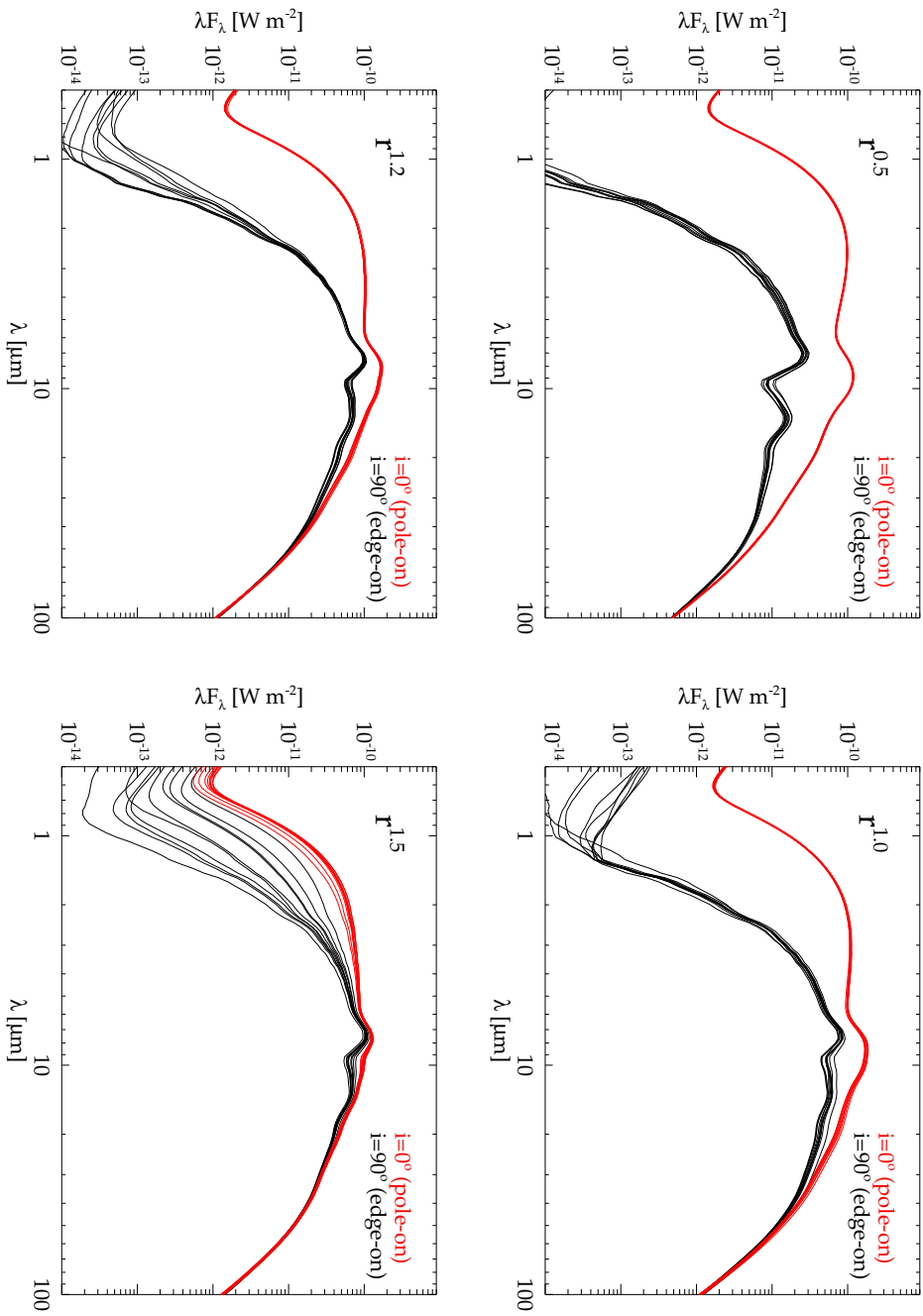


Figure 2.11: SEDs for different flaring (see text; model parameters in Table 2.3). From upper left to lower right: $H \propto r^{0.5}$, $r^{1.0}$, $r^{1.2}$, and $r^{1.5}$, respectively. Each panel consists of SEDs for 10 different random cloud arrangements seen edge-on (black) and pole-on (red).

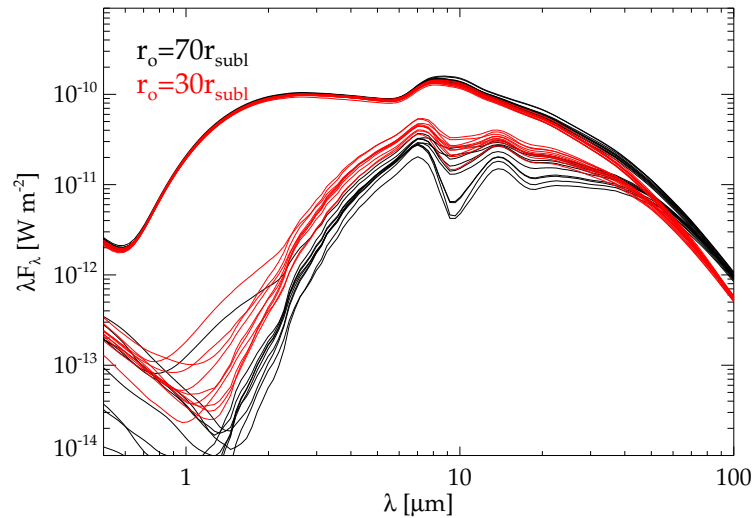


Figure 2.12.: SEDs for outer radii of $r_o = 70 r_{\text{sub}}$ (black) and $r_o = 30 r_{\text{sub}}$ (red) seen edge-on (bottom SEDs) and pole-on (top SEDs; model parameters in Table 2.3).

and more clouds at high latitudes that obscure the denser parts of the torus structure. As a result, the emission feature vanishes for $H \propto r^{1.5}$ and can even turn into weak absorption for stronger flaring.

2.4.4. The outer radius of the torus

Since the main torus emission in the NIR and MIR comes from the innermost part, it is expected that the SED is not very sensitive to the outer boundary of the torus. This especially applies if τ_{cl} decreases with r , as proposed by the accretion scenario (Sect. 2.3.3). In this case, the innermost part of the torus dominates since absorption by more distant clouds is weak. Thus, the strongest effect of the outer torus radius r_o is expected in cases where distant clouds significantly contribute to the obscuration of the inner torus. To test this, we investigated the influence of r_o for the extreme case of $\tau_{cl} = 70$ (constant) throughout the torus. We simulated SEDs for $r_o = 30 r_{\text{sub}}$ and $r_o = 70 r_{\text{sub}}$, respectively.

Our results are shown in Fig. 2.12. The overall shape of the SED is similar for both modeled r_o , while there are some differences in the absolute fluxes. Since the central region is less obscured for $r_o = 30 r_{\text{sub}}$, the NIR and MIR fluxes are higher. On the other hand, the FIR flux of the $r_o = 70 r_{\text{sub}}$ model is above the flux for the smaller radius since the outer cold part is missing in the latter model.

2.5. Discussion and assessments of the method

In early simulations we noted that for some random cloud arrangements with a rather edge-on LOV, few individual clouds at intermediate distances can completely fill up

the silicate absorption features and even turn them into emission. These clouds are generally FOCs with lower optical depths which are seen more or less face-on without experiencing any absorption by other clouds. Since they are at intermediate distances from the AGN, they contribute only marginally to the hot NIR emission. Furthermore, their overall MIR *continuum* emission is not significant. Their peak emission is usually located in the silicate emission feature, which causes the fill-up of the torus absorption feature. In real tori, such clouds are probably experiencing some kind of absorption by either other very distant clouds, some diffuse dust between the clouds, or dust in the host galaxy, especially since this effect happens only in edge-on line-of-sights. In our simulations, we suppressed the contribution from such clouds in order to be not dominated by an individual (or very few) clouds in the silicate feature. In the next section, it is shown that this suppression has no significant consequence on the energy budget.

As described in 2.3.2, our treatment of the SOC heating assumes that we have the same number of FOCs around a SOC at all distances from the AGN. In reality, the relative number of FOCs, however, decreases with growing distance. As a result, we overestimate the ambient radiation field that heats the SOCs. We discuss the influence of our treatment of the ambient radiation field on the torus simulations in the following sections.

2.5.1. Energy conservation

One important test of our simulations is the study of energy conservation. It is possible to derive a theoretically expected luminosity of the torus. In our model, the average number of clouds along a LOS, $\langle N \rangle$, is given by a Gaussian distribution:

$$\langle N \rangle = N_0 \cdot \exp\left(-\frac{1}{2} \frac{z^2}{H^2}\right) = N_0 \cdot \exp\left(-\frac{1}{2} \frac{r^2 \tan^2 \alpha}{H^2}\right) \quad (2.4)$$

where α is the latitudinal angle in spherical coordinates ($z = r \cdot \tan \alpha$) and $H = H(r)$ is the scale height. For simplicity, we assume $H(r) = h \cdot \frac{r}{r_{\text{sub}}}$ in the following discussion. $\langle N \rangle$ is the expected value for Poisson statistics. The probability of finding n clouds along a LOV is given by

$$P(n) = \frac{\langle N \rangle^n}{n!} \exp(-\langle N \rangle). \quad (2.5)$$

The probability that we see the AGN unobscured along a LOV is obtained for $n=0$:

$$P(0) = \exp(-\langle N \rangle) = \exp\left(-N_0 \cdot \exp\left(-\frac{1}{2} \frac{r_{\text{sub}}^2 \tan^2 \alpha}{h^2}\right)\right) \quad (2.6)$$

It is our aim to find the probability that a photon emitted by the AGN in a random direction is hitting a cloud in the torus. For this goal, we simply determine from Eqn. (2.6) the probability w_0 that a photon emitted by the AGN in a random direction is escaping the AGN undisturbed by averaging all possible LOV:

$$w_0 = 2 \int_0^{\frac{\pi}{2}} P(0) \cos \alpha \, d\alpha. \quad (2.7)$$

The probability w_T that a photon hits a cloud in the torus is given by

$$w_T = 1 - w_0. \quad (2.8)$$

Thus, the theoretically expected luminosity L_{theor} of the torus is

$$L_{\text{theor}} = w_T \cdot L_{\text{AGN}} = (1 - w_0) \cdot L_{\text{AGN}} \quad (2.9)$$

This is the theoretical reference luminosity for our simulations. For energy conservation in the Monte Carlo simulations of the clouds, L_{theor} should be equal to the (unobscured) re-emitted luminosity L_{FOC} of all first order clouds in the torus. We made a number of simulations which showed that in our simulations $L_{\text{theor}} = L_{\text{FOC}}$ to an accuracy of $\sim 2\%$.

Finally, this luminosity L_{FOC} should be re-emitted by our simulated tori when obscuration and SOCs (ambient radiation field) are considered in the simulations, so that $L_{\text{theor}} = L_{\text{FOC}} = L_{\text{sim}}$. Our studies showed that in our simulations

$$L_{\text{theor}} = 0.98 - 1.02 \times L_{\text{FOC}} = 0.95 - 1.05 \times L_{\text{sim}}. \quad (2.10)$$

Differences of the order of $\sim 5\%$ are observed, depending on the actual cloud distribution function. From this analysis we conclude that energy is conserved in our simulations with satisfying accuracy.

2.5.2. SED shape

We have carefully investigated the effect of our SOC approximation on the total torus SED shape. Our SOCs are generally too hot since the heating by surrounding clouds is overestimated (see Sect. 2.3.2). The ambient radiation field around a SOC in the torus is determined by considering the fraction of the sky around a SOC that is covered by FOCs. This fraction is derived within the inner 2.5 sublimation radii, where the heating of SOCs by surrounding FOCs is strongest within the torus. This treatment results in an overestimation of the ambient radiation field around SOCs at larger distances from the AGN.

We investigated at what wavelengths our SOCs contribute to the torus SED. By removing the SOC emission from our simulations, we found out that the SOC contribution is relevant only longward of $\sim 20 \mu\text{m}$. In the NIR and MIR up to $20 \mu\text{m}$, there is no difference in the torus SED simulations with and without SOCs. The discrepancy between a torus simulation with SOCs and without SOCs becomes a factor of ~ 2.5 in flux only longward of $100 \mu\text{m}$. This factor is constant for wavelengths larger than $100 \mu\text{m}$.

In a next step, we investigated the influence of the FOCs on the torus SED. In our current treatment, we only consider direct heating by the AGN. FOCs, however, are also heated by surrounding clouds. This missing heating of FOCs mainly concerns the cold backside of the FOCs. To get an estimation of this additional heating, we added a SOC SED from our SOC treatment (i.e., an overestimated SOC SED) to the FOC backside SED. We found out that in our simulations the contribution from additionally heated FOC backsides is small at all wavelengths. In the NIR and MIR, no difference

in the SED is seen at all. In the FIR, a small increase in flux can be observed. The increase at $100\ \mu\text{m}$ is $\sim 10\%$. Thus, the contribution of heated FOC backsides can be considered as insignificant in our simulations.

The SEDs obtained with our SOC treatment represent an upper limit for the real SED. In addition, our simulations without SOCs set a lower limit for the SED. The real SED is somewhere in-between. From the discussion above, we can set upper limits for the maximum overestimation and conclude:

- In the short wavelength range up to $20\ \mu\text{m}$, our SOC treatment has almost no influence on the SED (i.e., error $< 2\%$).
- Between $20\ \mu\text{m}$ and $30\ \mu\text{m}$, our SOC treatment can cause maximum deviations from the real SED of the same order as the variations by different random cloud arrangements (i.e., $\sim 5\text{-}10\%$).
- Longward of $100\ \mu\text{m}$, the flux overestimation due to our SOC treatment is less than a factor of ~ 2.5 .
- The influence of our SOC treatment on the luminosity is less than 5% (see Sect. 2.5.1).
- The heating of FOC backsides by surrounding clouds is insignificant for NIR and MIR, and is only $\sim 10\%$ at $100\ \mu\text{m}$.

The studies also highlight that the hot front sides of the FOCs are the dominant contributors to the ambient radiation field that heats the SOCs. Therefore, we conclude that our simulations are satisfying shortward of $20\ \mu\text{m}$. An improvement of the ambient radiation field for longer wavelengths by simulating the local FOC-to-SOC-relation and the r -dependence of the FOC density for any cloud distribution will be the topic of a future investigations.

2.5.3. Improved method

To improve the method of calculating the SOC radiation field, we propose a new method for approximating the ambient radiation field. For that, we determine the average covering factor of FOCs around a certain cloud at equatorial distance r in the torus. The average number of clouds which are obscuring the central AGN at equatorial distance r can be calculated by integrating the number density, $N_c(r) = N_0\eta_r$, along an equatorial line of sight:

$$N(r) = \int_{r_{\text{sub}}}^r N_c(r) dr' = N_0 \int_{r_{\text{sub}}}^r \eta_r dr' = N_0 \frac{(r/r_{\text{sub}})^{1+a} - 1}{(r_{\text{out}}/r_{\text{sub}})^{1+a} - 1} \quad (2.11)$$

The probability, $P_{\text{FOC}}(r)$, of finding a FOC at r in the equatorial plane can be estimated by the probability that the AGN is directly visible at that distance. According to Natta & Panagia (1984) and Nenkova et al. (2002), we can use Poisson statistics to determine this probability, so that

$$P_{\text{FOC}}(r) = P_0(N(r)) = \exp(-N(r)). \quad (2.12)$$

Thus, the fraction of the sky, $f_{\text{FOC}}(r)$, which is covered by FOCs at distance r is better approximated by $f_{\text{FOC}} = P_{\text{FOC}}(r)$ instead of using our original method where $f_{\text{FOC}}(r) = 1$ at all r . As a consequence, the luminosity of the ambient radiation field has to be adjusted by $f_{\text{FOC}}(r)$.

This method can even be improved by accounting for the decrease in cloud density with increasing distance from the equatorial plane. In the latter case, Eqn. (2.11) has to be rewritten with $\eta_r \cdot \eta_z$. For a non-flaring case (i.e., $H(r) \propto r$), this can be integrated analytically, while for other flaring parameters, b , a numerical integration method has to be applied. The implementation of this new method is currently under way and will be part of future work (see Chapter 8).

2.6. Summary and conclusions

We presented a new two-step method for 3-dimensional radiative transfer modeling of *clumpy* dust tori of AGN. First, SEDs of individual dust clouds are simulated with our Monte Carlo code. Then, the modeled clouds are randomly arranged within the torus region. The cloud properties are derived from a physically motivated accretion scenario proposed by Vollmer et al. (2004) and Beckert & Duschl (2004). We investigated the influence of clumpy dust distributions on model SEDs. Furthermore, our methods were tested with respect to energy conservation and application to different wavelength regimes.

For type 2 objects, we find a moderately pronounced silicate absorption feature which is in agreement with observations. Type 1 model SEDs show moderate emission. The modeled silicate emission-to-continuum flux ratio of ~ 2 (see Figs. 2.7, 2.10, and 2.11) agrees with recently observed emission features in QSOs and a LINER where the ratio is 1.5–2.5 (Siebenmorgen et al. 2005; Hao et al. 2005; Sturm et al. 2005). In addition, the total NIR and MIR model fluxes are approximately in agreement with observations. It is not necessary to assume additional dust in the polar region to reproduce the observed fluxes.

The actual random cloud arrangement has a significant effect on the SED and images. For the same set of large-scale torus parameters, we find remarkably different SEDs for different random cloud arrangements. The depth of the silicate feature decreases if the number of unobscured clouds is increased in comparison to other random arrangements. Strong statistical variations of the optical depth of the torus due to the clumpiness have already been predicted by Nenkova et al. (2002). They argue that due to Poisson statistics, clumpiness is able to account for the high variation in X-ray column densities in Seyfert 2 galaxies. We show that clumpiness not only affects absorption of radiation from the central source but also has strong effects on the IR emission of the torus itself.

For type 1 AGN, we find that the silicate emission may vanish if the toroidal geometry has strong flaring or a high cloud density towards the center. This may apply to Seyfert 1 nuclei with no emission feature observed. In such cases, the absence of a silicate feature does not necessarily mean that there is no dust torus present.

Finally, we give an outlook for the next steps that can be done to improve the models. In particular, we propose a new method to obtain a better estimate of the local ambient radiation field around a dust cloud in the torus. This will be part of future work.

3. NGC 1068 – the Seyfert 2 Prototype for Torus Studies

This chapter is based on work published in the papers

Hönig, S. F., Beckert, T., Ohnaka, K., Weigelt, G. 2006, A&A, 452, 459

Hönig, S. F., Beckert, T., Ohnaka, K., Weigelt, G. 2007, ASPC, 373, 487 (Conference proceedings “The Central Engine of Active Galactic Nuclei”, ed. L. C. Ho and J.-M. Wang, San Francisco: ASP)

3.1. Overview and Context

As already mentioned in Chapter 1, NGC 1068 is a prime target for torus studies. With a distance of ~ 14.4 Mpc, $1''$ on the sky corresponds to a physical scale of approximately 70 pc. With single 8 m telescopes, it is possible to resolve scales of ~ 5 pc in the NIR and 30 pc in the MIR. This is about the size that models predict for the extension of the dust torus. With interferometric methods, even the sub-parsec regime is accessible in the infrared.

The nucleus of NGC 1068 is heavily obscured at wavelengths shortward of $\sim 1 \mu\text{m}$. Since the host galaxy is seen face-on, the obscuring medium is presumably located in the central region rather than the host galaxy. The nuclear environment is Compton-thick to X-rays (hydrogen column densities $\gtrsim 10^{24} \text{ cm}^{-2}$), and the UV/optical accretion disk continuum is suppressed and not visible. Spectro-polarimetry observations of NGC 1068 were the key component for the introduction of the unification schemes of AGN. In the “normal” optical spectrum, only narrow emission lines are present. Antonucci & Miller (1985) report on spectro-polarimetry of the [OIII] and Balmer line region (see Fig. 3.1). While the [OIII] lines are highly polarized but narrow, the Balmer lines show a polarized component with broad line wings. They note that the polarized spectrum resembles a Seyfert 1 spectrum, which led to the suggestion that NGC 1068 harbors a hidden type 1 AGN.

On the 100 pc scale around the nucleus, a strong emission line region is visible at UV and optical wavelengths. HST images show a cone-like outflow region towards the Northern direction (see Fig. 3.2, top right). It was possible to identify several NLR clouds within the outflow and determine their 3-dimensional positions (Kishimoto 1999). They are approximately aligned with the Radio jet as reported by Gallimore et al. (1996). The NLR cloud spectra are dominated by line emission. Their continuum fluxes show a high degree of polarization, presumably caused by scattering of light from the central hidden AGN region. The polarization vectors are perpendicular to the jet axis and show some centro-symmetry. Their normal vectors are pointing towards a

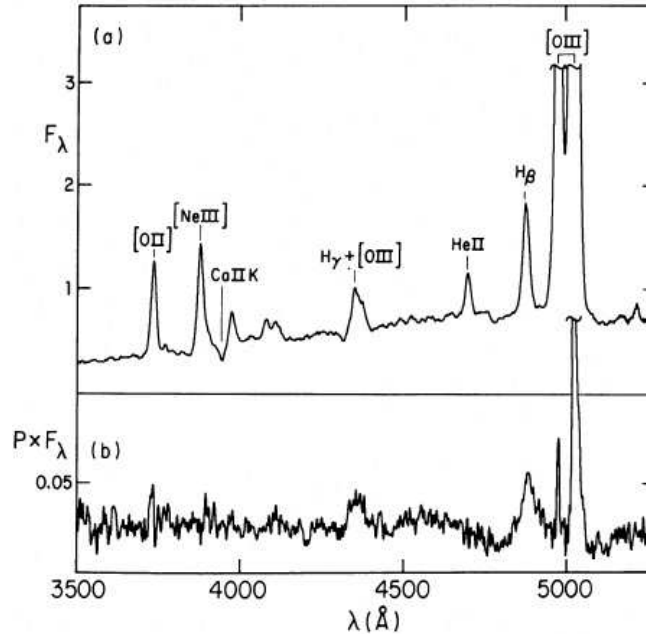


Figure 3.1.: Total and polarized fluxes (arbitrary unit) of the nucleus of NGC 1068 as reported by Antonucci & Miller (1985). The upper panel shows several narrow emission lines which are present in the total spectrum. In the polarized flux (lower panel), the $H\beta$ line shows broad wings as observed in type 1 AGN.

single position which is coaligned within $0''.08$ with the assumed nucleus S1 in Radio wavelengths (e.g., Capetti et al. 1995; Kishimoto 1999).

The outflow/jet structure can also be seen in the MIR. Recently, Galliano et al. (2005) report on VLT/VISIR imaging of the inner few arcseconds of NGC 1068 in the $[NeII]$ filter ($\lambda = 12.8 \mu\text{m}$). An $\sim 1''$ jet-like extension towards North is seen following the inner radio jet. Further out, the MIR extension changes the direction and emission knots are visible. Apparently, the MIR emission brackets the outer Radio jet, and the MIR knots are aligned with clouds seen in the visual $[OIII]$ image. The inner part of the jet-like MIR structure up to the change of direction can also be seen in Speckle reconstructed K -band images (Weigelt et al. 2004). The actual emission mechanism of this region is still a matter of debate. The discussion includes shock-heating of gas and dust related to the jet injection into the surrounding medium, dust scattering, and optically thin and thick thermal dust emission. A compilation of the described observations is shown in Fig 3.2.

The actual nucleus of NGC 1068 has been resolved in the Radio and IR regimes. While the Radio emission will be discussed in detail in Chapter 4, we will now focus on the IR emission which forms the red bump in the SED. It is, presumably, dominated by dust scattering and thermal re-emission in the torus. The fact that the NIR and MIR emission region is resolved with interferometric methods adds important spatial information to the modeling attempts, and may allow to distinguish between different type of models.

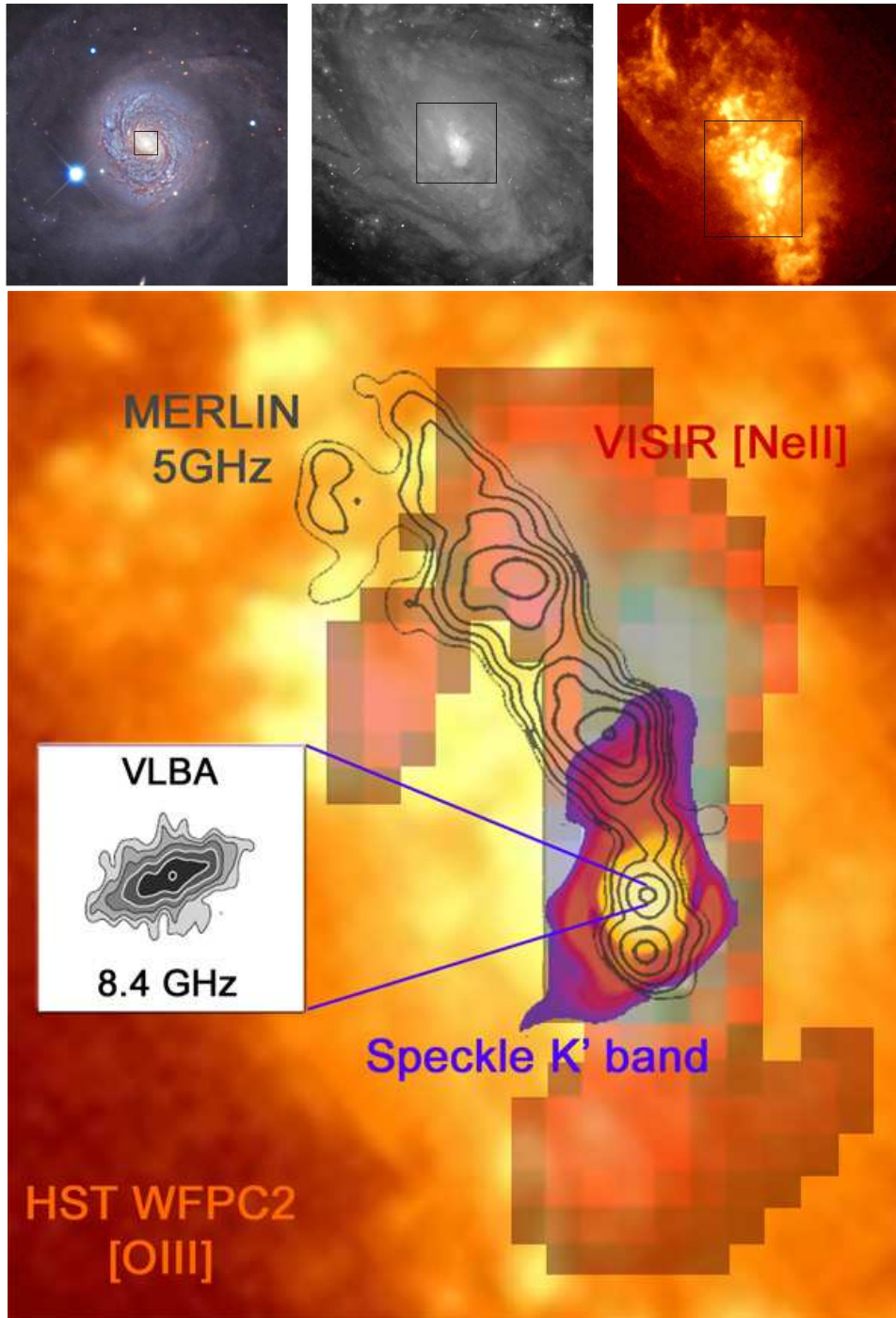


Figure 3.2.: Zooming into the parsec scale region of the nucleus of NGC 1068. **Top left:** Optical image of the whole galaxy *Image: Ken Crawford*; **Top middle:** Archival HST/ACS image ($0.55 \mu\text{m}$) 700 pc around the nucleus; **Top right:** HST/WFPC2 [OIII] line image of the NLR (150 pc radius) (Dressel et al. 1997); **Bottom:** Overlay on the [OIII] image of the Radio jet at 5 GHz (Gallimore et al. 2004), the extended MIR emission (VISIR NeII filter; Galliano et al. 2005), and the *K*-band speckle image (Weigelt et al. 2004). Vertical scale: $1''7/120 \text{ pc}$. The VLBA 8.4 GHz inset shows the central 40 mas Radio emission (Gallimore et al. 2004).

3.2. Simultaneous modeling of the IR SED and IR visibilities of NGC 1068

With the clumpy torus model described in Chapter 2, we have a tool to quantitatively interpret the nuclear observations of NGC 1068. The goal of our radiative transfer modeling studies is to find a model which can simultaneously reproduce both the observed high spatial resolution IR SED and the interferometric visibilities obtained during the last few years. In particular, the following observations are considered:

- NIR and MIR photometry in the wavelength range of 1.3 to 18 μm listed in Table 3.1. All data points are taken with 8 m class telescopes.
- 8 to 13 μm low-resolution spectrum of the total nuclear flux which was obtained using VLTI/MIDI (Jaffe et al. 2004). This spectral range covers the silicate absorption feature which is typical for type 2 AGN.
- NIR speckle interferometric visibilities in the *H*- and *K*-band (Weigelt et al. 2004) at baselines between 0 – 6 m.
- wavelength-dependent visibilities in the 8 – 13 μm range which were obtained with the VLTI/MIDI instrument (Jaffe et al. 2004). The most striking feature of these interferometric measurements was the presence of deeper silicate features in the correlated fluxes (= total flux(λ) \times visibility(λ)) of longer baselines than at shorter baselines and in the total fluxes.
- *K*-band visibility at 46 m baseline as observed with the VLTI/VINCI instrument (Wittkowski et al. 2004).

We tried to find a set of model parameters that can simultaneously reproduce all of these observations. For this goal, we scanned the parameter space, as described in Sect. 2.4, and obtained the clumpy torus model parameters listed in Table 3.2. Figs. 3.3 and 3.6 present the model SED and *K*-, *M*-, and *N*-band model images.

Fig. 3.3 shows a comparison of NGC 1068's average model SED, the variation range of the model SEDs obtained for 10 different random cloud arrangements, and the observed high angular resolution SED. There is a satisfactory agreement between the observed and modeled SED. In particular, the modeled silicate absorption feature at $\sim 10 \mu\text{m}$ is following the observed total MIDI *N*-band spectrum. This is an improvement to smooth dust models which usually predict stronger silicate features for similar NIR colors (e.g., Granato et al. 1997; Schartmann et al. 2005).

Fig. 3.5 shows the visibilities of our NGC 1068 model (Table 3.2) in the range of 8 – 13 μm . The model visibilities are roughly in agreement with the observed MIDI visibilities for 42 m and 78 m baselines (Jaffe et al. 2004). It is important to note that the model follows the trend of deeper silicate features at longer baseline, as seen in the MIDI visibilities. Apparently, this behavior cannot be explained by smooth dust distribution torus models (Jaffe et al. 2004; Schartmann et al. 2005). As a consequence, the MIDI observations may provide structural information that allows for distinguishing between the various types of models. This will help in removing model ambiguities

Table 3.1.: Photometric data for the nuclear region of NGC 1068 from high-resolution observations.

Wavelength μm	Flux Jy	Phot. Aperture arcsec	Reference
1.3	0.00048	0.2	Rouan et al. (1998)
1.6	0.07 ± 0.02	0.1	Weigelt et al. (2004)
1.8	0.0054	0.2	Rouan et al. (1998)
2.1	0.35 ± 0.09	0.1	Weigelt et al. (2004)
2.2	0.056	0.27	Prieto (2004) ¹
3.5	1.34	0.4	Marco & Alloin (2000)
3.8	1.42	0.4	Marco & Brooks (2003)
4.5	2.5	0.27	Prieto (2004) ¹
4.7	2.72 ± 0.14	0.4	Marco & Brooks (2003)
4.8	3.23 ± 0.32	0.4	Marco & Alloin (2000)
7.7	8.8 ± 1.0	0.4	Tomono et al. (2001)
8.7	10.0 ± 1.2	0.4	Tomono et al. (2001)
9.7	7.04 ± 0.80	0.4	Tomono et al. (2001)
10.4	7.94 ± 0.87	0.4	Tomono et al. (2001)
11.7	17.8 ± 2.2	0.4	Tomono et al. (2001)
12.3	17.2 ± 2.1	0.4	Tomono et al. (2001)
18.5	20.2 ± 3.4	0.4	Tomono et al. (2001)

¹ published in Schartmann et al. (2005),

Table 3.2.: Parameters of our NGC 1068 clumpy torus model.

Torus	Model Value	Clouds	Model Value
L_{AGN}	$7.2 \times 10^{44} \text{ erg s}^{-1}$	$R_{cl}(r)$	$0.01 \text{ pc} \times \left(\frac{r}{r_{\text{sub}}}\right)^{1.5}$
r_{sub}	0.28 pc	N_0	10
d	14.4 Mpc	τ_{cl}	$40 \times \left(\frac{r}{10 r_{\text{sub}}}\right)^{-0.8}$
$\eta_r(r) \propto r^a$	$a = -1.5$	dust	see Sect. 2.2.2
$H(r)$	$0.6 r_{\text{sub}} \times \left(\frac{r}{r_{\text{sub}}}\right)$		
r_o	$70 r_{\text{sub}}$		
i	55°		

which can occur when modeling SEDs only. Since modeling of the visibilities appears quite important, some further modeling efforts are presented in Sect. 3.3.

In the NIR, nuclear visibilities and images have been obtained using Speckle interferometry (Wittkowski et al. 1998; Weigelt et al. 2004). The baselines covered by these observations with the SAO telescope are in the range of 0 – 6 m. The visibility and images show clear asymmetry towards the north, parallel to the jet axis (see Fig. 3.2). While it is not clear if the Northern extension of ~ 39 mas is directly related to torus, the direction perpendicular to the jet axis is considered as a size constraint for the torus in the K -band. Accordingly, the torus diameter perpendicular to the jet is 18 mas or 1.3 pc. In addition to the speckle and MIDI observations, it was possible to observe NGC 1068 with the VLTI/VINCI instrument in the K -band (Wittkowski et al. 2004). The obtained visibility of ~ 0.4 at a projected baseline of 46 m corresponds to a structure that is smaller than 3 mas or $\lesssim 0.2$ pc; i.e., at least ~ 10 times smaller than the resolved ~ 30 mas nucleus in PA 45° . The large visibility of 0.4 at 46 m baseline can be explained by at least two different types of structures within the 18×39 mas core: (1) a single compact object (in addition to the 18×39 mas core) with a diameter in the range of 0 and 3 mas, or (2) several objects with diameters in the range of 0 and 3 mas. Since there is only one visibility point currently available in the K band at long baselines, it is not yet possible to decide whether this substructure consists of one or several $\lesssim 0.2$ pc objects. One possible explanation for this substructure is “*graininess*” due to clumpiness, as seen in the images in Figs. 2.8 and 3.6. The corresponding K -band visibilities of our model are shown in Fig. 3.4. Another possible explanation is that we see the central accretion flow viewed through only moderate extinction directly (Wittkowski et al. 2004). Some more detailed discussion on the origin of this high K -band visibility is given in Chapters 4 & 5.

Fig. 3.6 presents model images of our clumpy torus model of NGC 1068 (see Table 3.2). These model images are calculated for the wavelength ranges $2.1 - 2.3 \mu\text{m}$, $4.7 - 5.0 \mu\text{m}$, and $9.5 - 10.3 \mu\text{m}$, which approximately correspond to K -, M -, and N -bands, respectively. The images in the upper row are obtained for one particular random cloud arrangement, whereas the images in the lower row are the average brightness distributions as simulated from ~ 200 different random cloud arrangements. The *grainy structure* in the images in the upper row is caused by the *clumpiness* of the torus and is characteristic for the clumpy torus structure. We note that at this stage of modeling, the actual size of the clouds is not considered in the images. For the pixel resolution shown in Fig. 3.6, however, it is not significant.

Table 3.3.: Comparison between observed interferometric sizes and clumpy torus model sizes.

Band	model size	interf. size	Reference
H	2.1 ± 0.5 pc	1.3×3.1 pc	W04
K	2.0 ± 0.3 pc	1.3×2.7 pc	W04
N	2.7 ± 1.0 pc	$< 2.1 \times 3.4$ pc ¹	J04

W04 (Weigelt et al. 2004), J04 (Jaffe et al. 2004)

¹ warm component: 2.1×3.4 pc; hot component: < 1 pc

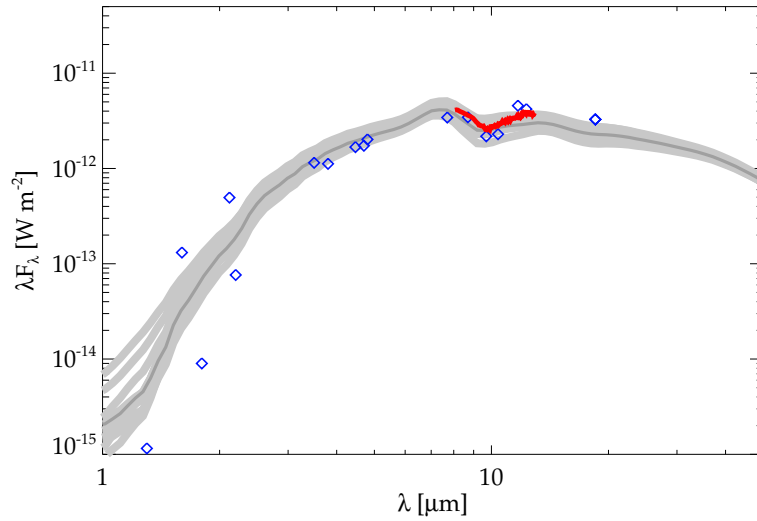


Figure 3.3.: Comparison between the observed high-resolution SED of NGC 1068 (blue diamonds and red curve) and our model SED (model parameters in Table 3.2). The red line represents the total MIDI flux (Jaffe et al. 2004). The shaded area shows the range of model SED variations obtained for 10 different random cloud arrangements. The dark grey line is the average of the 10 individual model SEDs.

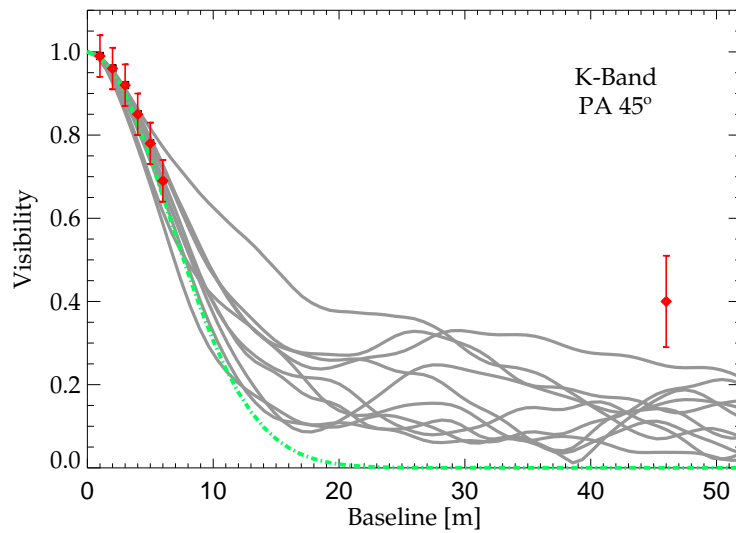


Figure 3.4.: Comparison between the *K*-band model visibilities (grey lines; model parameters of Table 3.2) for 10 different random cloud arrangements and the observed visibilities (red symbols) at 0-6 m and 46 m baseline at PA 45°. The green dashed-dotted line shows a Gaussian profile with 28 mas FWHM (=2.0 pc; see Table 3.3).

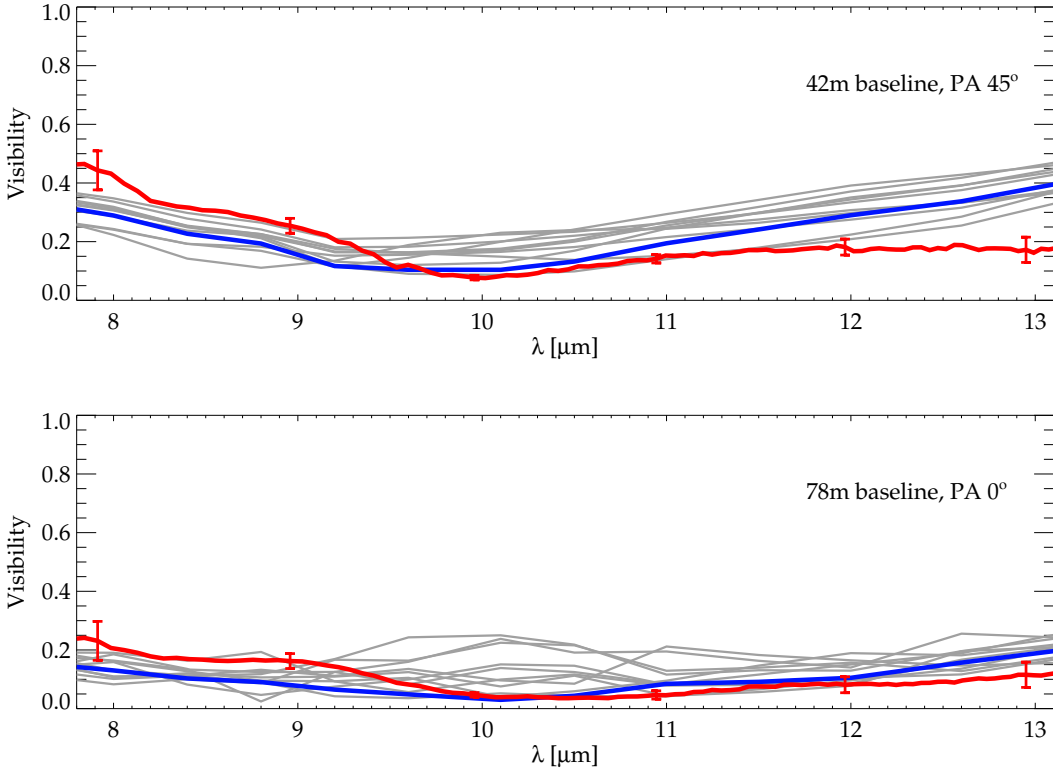


Figure 3.5.: Comparison between the observed NGC 1068 MIDI visibilities (red line) at projected baselines of 42 m (upper panel) and 78 m (lower panel), and our model visibilities (model parameters in Table 3.2). The grey lines show the visibilities for 10 different random cloud arrangements. The blue line represents the average model visibility.

Finally, it is possible to compare the resolved H -, K -, and N -band sizes of the compact core of NGC 1068 with the size predictions of our model described in Table 3.2. From the model images, we derived FWHM diameters (Gaussian model fits) of 2.1, 2.0, and 2.7 pc for the H -, K -, and N -band model diameters. The comparison (Table 3.3) with the interferometrically observed H -, K -, and N -band diameters (1.3×3.1 pc, 1.3×2.8 pc, and $< 2.1 \times 3.4$ pc, respectively) shows that the observed and modeled diameters are roughly in agreement. In other words, our model allows us to simultaneously reproduce *both* the observed SED and the H -, K -, and N -band diameters of NGC 1068.

3.3. Improvement of the visibility fit

Since visibilities appear to be an important constraint for distinguishing the various torus models, we have put some further effort in improving the model fit to the interferometric data. In particular, we attempted to find a model which has a comparable

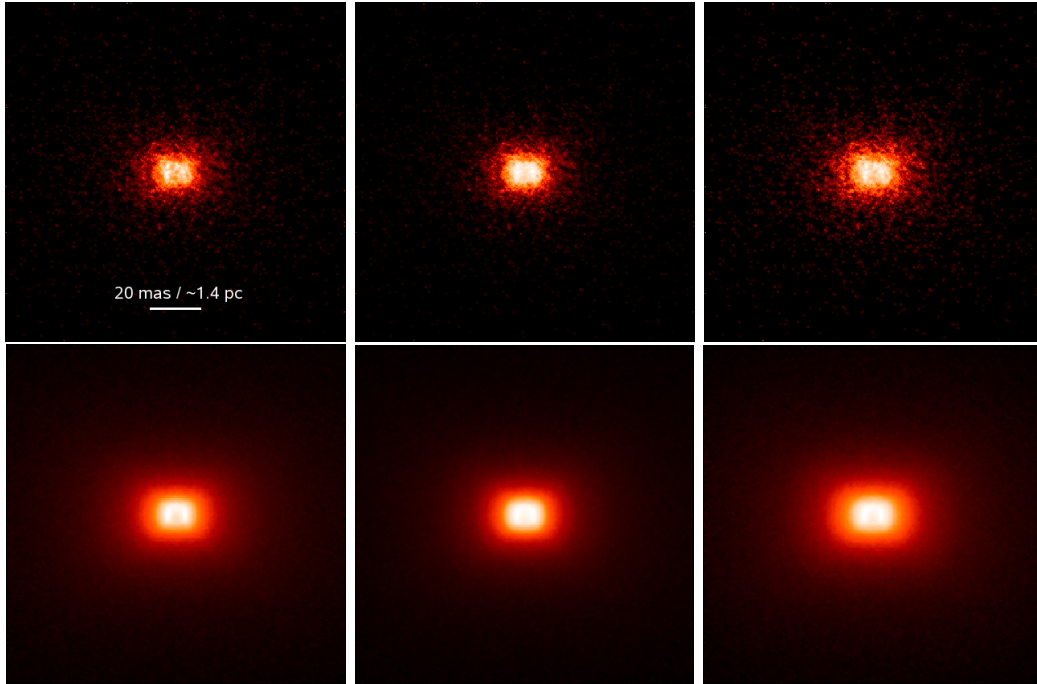


Figure 3.6.: NGC 1068 model images of our clumpy torus model described in Table 3.2. From left to right: K -, M -, and N -band images for an inclination angle of $i = 55^\circ$. The upper row shows images obtained for one particular random cloud arrangement, whereas the images in the lower row are averages of over ~ 200 different random cloud arrangements. The *grainy structure* in the images in the upper row is caused by the *clumpiness* of the torus.

high visibility at long baselines in the K -band, and simultaneously fits the correlated fluxes of MIDI in the mid-infrared.

There is some room for fitting different models to the observed photometric data as presented in Sect. 3.2. In the H and K band, some discrepancy exists between the AO and Speckle photometry. It is known that AO photometry can suffer from flux losses due to non-perfect AO correction. As a result, part of the flux which should be attributed to the central peak is smeared out in a “speckle halo”, and the nuclear flux is underestimated. This is particularly true for extended objects as NGC 1068. For that reason, we previously selected a model that fits in between Speckle and AO measurements, as a compromise (see Fig. 3.3). On the other hand, the Speckle visibilities show some extension in the direction of the jet and outflow cone which is tilted with respect to the MIDI observations by $\sim 30^\circ$ (Jaffe 2006). This may suggest that there is additional dust in the outflow which is not directly related to the torus. This dust component can scatter light of the accretion disk and torus into our direction, so that the observed NIR fluxes are a combination of torus scattered and re-emitted light and scattered light from the outflow region. This would affect both Speckle and

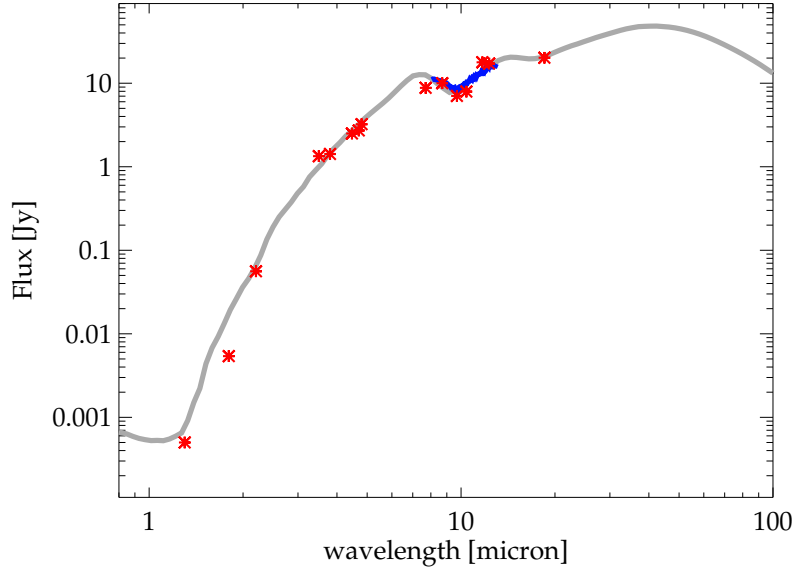


Figure 3.7.: Comparison of the NGC 1068 SED (red asterisks: photometry; blue line: MIDI total flux) with our alternative model which was specifically selected to improve the visibility fit.

AO photometry. In consequence, the “real” fluxes coming from the torus would be less than the observed ones.

In our improved visibility model, we try to fit the lower fluxes from the AO data to account for the possible contamination by scattered light from the outflow. The same geometric model parameters (i.e., cloud size distribution, radial and vertical cloud distribution, and optical depth of the clouds) are used as in the models from Sect. 3.2. In contrast to the previous models, the AGN luminosity and the inclination angle are varied, and a specific random arrangement of clouds is selected where the colors in the NIR are consistent with the AO data. From that model, we simulated visibilities which account for the growth of cloud diameters with distance from the AGN.

In Fig. 3.7 we show a comparison between the observed high-resolution SED with only AO measurements in the J , H , and K bands, and our new model SED. For this new model, the AGN luminosity is assumed to be $L_{\text{bol}} = 2 \times 10^{45}$ erg/s and the torus is seen edge-on ($i = 90^\circ$). The model is in good agreement with the observations. K -band model visibilities for 0 – 50 m are shown in Fig. 3.8 (top). The specific arrangement of clouds is consistent with the error bars of the VLTI/VINCI observations at 46 m, although the modeled visibility is still smaller than 0.4. Nevertheless, the clumpy structure is able to cause high visibilities even at long baselines.

It is important to note that the model visibilities at long baselines are sensitive to the actual cloud arrangement. A slightly different arrangement can result in a different, lower visibility (see Fig. 3.4). Typical orbital velocities of clouds in the torus regime are of the order of 200 km/s (e.g., see Beckert & Duschl 2004). When assuming self-gravitational clouds which are limited in size by the shear of the gravitational potential,

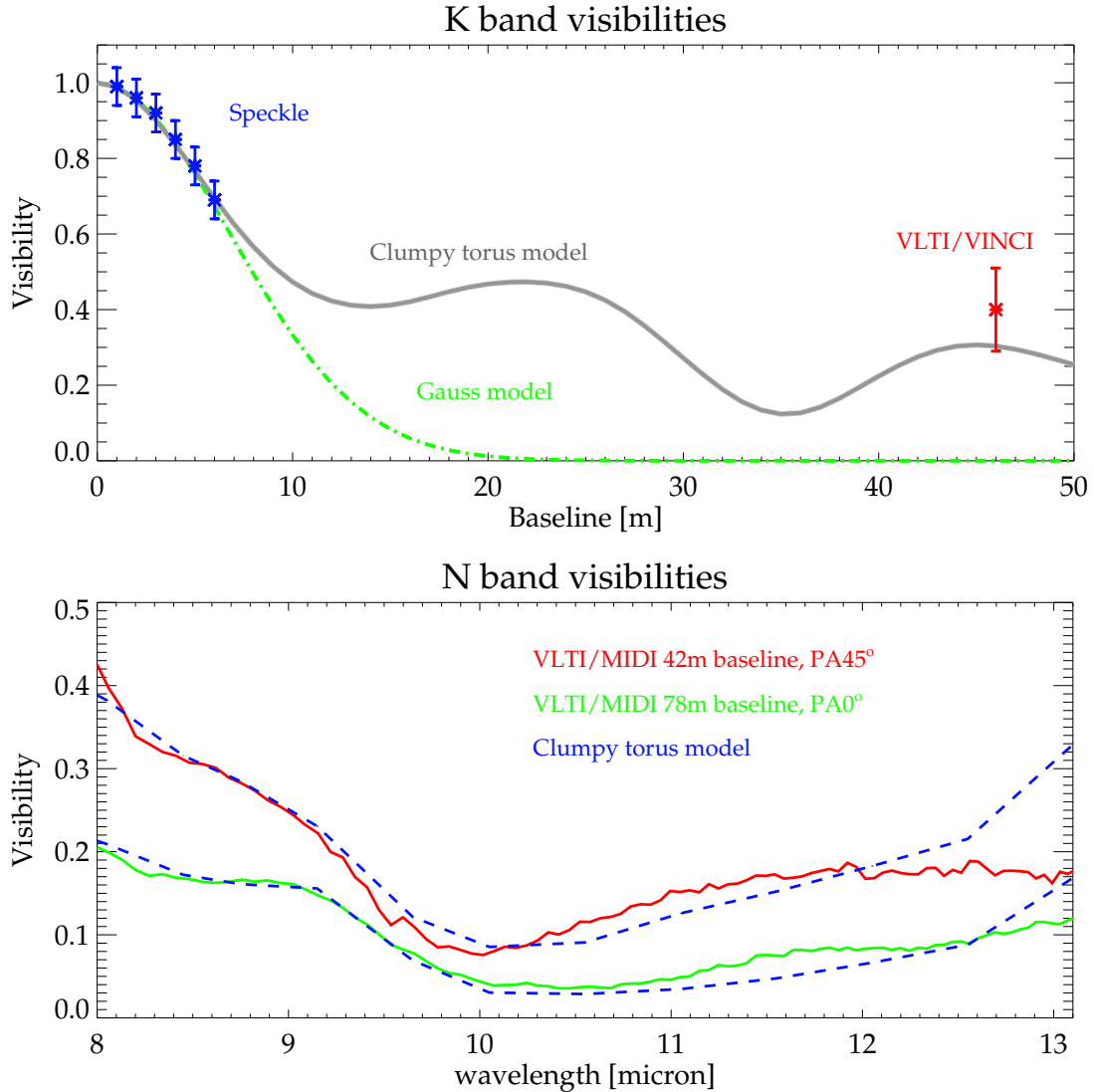


Figure 3.8.: Improved model fit to *K* and *N*-band visibilities of NGC 1068. **Top:** Comparison of observed Speckle and long-baseline *K*-band interferometry and predictions of our clumpy torus model. **Bottom:** Comparison between the VLT/MIDI spectro-interferometry of NGC 1068 for two different baselines (solid lines) and our clumpy torus model (dashed lines).

the cloud sizes, R_{cl} , at distance r from the AGN are of the order of $R_{\text{cl}}/r \sim 0.01 - 0.1$ (see Beckert & Duschl (2004), model parameters in Sect. 3.2, and for more details Chapter 5). For a sublimation radius of the order of 0.1 pc, which corresponds to typical Seyfert AGN luminosities, this means that a cloud passes over a fixed position in ~ 5 years. If we assume that of the order of 10 clouds are on the line of sight from the AGN to the observer, an order of magnitude “*reconfiguration time scale*” for the internal torus structure can be estimated which is several months to few years. Thus, when comparing to observations, the clumpy models predict that the observed long-baseline visibilities in the K -band can change on this time scale. As a consequence, visibilities observed at different epochs have to be compared with some caution concerning possible variation.

Improved N -band visibility models in the wavelength range of $8 - 13 \mu\text{m}$ are shown in Fig. 3.8 (bottom). The particular arrangement of clouds is in better agreement than what has been shown in Fig. 3.5. For the N -band, similar phenomena are observed as for the K -band, i.e., reconfiguration of the cloud arrangement can cause significant differences in the observed long-baseline visibilities. This was already illustrated by the set of 10 different cloud arrangements in Fig. 3.5, which shows very different visibility shapes at long baselines. In consequence, different objects can appear quite different in the N -band visibility spectrum. For example, recently Tristram (2007) showed VLTI/MIDI visibility spectra for the nucleus of the Circinus galaxy. The wavelength-dependent shape is very different from those observed for NGC 1068. Nevertheless, Tristram (2007) finds evidence for a clumpy structure of the Circinus torus. It will be an important future task to also model the observed Circinus visibilities with our clumpy torus model.

3.4. Summary and Conclusions

We applied our 3-dimensional clumpy torus model (see Sect. 2) to high-resolution spatial observations of the nucleus of NGC 1068. In particular, we aimed for simultaneously reproducing the observed photometric SED and the interferometric observations in the NIR and MIR. It was suggested that the observed wavelength-dependency of the $8 - 13 \mu\text{m}$ visibilities as observed with VLTI/MIDI are not consistent with smooth dust torus models, but with a clumpy torus structure. This suggestion has been quantitatively tested for the first time.

We presented a model which simultaneously reproduces the SED and NIR and MIR visibilities of NGC 1068. The model is geometrically characterized by a radial $r^{-1.5}$ -distribution of the clouds, a constant scale height $H \propto r$, and an inclination of the torus axis towards the line of sight of $i = 55^\circ$. For the AGN luminosity, we assume $\sim 7 \times 10^{44} \text{ erg s}^{-1}$. The clumpy torus model SED is in reasonable agreement with the AGN. N -band model visibilities follow the trend of deeper silicate absorption features at long baselines as compared to the total flux which was an important result from the MIDI interferometric observations. In addition, we also show that the high VLTI/VINCI K -band visibility at 46 m can be explained by the random arrangement of cloud inside the torus.

Since it was the first time that visibilities of AGN dust tori have been modeled, we put some further effort to improve the model fit of the interferometric data. When using a slightly different AGN luminosity, inclination, and random cloud arrangement ($L = 2 \times 10^{45} \text{ erg s}^{-1}$, $i = 90^\circ$), a better model to the K and N -band interferometry has been found. Based on the different model visibilities for various random cloud arrangement for a given set of parameters, it is well possible that the observed visibilities for a certain baseline configuration change on a time scale of several months or years. A detailed study on how the IR observations and the clumpy torus model can be interpreted in terms of the available multi-wavelength observations of the nucleus of NGC 1068 is presented in the next chapter.

4. A Multi-wavelength Analysis of the NGC 1068 SED

This chapter is based on work published in the paper

Hönig, S. F., Prieto, M. A., Beckert, T. 2007, A&A, in preparation

4.1. Introduction

The nucleus of the nearby Seyfert 2 galaxy NGC 1068 was the prime target of the most recent high-spatial resolution instruments in all wavelength regimes from the optical, through infrared into the Radio. For the first time, it is possible to build up a genuine nuclear spectrum of the immediate vicinity of the AGN. Furthermore, as described in previous chapters, near- (NIR) and mid-infrared (MIR) interferometric observations resolved the nuclear IR emission source (Wittkowski et al. 1998; Weigelt et al. 2004; Jaffe et al. 2004). It is supposed that the nuclear Radio emission comes from an accretion disk corona or an associated jet (Gallimore et al. 1996) while the infrared emission is more likely caused by thermal dust emission in the circumnuclear dusty torus (e.g., Hönig et al. 2006, and Chapter 3).

It is, however, as yet unclear how much each component contributes at different wavelengths. MIR VLTI/MIDI interferometric observations by Jaffe et al. (2004) show that approximately 20% of the MIR emission originates from an unresolved source $\lesssim 0.7$ pc. Wittkowski et al. (2004) report that *K*-band interferometry with the VLTI/VINCI instrument at 46 m baseline reveals a surprisingly high contribution of 40% to the whole nuclear flux by an unresolved source of $\lesssim 0.3$ pc. This can be explained by either radiation from a small compact source which is associated to the nuclear Radio spectrum (e.g., Wittkowski et al. 1998), or by substructure inside the dust torus (“clumpy torus”; Hönig et al. 2006).

In the following study, we use the combination of high-spatial resolution photometry, radiative-transfer simulations in the IR, and power-law models in the Radio to compare the extrapolated Radio emission to measurements at IR wavelengths. In Sect. 4.2, we summarize the observational data used for our study. In Sect. 4.3, we describe the models which were used for the Radio and IR regimes, respectively. In Sect. 4.4, we discuss the model results and analyze the maximum contributions of the Radio component to the observed NIR and MIR emission of diffraction-limited and interferometric data. We argue that the MIR is dominated by thermal dust emission from the torus while the situation in the NIR is inconclusive. In Sect. 4.5, the contribution of the accretion disk to the IR spectrum is quantified and compared to the interferometric VLTI/VINCI observations. In Sect. 4.6, we summarize our results.

Table 4.1.: High spatial resolution observations of the nuclear emission of NGC 1068 from the Radio to the infrared regime.

Frequency	Flux [Jy]	spatial scale [mas]	Reference
2.30×10^{14}	0.0084	78	this work
1.76×10^{14}	0.022	130	this work
1.36×10^{14}	0.098	78	this work
1.24×10^{14}	0.32 ± 0.03	78	this work
7.90×10^{13}	1.5	700	[1]
6.70×10^{13}	2.5	162	this work
3.75×10^{13}	4.23	200	[2]
3.0×10^{13}	3.33	200	[2]
2.5×10^{13}	7.1	200	[2]
1.6×10^{13}	9.6	290×180	[3]
1.2×10^{13}	9.4	200	[2]
2.3×10^{11}	0.022 ± 0.008	1000×600	[4]
1.15×10^{11}	0.023 ± 0.05	1400	[4]
4.3×10^{10}	0.019 ± 0.003	75	[5]
2.25×10^{10}	0.016 ± 0.006	75	[5]
8.4×10^9	0.0054 ± 0.0002	4.7×2.1	[6]
5.0×10^9	0.0091 ± 0.0002	4.7×2.1	[6]
5.0×10^9	0.0051	14×3	[7]
$< 1.7 \times 10^9$	0.0026	14×12	[7]
$< 1.4 \times 10^9$	6×10^{-5}	16.0×7.6	[6]

[1] Marco & Brooks (2003); [2] Bock et al. (2000); [3] Tomono et al. (2001); [4] Krips et al. (2006); [5] Gallimore et al. (1996); [6] Gallimore et al. (2004); [7] Roy et al. (1998)

4.2. Observations

The location of NGC 1068's nucleus is assumed to be at the center of a 0.8 pc size, disk-like Radio structure known as S1, resolved at 5 and 8.4 GHz by Gallimore et al. (2004). In the mid-IR, a Gaussian decomposition of VLTI/MIDI interferometry data sets an upper limit of $0.7 \text{ pc} \times < 1 \text{ pc}$ on the size of the central source at wavelengths $< 10 \mu\text{m}$ (Jaffe et al. 2004). At $2 \mu\text{m}$, both speckle observations (Weigelt et al. 2004) and VLTI/VINCI interferometry (Wittkowski et al. 2004) confirm the presence of a compact core with FWHM $\sim 0.4 \text{ pc}$. Shortward of $1 \mu\text{m}$, the NGC 1068 nucleus is fully obscured and undetected.

The Radio to IR SED of NGC 1068's nucleus is extracted from the best sub-arcsec photometry currently available for this source. Overall, we sample spatial scales at Radio, mid- and near-IR, and optical wavelengths down to few parsecs. Radio data from source S1, which is assumed to be NGC 1068's nucleus, is taken from the VLA 75 mas beam (Gallimore et al. 1996) and VLBA-observation (Roy et al. 1998; Gallimore et al. 2004). The millimeter data at 1 mm and 3 mm are taken from Krips et al. (2006) and correspond to a beam size of $1'' \times 0.6''$. Because of the possible contribution of

the jet in the 3 mm data, only the peak value as specified by Krips et al. (2006) is considered.

Data in the 8 – 25 μm range are taken from Bock et al. (2000) and Tomono et al. (2001), using their reported fluxes in aperture diameters of ~ 200 mas. This high resolution was obtained by deconvolving their 10 m Keck and 8.2 m Subaru images, respectively. It is important to note that both sets of deconvolved-extracted fluxes differ by $< 30\%$.

Interferometry data from VLTI/MIDI in the 8 – 13 μm has been taken from Jaffe et al. (2004). For our study, we used the correlated fluxes from the 78 m baseline which provides the highest resolution IR data which is currently available. The visibilities show that the silicate absorption feature becomes more pronounced at longer baselines. This was interpreted as an indication for clumpy substructure within the dust torus (Jaffe et al. 2004; Hönig et al. 2006, see also Chapter 3). 5-20% of the total flux are unresolved at the 78 m baseline.

In the 1 – 5 μm range, we use our adaptive optics images acquired with VLT/NACO, except for the *L*-band photometry which was taken from Marco & Brooks (2003). The spatial resolution achieved in these observations varies from FWHM ~ 78 mas in the 1.3 – 2.44 μm range to FWHM ~ 160 mas in the *M*-band. Nuclear fluxes were integrated over an aperture size comparable to those resolutions. These aperture sizes were selected to minimize the contribution from the prominent IR diffuse emission surrounding the nucleus of NGC 1068. The 1.3 μm data should be considered as an upper limit. The corresponding frequency is the highest at which the core of NGC 1068 can be reliably distinguished from the strong extended emission. All observations are listed in Table 4.1. We note that these are different from what has been used in the previous chapters due to the different aim of this study and new available data, especially in the NIR.

NGC 1068 is Compton thick in the X-ray regime. It shows prominent extended soft X-ray emission as seen in *Chandra* images (Young et al. 2001). The extended emission is preferentially distributed along the ionization cone. *XMM-Newton* spectra show that most of this emission is resolved in multiple emission lines and not much continuum is detected (Kinkhabwala et al. 2002). Due to the Compton thickness of the source and extension of the emission, we do not include X-ray photometry in our modeling of the nucleus.

4.3. Models

We focused our modeling efforts on two components: (1) the near- and mid-infrared component in the range of $10^{13} - 10^{14}$ Hz, and (2) the Radio component at frequencies from 10^9 Hz to 10^{11} Hz. Our aim is to quantify the contribution of each component in different wavelength regimes.

4.3.1. IR torus model

For the infrared regime of the NGC 1068 SED, we use the clumpy torus models of Hönig et al. (2006). With these models, we aimed at fitting the photometric data

from $1.2 - 23 \times 10^{13}$ Hz, simultaneously with the 78 m baseline data as observed with VLTI/MIDI. A grid of models has been calculated where we tested different radial cloud distributions (radial distribution function $\propto r^{-1.0, -1.5, -2.0}$), inclination angles, and average numbers of clouds in an equatorial line of sight. For each set of model parameters we simulated 10 different random arrangements of clouds. This accounts for the variation in SEDs which occurs due to the actual cloud distribution. Our best-fitting model is shown as blue-dashed lines in Figs. 4.1 & 4.2.

The modeled torus has a line-of-sight inclination of 90° , which corresponds to an edge-on view of the torus. In radial direction, the clouds are distributed according to a power-law of $r^{-1.5}$, which is well consistent with clumpy torus accretion scenarios where the torus is located in the sphere of influence of the central supermassive black hole (Beckert & Duschl 2004). We assumed a constant scale height, H/R , throughout the torus, so that no vertical flaring occurs. The half opening angle of our geometrical configuration is $\sim 40^\circ$. Although an r -dependent H/R could have been chosen, it has already been tested in Hönig et al. (2006, 2007) and no better fit was found then. Furthermore, theoretical considerations and observational studies of clumpy tori seem to favor non-flaring geometries (Hönig & Beckert 2007; Polletta et al. 2007, , see Chapters 6 & 7). The obscuration of the nucleus is characterized by an average of 10 optically thick dust clouds along the line of sight to the observer. The observed and modeled size of the dust torus is $\sim 20-30$ mas ($\sim 1.4-2$ pc), depending on wavelength and orientation. To fit the observed fluxes, a bolometric luminosity of the central AGN of 2×10^{45} erg s $^{-1}$ has been inferred.

4.3.2. Radio models

In the Radio regime at frequencies lower than 1 THz, we used two different $F_\nu \propto \nu^\alpha$ power-laws with $\alpha = 1/3$ (Fig. 4.1) and $\alpha = 0$ (Fig. 4.2), and exponential cutoffs at low frequencies. They are now described in more detail.

Synchrotron radiation. The Radio data of NGC 1068 shows a slightly inverted spectrum ($\alpha > 0$) from low to higher frequencies, with an apparent turnover at $\sim 10^9$ Hz. By using the data in the full range between 5×10^9 Hz and 3×10^{11} Hz, we obtain a slope of $\alpha = 0.29 \pm 0.07$ from a least-square fit. This is consistent with a power law index of $\alpha = 1/3$, which can be produced by optically thin Synchrotron radiation coming from quasi-monoenergetic electrons (Beckert et al. 1996). In such a scenario, the emission is characterized by $F_\nu \propto \nu^{1/3} \exp(-\nu/\nu_c)$, with an exponential turnover, ν_c , at high frequencies. Due to our goal of estimating the maximum possible influence of the Radio emission source to the IR, we assume that $\nu_c > 300$ THz, so that the high-frequency cutoff can be neglected hereafter, since it doesn't occur in the frequency range we are interested in. At low frequencies, a turnover can occur if the Synchrotron source is located within thermal plasma without significant free-free emission. Thermal free-free absorption becomes important when the optical depth of the free-free plasma, $\tau_{\text{ff}} \propto \nu^{-2.1}$, becomes > 1 (e.g., Beckert et al. 1996). In this case the Synchrotron emission from the center will experience free-free absorption. As a result, the Synchrotron

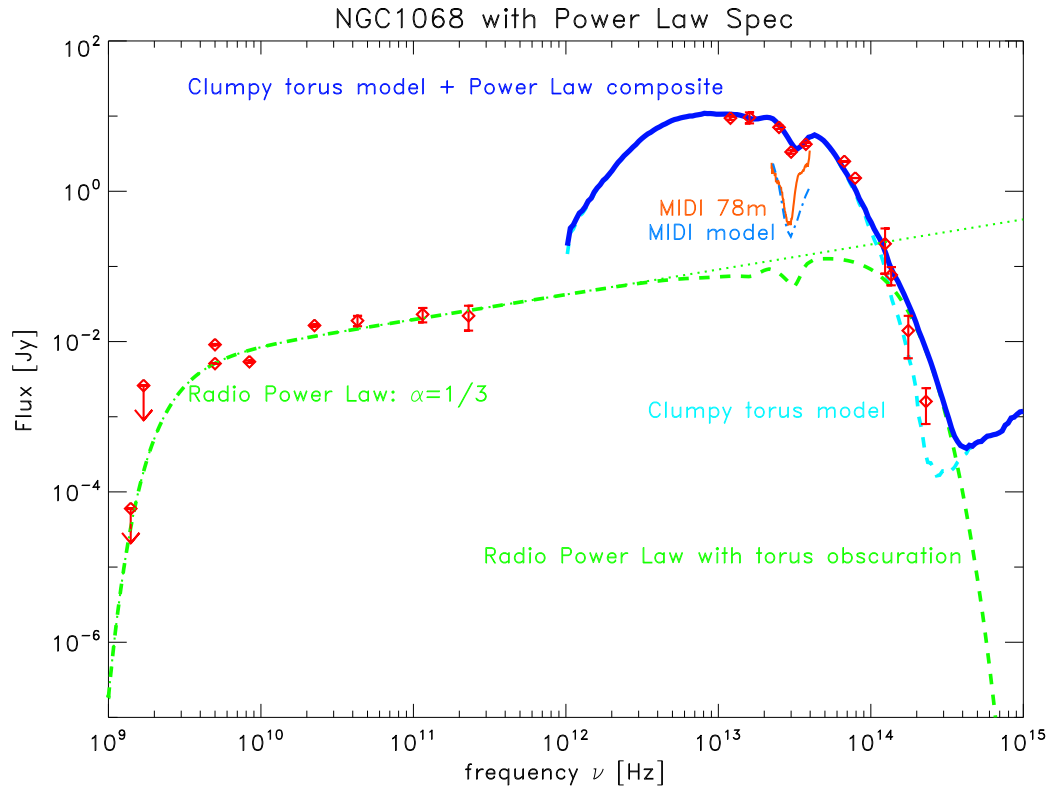


Figure 4.1.: High-spatial resolution SED of the nucleus of NGC 1068, in comparison to thermal dust emission from a torus in the IR and non-thermal Synchrotron emission in the Radio. The blue-dashed line shows the clumpy torus model that was used in this study (Hönig et al. 2006) to model the single-dish IR photometry (diamonds) and interferometric observations by VLTI/MIDI (orange solid line; model: dashed-dotted blue line). The Radio data (diamonds) are modeled by a spectrum $F_\nu \propto \nu^{1/3} \exp(-(\nu/\nu_{\text{ff}})^{-2.1})$ (Synchrotron + free-free absorption; green-dotted line), extrapolated into the infrared and attenuated by the torus obscuration (green-dashed line). The total model spectrum (torus model + Radio spectrum) is shown by the dark blue solid line.

spectrum has to be modified by a factor $\exp(-(\nu/\nu_{\text{ff}})^{-2.1})$, with the low-frequency turnover at ν_{ff} , implicitly defined by τ_{ff} .

In Fig. 4.1, we compare the Synchrotron model SED with observed Radio fluxes. The low-frequency free-free absorption turnover occurs at $\nu_{\text{ff}} = 3$ GHz which is consistent with the upper limit on detections around 1 GHz. For NGC 1068, the possibility of Synchrotron emission from quasi-monoenergetic electrons was already explored, e.g., by Gallimore et al. (1996) and Wittkowski et al. (1998), but with less Radio data available. In addition, similar power laws have been found for other galactic nuclei as Sgr A* (Beckert et al. 1996) or M81 (Reuter & Lesch 1996). According to Wittkowski et al. (2004), such an emission mechanism would require a source size of the order of 100 AU and electron densities of 10^3 cm^{-3} , which is consistent with our analysis. As a result, the observed Radio emission would probably come directly from the AGN.

The turn-over frequency ν_{ff} between the optically thick and optically thin case allows us to estimate the emission measure, E , for the free-free plasma. Assuming a gas temperature of 10^4 K, we obtain a corresponding emission measure $E = 3 \times 10^7 \text{ pc cm}^{-6}$ at $\nu_{\text{ff}} = 3$ GHz. Beckert et al. (1996) found $E = 10^6 \text{ pc cm}^{-6}$ for the Galactic center, with $\nu_{\text{ff}} = 0.8$ GHz and a temperature of 6000 K. The discrepancy can be explained by higher gas densities in the vicinity of an AGN as compared to the Galactic Center.

A second possibility for the low-frequency turnover is Synchrotron self-absorption (SSA) within the emission source. This would result in a turnover spectrum from the optically thin to the optically thick case according to $F_{\nu} \propto \nu^2$ (for mono-energetic electrons; in the case of a power law extending to lower electron energies, $F_{\nu} \propto \nu^{5/2}$), which is less steep than the free-free absorption. Given the detection of S1 in NGC 1068 at 5 GHz, and the upper limits at ~ 1.5 GHz, the turnover should occur in-between. The observed lower limit for the power law index in this frequency range ($\alpha \gtrsim 3.5$), however, seems to favor the free-free absorption scenario over SSA. Furthermore, optically thin Synchrotron emission from monoenergetic electrons and optically thick SSA would be almost contradictory.

Free-free emission. The fluxes at the highest Radio frequencies > 100 GHz are consistent with a flat spectrum, i.e. $F_{\nu} \propto \nu^0$. This opens the possibility that the Radio spectrum is produced by optically thin thermal free-free emission. A comparison between observed data and the flat thermal free-free spectrum with a low-frequency free-free absorption cutoff at $\nu_{\text{ff}} = 6$ GHz is shown in Fig. 4.2. This scenario has already been investigated by Gallimore et al. (1996). Due to the then limited amount of data, it was thought to be a more likely scenario for the southern Radio source S2. For the nuclear Radio source S1, the spectral index seemed to be not consistent with a flat power-law. The slope of the S1 data in our compilation leaves some margin for such an interpretation, e.g., by considering the different apertures at different frequencies which could result in a flux over-estimation at the higher frequencies.

4.4. The influence of the Radio components to the IR

Since there is a gap between the 100 GHz and 10 THz regime, it is difficult to judge how the IR and Radio components are connected. In particular, a high frequency

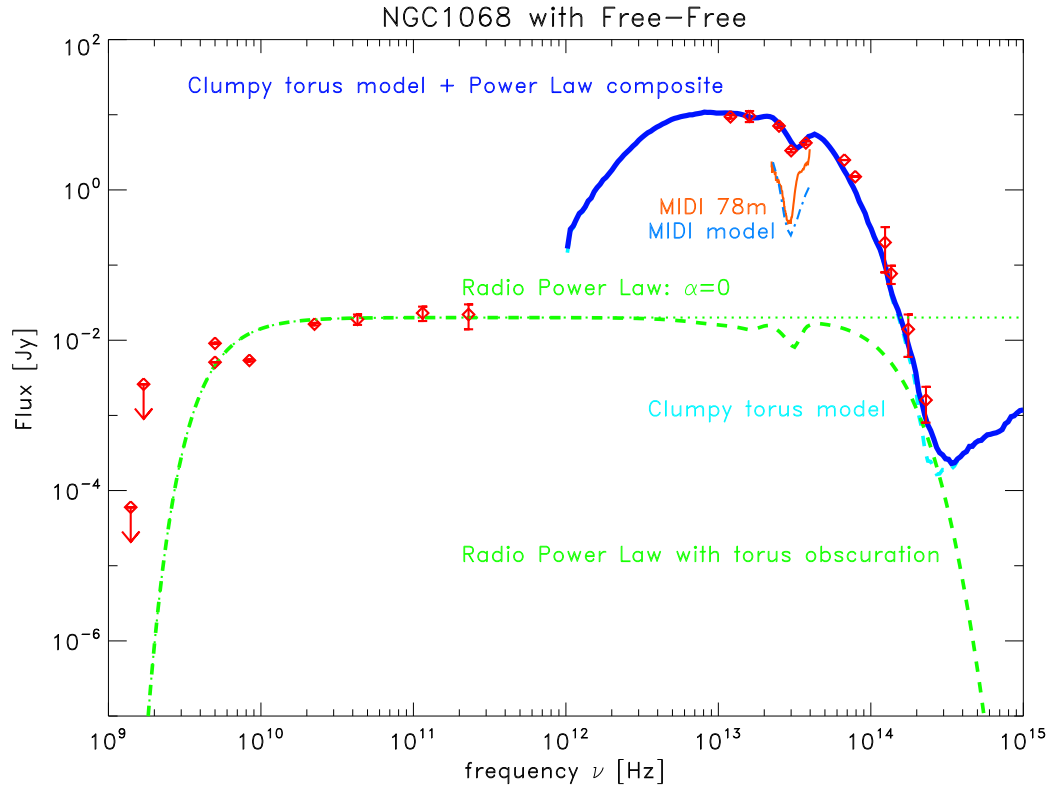


Figure 4.2.: Same as Fig. 4.1, but with optically thin free-free emission in the Radio (flat spectrum with power-law index $\alpha = 0$).

turnover for the Radio component cannot be determined from the existing data. As a consequence, the possibility exists that the Radio source also contributes to the IR. This leaves two open questions: (1) Is the unresolved flux in the long-baseline MIR data from VLTI/MIDI coming from the central AGN? (2) Can the Radio source (especially a possible Synchrotron source) be responsible for a significant fraction of the NIR flux? To answer these questions, we have extrapolated the two investigated Radio models into the IR regime (Figs 4.1 & 4.2, green dotted lines). We assume that the Radio source is surrounded by the dusty torus. As a result, it will suffer from extinction by the dust within the torus (green dashed lines).

As can be seen from the plots, the maximum possible extrapolated MIR flux of the Synchrotron and free-free power law is still a factor of 5-10 below the unresolved 78 m baseline MIDI flux. As a conservative limit, we determined a maximum flux contribution of the Radio source to the correlated MIR flux $F_{\text{Radio}}(\text{MIR})/F(\text{MIR}) \lesssim 0.2$. This means that the unresolved MIDI flux supposedly comes from the dust surrounding the AGN rather than from the AGN Radio component. This is consistent with the clumpy torus model for the long baseline (see also Hönig et al. 2006, 2007, and Chapter 3 for more details).

In the NIR, the situation is less clear. Although the clumpy torus model in Figs. 4.1 & 4.2 (light-blue dotted lines) is able to reproduce all of the NIR emission, it is pos-

sible that less NIR emission is actually coming from the torus. The reason is that in the clumpy torus picture, the NIR wavelengths are much more sensitive to the actual arrangement of clouds for the same set of model parameters (Hönig et al. 2006). While the extrapolated dust-obscured free-free spectrum is probably too weak at all NIR bands, the Synchrotron spectrum might contribute significantly to the J , H , and K -band fluxes, but only if it reaches from the Radio into the NIR. A similar suggestion has been made by Wittkowski et al. (1998) who report on Speckle interferometry of NGC 1068. They estimate that $\sim 50\%$ of the resolved nuclear K -band emission might originate from Synchrotron emission. The implied lower-limit angular size of the source from Synchrotron theory (assuming a spherical geometry) is given as 0.01 mas.

4.5. Quantifying the contribution of the accretion disk

Interestingly, interferometric VLTI/VINCI observations of NGC 1068 show that at a baseline of 46 m, $\sim 40\%$ of the observed K -flux comes from an unresolved source of size < 1 mas (Wittkowski et al. 2004). This can be interpreted either by viewing the central AGN directly (Wittkowski et al. 2004) or by individual clouds or cloud clumping inside the dust torus (Hönig et al. 2006).

We tried to figure out how much the accretion disk can actually contribute to the NIR and MIR. For that, we used a standard accretion disk spectrum of the shape $F_\nu \propto \nu^{1/3} \exp(-\nu/\nu_{\max})$ (e.g., Shakura & Sunyaev 1973). For that, we assume that no outer edge self-gravity cutoff occurs (e.g., Goodman 2003). The turnover frequency, ν_{\max} , is characterized by the accretion disk temperature at the innermost stable orbit ($\sim 3R_{\text{Schwarzschild}}$), which can be inferred from the mass of the central black hole ($M_{\text{BH}} \approx 10^7 M_\odot$, Greenhill et al. 1996) and the modeled AGN bolometric luminosity ($L = 2 \times 10^{45}$ erg/s, see Sect. 4.3.1). For NGC 1068, we obtain a temperature of approximately 1.5×10^6 K which corresponds to a frequency $\nu_{\max} \sim 8 \times 10^{16}$ Hz. We extended the accretion disk spectrum down to IR wavelengths, so that the integrated accretion disk spectrum equals the modeled AGN bolometric luminosity. This provides some estimate for the emission from the accretion disk, although it is completely obscured in the UV and optical.

In Fig. 4.3, we show a comparison of the observed fluxes with the clumpy torus model (Sect. 4.3.1), and the accretion disk spectrum which is extrapolated from the UV to the MIR (dotted line) and attenuated by the torus obscuration (dashed line). The obscured accretion disk spectrum is obviously not able to contribute significantly to the NIR or MIR emission. Only in the J -band, a contribution of up to 20% is possible. If the torus is indeed clumpy, there exists the possibility that the accretion disk is seen through “holes” in the torus of less or no obscuration. If this happens, it is possible that the accretion disk contributes significantly to the shortest wavelength bands in the NIR (J and H -band). On the other hand, the contribution in the K -band would be only $\leq 10\%$. Furthermore, if an average number of N clouds obscure the central accretion disk, the probability, $P(0)$, of viewing the disk through a hole is approximately $P(0) = \exp(-N)$ (Natta & Panagia 1984). For typically 5 – 10 clouds along the line-of-sight, this probability is less than 1%. Thus, it is not expected that

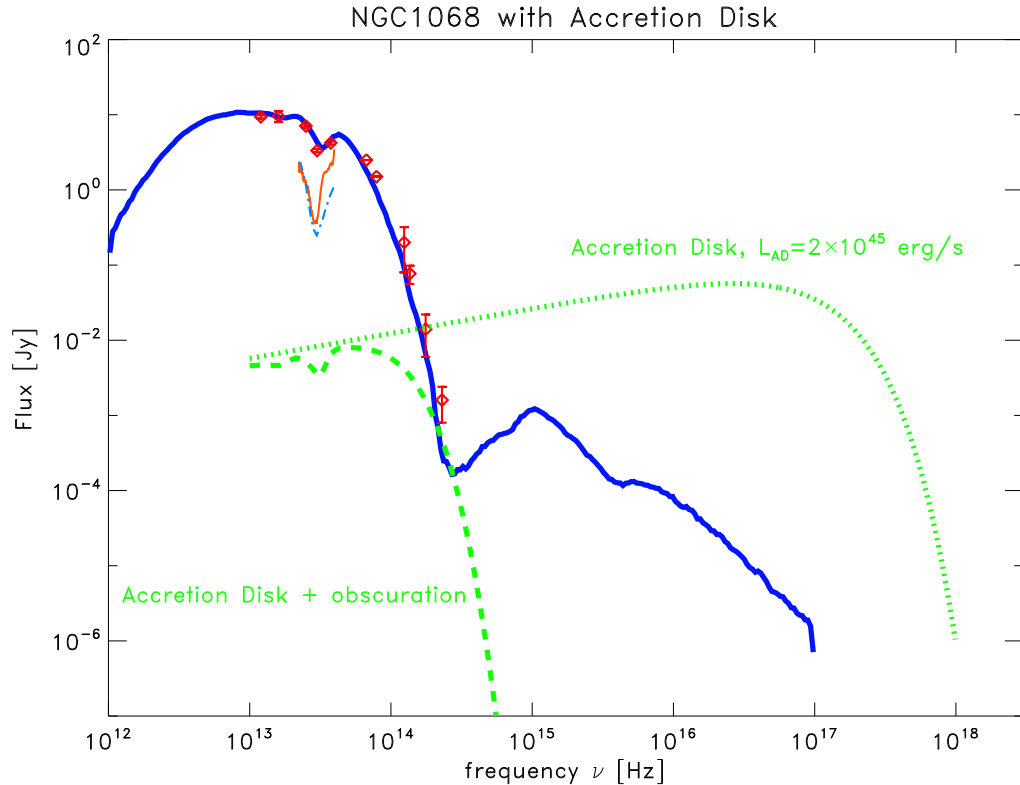


Figure 4.3.: Accretion Disk contribution to the IR spectrum. A standard accretion disk spectrum $F_\nu \propto \nu^{1/3} \exp(-\nu/\nu_{\max})$ was adjusted for the known parameters $L = 2 \times 10^{45}$ erg/s and $M_{\text{BH}} \approx 10^7 M_\odot$ of NGC 1068 (green dotted line) and attenuated for the torus obscuration (green dashed line).

the unresolved K -band flux as observed with VLTI/VINCI (40% of the total nuclear flux) originates from the accretion disk.

It is interesting to note that the slope of the Radio spectrum, $F_\nu \propto \nu^{1/3}$, agrees with the superposition of thermal black body spectra for an accretion disk. The modeled accretion disk spectrum, however, is offset from the Radio spectrum when extrapolating it to higher frequencies. Furthermore, if the Radio emission would come from the accretion disk, the highest Radio frequencies would correspond to temperatures of the accretion disk of 1-4 K. Thus, the expected disk size for NGC 1068 would be at least of the order of kiloparsecs, which is not reasonable and contradicted by observations (e.g. Gallimore et al. 2004).

4.6. Summary and Conclusions

We analyzed the SED of NGC 1068 from 10^9 Hz to 10^{14} Hz. The SED was modeled by two components: (1) an IR component which is represented by a clumpy torus model, and (2) a Radio component represented either by Synchrotron emission with

$F_\nu \propto \nu^{1/3}$, or optically thin free-free emission, $F_\nu \propto \nu^0$. For the infrared, we used our clumpy torus model to simultaneously reproduce the high-resolution NIR-to-MIR SED and the VLTI/MIDI correlated fluxes at 78 m baseline. The model is characterized by a radial cloud density distribution $\propto r^{-3/2}$ and a half opening angle of 40° . The torus has a constant H/R , and the central AGN is obscured by 10 dust clouds on average. For the Radio source, we showed that the power-law index of 0.29 ± 0.07 is consistent with a spectral slope proportional to $\nu^{1/3}$ which is expected from Synchrotron emission by quasi-monoenergetic electrons. In addition, there is some possibility that the spectrum comes from thermal free-free emission. Both Radio models require a low-frequency turnover around 5 GHz where the spectrum changes. The steepness in the range between 1 – 5 GHz suggests that the turnover is caused by a foreground screen of thermal plasma which becomes optically thick below $\sim 3 - 5$ GHz ($F_\nu \propto \exp(-(\nu/3 \text{ GHz})^{-2.1})$).

The main goal of this study was to spectrally disentangle the near- and mid-infrared dust emission from possible contamination by the Radio source. For that, we extrapolated the free-free and Synchrotron power laws to the infrared. It was possible to show that the Radio source is contributing less than 20% to the observed unresolved flux at 78 m baseline. Most of the flux is probably coming from unresolved structure inside the torus, e.g., as predicted by clumpy torus models. In the near-infrared, the situation is less conclusive. Although a clumpy torus model can account for the observed NIR emission, effects from the clumpy structure of the torus can cause the torus NIR emission to be significantly variable. As a consequence, there is still room for a strong contribution from the Radio source to the NIR. Actually, *K*-band interferometry at 46 m baseline show that $\sim 40\%$ of the observed flux comes from an unresolved source < 1 mas. This can be either caused by the compact Radio source's contribution to the NIR, or by dust clouds inside the torus. We also investigated the possibility that this unresolved flux may originate from the accretion disk. Using the modeled bolometric AGN luminosity and the known black hole mass of NGC 1068, we synthesized the expected accretion disk spectrum. From extrapolation into the IR, we concluded that the *K*-band contribution of the accretion disk should be less than 10%.

5. Dust Tori in Type 1 AGN

This chapter is based on work published in the paper

Kishimoto, M., Hönig, S. F., Beckert, T., Weigelt, G. 2007, A&A, 476, 713

In the framework of the PhD thesis, the clumpy torus model has been used for quantitative interpretation of the torus and accretion disk contribution to NIR photometry of type 1 AGN. Furthermore, modifications have been made to compare the model dust sublimation radii with reverberation measurements of the presumed inner torus boundary.

5.1. Overview and context

The emission from active galactic nuclei (AGN) in NIR and MIR wavelengths is generally thought to be dominated by the thermal emission from dust grains in the torus which surrounds the broad emission line region and the central engine. One of the main goals of high spatial resolution AGN studies is to resolve the innermost region of these tori. This could be done in Type 1 AGN where our line of sight is more or less close to the symmetry axis direction of the torus, and so the innermost region is directly seen. While IR interferometric observations have resolved at least some part of this torus structure in nearby AGN (Wittkowski et al. 1998; Weinberger et al. 1999; Swain et al. 2003; Weigelt et al. 2004; Wittkowski et al. 2004; Jaffe et al. 2004), most of the results obtained so far are for Type 2 objects where the symmetry axis of the torus is thought to have large inclinations to our line of sight and so the innermost region of the torus is not directly seen.

The inner boundary of the torus is set by sublimation of dust, and since the dust sublimation temperature is thought to be roughly $\sim 1500\text{K}$, the innermost region is mainly emitting in the near-IR. However, in Type 1s, some sizable part of the near-IR emission comes from the central engine, which is also directly seen along our line of sight. This will affect the measurement of the innermost region of the torus. The fractional contribution of the accretion disk is one of the key quantities in high spatial resolution studies of the innermost tori. In the following study, we try to quantify the contribution and its effect on the interferometric observations, based on the high spatial resolution HST/NICMOS images of nearby type 1 AGN which minimizes the effect of host galaxies.

In Sect. 5.2, we will describe the available HST/NICMOS sample and the measurement of the point source fluxes at multiple wavebands through two-dimensional decomposition. In Sect. 5.3, these point-source fluxes will be compared to simple blackbody colors and also to the colors of more realistic clumpy torus models, to evaluate the accretion disk contribution. In Sect. 5.4, we examine the expected innermost size of the

torus. Based on this discussion, we aim to clarify the current expectation for the interferometry of the innermost torus region in Sect. 5.5. We summarize our discussions in Sect. 5.6. When needed, cosmological parameters are assumed as $H_0 = 70\text{km/s/Mpc}$, $\Omega_m = 0.3$, and $\Omega_\Lambda = 0.7$.

5.2. HST/NICMOS images and point source flux

5.2.1. Sample description and data reduction

We have searched the HST archive for NICMOS observations of Type 1 AGN which are in the AGN catalog compiled by Véron-Cetty & Véron (2006), with spectral classifications S1.0 to S1.5 and redshift z up to 0.2. Simultaneously, HST observations at $J/H/K$ or H/K bands are required. Filters are mostly F110W, F160W, and F222M, with a central wavelength of $1.12\ \mu\text{m}$, $1.60\ \mu\text{m}$ and $2.22\ \mu\text{m}$, respectively. We further excluded radio-loud objects to avoid any possible contribution in the NIR from synchrotron components. Table 5.1 lists the objects found. For this sample, the physical linear size corresponding to the FWHM of the NICMOS Point Spread Function (PSF) at $2.2\ \mu\text{m}$ is less than $\sim 600\text{pc}$. The data were reduced and calibrated using the standard pipeline software CALNICA and CALNICB with the most recent reference files as of early 2007. The detector readout mode was MULTIACCUM. In this mode, each pixel in NICMOS detectors is read multiple times non-destructively during a single integration. The final count rate at each pixel is calculated in CALNICA by a least squares fit to the accumulating counts versus exposure times at each readout. This uses only non-saturated periods during the course of the single exposure for each pixel. Therefore, the brightest nuclear pixels have effectively short exposure times and do not suffer from saturation.

5.2.2. Nuclear flux measurements

We implemented a two-dimensional decomposition for the central $\sim 4 \times 4\text{arcsec}^2$ of each image using our software written in IDL. We used a model PSF generated by TinyTim (Krist et al. 1998) for the nuclear point source, and a model bulge component for an underlying host galaxy, convolved with the same model PSF. The bulge component assumes a de Vaucouleurs profile,

$$\Sigma(r) = \Sigma_e \times \exp \left[7.67 \left(1 - \left(\frac{r}{r_e} \right)^{1/4} \right) \right] \quad (5.1)$$

where $\Sigma(r)$ is the surface brightness at radius r from the peak, and Σ_e is the surface brightness at the half light radius r_e ¹. We then measured the total flux of the PSF component.

Generally, the point sources in NICMOS images can be well modeled by the TinyTim synthetic PSFs, but detailed PSF shapes depend on several factors, which have

¹The de Vaucouleur profile is well established for typical galaxy bulges. It is a special case of the more general Sérsic profile, $\Sigma(r) = \Sigma_e \cdot \exp \left[\kappa \left(1 - (r/r_e)^{1/n} \right) \right]$ with $\kappa \approx 2n - 0.331$ for $n \geq 2$ (Peng et al. 2002).

been investigated substantially by Krist et al. (1998) and Suchov & Krist (1998). To roughly estimate the discrepancies between synthetic and observed PSFs, we compared synthetic PSFs with the NICMOS images of the Galactic stars SA 107–626 and SA 107–627 taken with NIC1/NIC2 cameras with a few filters. These have been observed for the PSF measurements by Kukula et al. (2001, ; see also Veilleux et al. (2006) for notes on the latter star). For each stellar observation, we compared radial profiles of three images: (A) an absolute difference image between the synthetic and observed PSF with matched total counts; (B) a “standard-deviation image” σ_{pix} for the observed PSF, where each pixel consists of the standard deviation of the 3×3 pixel region centered on that pixel; (C) a statistical error estimate image σ_{stat} for the observed PSF from the pipeline. In the outer region, the pixel values of the σ_{pix} image B approaches those of the σ_{stat} image C as expected. In the inner region close to the PSF center, σ_{pix} is much larger than σ_{stat} , since the former rather represents the extent of small spatial scale structures of the PSF on top of the statistical photon noise. We found that the overall profile of the difference image A is roughly reproduced by taking the geometric mean σ_{mean} of image B and C, i.e. $\sigma_{\text{mean}} = (\sigma_{\text{pix}}\sigma_{\text{stat}})^{1/2}$. Thus, the average deviation of the observed image from the model PSF can approximately be described by this σ_{mean} .

This would also be applicable for our AGN images since a relatively smooth, underlying host component would not contribute much to the σ_{pix} image except for its photon noise. Therefore, we adopted this σ_{mean} image as an estimate for the average deviation of each observed AGN image from the model. In the two-dimensional fit, we weighted each pixel by $1/\sigma_{\text{mean}}^2$, after masking out obvious distinct structures in the host galaxies such as starburst knots in a few cases (e.g. NGC 7469). The σ_{stat} image is obtained from the pipeline software, and the σ_{mean} image can easily be generated from the observed image. The radial profile of the χ^2 image of the resulting fits turned out to be quite flat, with χ^2 values being roughly of order unity in most cases, indicating adequate weighting and fit. The reduced χ^2 of the fits are thus quite close to unity in most cases.

To estimate the errors in our PSF flux measurements, we compared the PSF flux recovered by the fits for the Galactic stars with those from a synthetic aperture photometry with aperture corrections. We found that the former reproduces the latter within $\sim 5\%$. In the fits for the AGN images of our sample, we also measured the residual flux within a $2''$ diameter aperture after the subtraction of the fitted PSF and host components, and found it on average to be less than $\sim 5\%$ of the measured PSF flux. Therefore we assume 5% uncertainty in our PSF flux measurements. This has been found to be typically several times larger than the formal statistical error given by the fit.

The results of the flux measurements are summarized in Table 5.1. The measured fraction of the PSF component within a $2''$ diameter aperture for each object is also tabulated. Similar measurements have been made by Alonso-Herrero et al. (2001) for 5 objects in the list, though only two of them have simultaneous $J/H/K$ observations, for which we have confirmed approximate consistency of the results. Scoville et al. (2000) studied the same NICMOS colors of ultra luminous infrared galaxies (ULIRGs) including a few objects in our sample, by measuring the nuclear fluxes within a $1''.1$ diameter aperture with the adjacent background subtracted. Our two-dimensional de-

Table 5.1.: The list of $z < 0.2$ radio-quiet Type 1 AGN with simultaneous $J/H/K$ or H/K observations in the HST/NICMOS archive. Also given are the physical scale for 0.21 arcsec (FWHM of the PSF in F222M), the measured flux for the central PSF component, and the ratio of PSF-to-total flux within a $2''$ diameter aperture.

object name	z	scale ^a (pc)	obs date	chip/filter	PSF flux (mJy)	PSF/total (in $2''$)
NGC 4151	0.00332	19	1998-05-22	NIC2/F110W	59.9	0.77
				NIC2/F160W	100.	0.82
				NIC2/F222M	197.	0.87
NGC 3227	0.00386	22	1998-04-06	NIC2/F160W	7.84	0.20
				NIC2/F222M	16.6	0.35
NGC 7469	0.0163	67	1997-11-10	NIC2/F110W	17.1	0.64
				NIC2/F160W	38.0	0.68
				NIC2/F222M	79.8	0.80
IC4329A	0.0161	75	1998-05-21	NIC2/F160W	47.5	0.75
				NIC2/F222M	107.	0.85
NGC 5548	0.0172	79	1998-02-15	NIC2/F160W	16.5	0.68
				NIC2/F222M	32.7	0.79
Mrk 231	0.0422	182	1998-09-25	NIC1/F110M	24.9	0.81
				NIC2/F160W	68.6	0.84
				NIC2/F207M	130.	0.88
IRAS07598 ^b	0.148	563	1997-11-11	NIC2/F110W	7.31	0.88
				NIC2/F160W	17.3	0.90
				NIC2/F222M	44.3	0.91
Mrk 1014	0.163	603	1997-12-13	NIC2/F110W	1.27	0.53
				NIC2/F160W	3.01	0.61
				NIC2/F222M	6.93	0.68

^a physical scale of $0''.21$, calculated from the radial velocities corrected with a CMB dipole model from NED.

^b full name: IRAS07598+6508

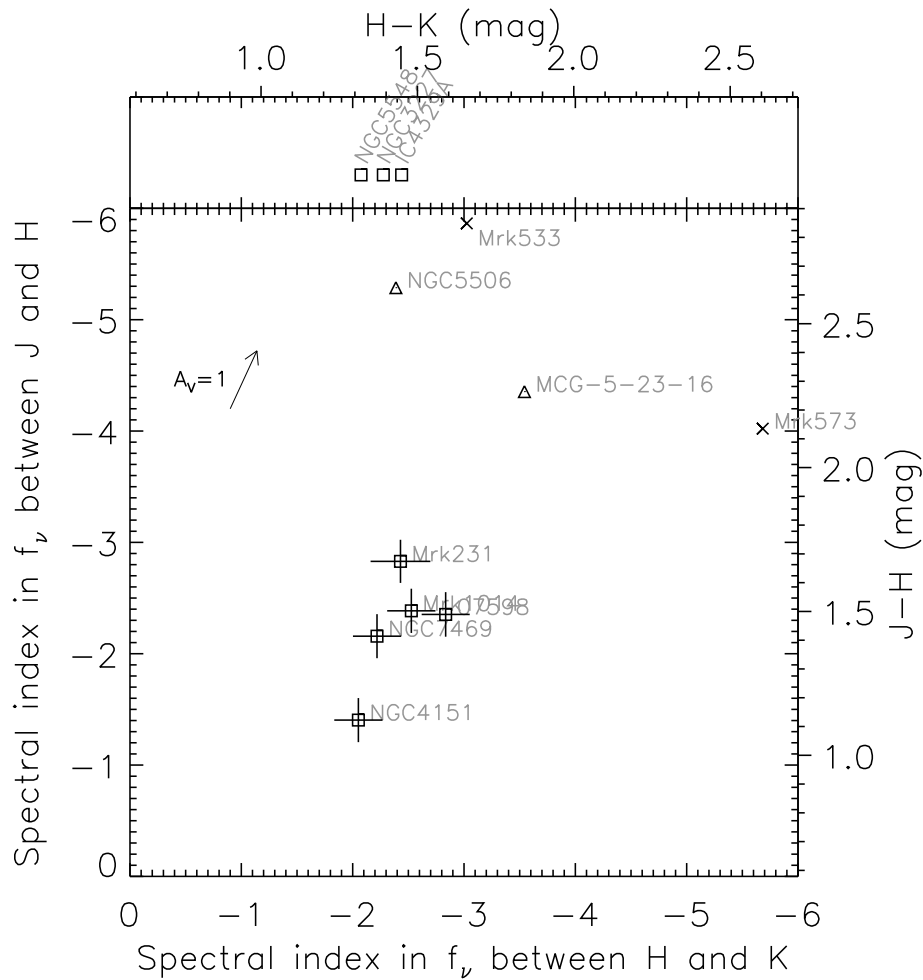


Figure 5.1.: The observed $J - H$ and $H - K$ colors for the nuclear point sources in the HST/NICMOS images of the Type 1 AGN listed in Table 5.1 are shown as squares with error bars. The colors are presented as the spectral index α in f_ν ($\propto \nu^\alpha$) from the fluxes measured with F110W and F160W filters for $J - H$ color, and F160W and F222M filters for $H - K$ color. The corresponding $J - H$ and $H - K$ colors in Vega magnitude are shown as second axes at top and right. In the top small panel, the objects with only a $H - K$ color are shown. The colors of Type 2 (crosses) or intermediate-type objects (triangles) from Alonso-Herrero et al. (2001) have also been plotted for comparison with the Type 1 objects. A foreground reddening vector for $A_V = 1$ is indicated in the upper-left.

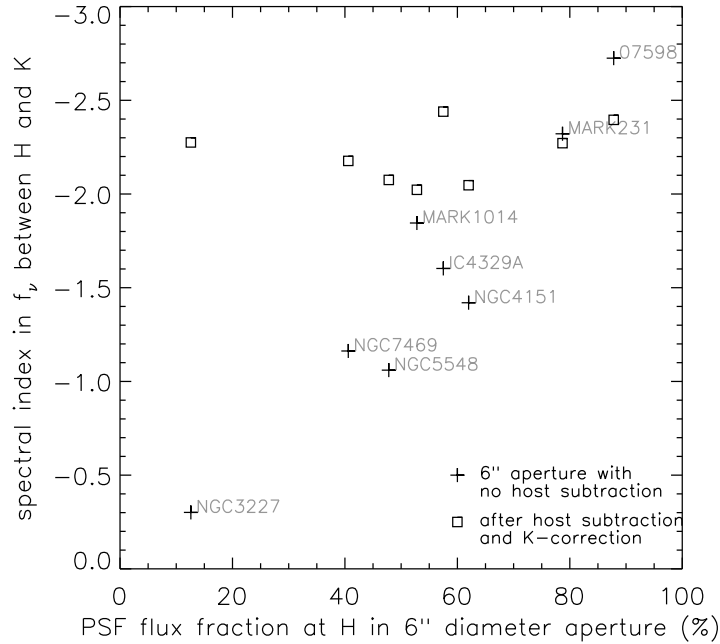


Figure 5.2.: $H-K$ color versus PSF flux fraction in F160W filter image, with synthetic aperture of 6 arcsec diameter (plus signs). Plotted in squares are the $H-K$ colors of the PSF-only flux, i.e. after host galaxy light subtraction (and also after a K-correction; see text).

composition measurements for the common objects are roughly in agreement with their measurements.

The observed $J-H$ and $H-K$ colors for these Type 1 objects are plotted in Fig. 5.1 in squares after a small correction for the Galactic extinction using $E(B-V)$ from NED. The objects with only a $H-K$ color are plotted in the small top panel. For comparison, we have also plotted the same colors of the nuclear point sources in several nearby Type 2 or intermediate-type objects (crosses and triangles, respectively; the latter ones are designated as S1i in the catalog by Véron-Cetty & Véron (2006), meaning that broad lines are detected in the IR). These are at $z < 0.03$ and the fluxes have been deduced by Alonso-Herrero et al. (2001) using both ground-based and HST images. The colors of the Type 1 objects are concentrated in a relatively narrow range, and generally much bluer than those of the Type 2 and intermediate-type objects.

To show the effect of the host subtraction (through the two-dimensional PSF+host decomposition) on the color measurements as compared with large-aperture measurements, we plotted the $H-K$ color versus the PSF flux fraction at H band with a synthetic aperture of 6 arcsec diameter in Fig. 5.2. The color changes significantly as a function of the PSF fraction. For comparison, we also plotted the $H-K$ color of the PSF flux from the PSF+host decomposition (the colors are the same as the $H-K$ colors plotted in Fig. 5.1, i.e. with a K-correction for objects with $J/H/K$ measurements;

see Sect. 5.3 below). As clearly seen, the effect of the host subtraction using these high resolution images is quite significant in the majority of the objects.

5.3. The spectral components of the NIR point sources

5.3.1. Hot dust emission and contribution from the putative accretion disk

Type 1 objects are thought to have low inclination angles, providing a direct view onto the central engine and the broad line region. If we assume that the stellar light from the host galaxy is well subtracted by the PSF+host decomposition, the spectrum of the unresolved source at NIR wavelengths is expected to be composed of essentially two components: (i) the thermal emission from hot dust grains in the innermost torus, nearly at the sublimation temperature; (ii) the central engine emission, i.e. the near-IR tail of the so-called big blue bump emission from the putative accretion disk. We will discuss other possible components below.

If we simply assume the NIR spectrum of dust grains to be that of a blackbody with a single temperature T , and that of an accretion disk to be of a power-law form $f_\nu \propto \nu^{1/3}$ which is a long wavelength limit of standard accretion disks (e.g. Frank et al. 1992), then the spectral shape in the rest frame is fixed for a given T and a given fraction of the accretion disk contribution at a certain wavelength. We parameterize the latter as the disk fraction at the rest wavelength of $2.2\ \mu\text{m}$ and denote it as f_{AD} . These T and f_{AD} can be calculated from the observed set of $J - H$ and $H - K$ colors and redshift z for each object. Equivalently, we can produce a grid of T and f_{AD} on the $J - H$ and $H - K$ color plane for $z = 0$, and plot the $J - H$ and $H - K$ colors of each object with K-corrections assuming this two-component spectrum. Such a color-color diagram is shown in Fig. 5.3 for the Type 1 objects. Note that such K-corrections² for the spectral shape are noticeable essentially only for two objects in the plot. Fig. 5.3 shows that the observed colors follow a relatively well-defined trend: they are along a locus of a roughly similar temperature 1200-1500 K for the hot dust component, with a small range in f_{AD} of 5-25%. The corresponding accretion disk fractions at H and J are much higher, 0.1-0.5 and 0.4-0.9, respectively.

5.3.2. The NIR colors of clumpy torus models

To estimate the extent of the difference of NIR colors from simple black-body spectra, we have simulated the NIR colors of more realistic AGN tori using our clumpy torus model (Hönig et al. 2006, and Sect. 2) which are based on a physically motivated accretion scenario for the formation of a torus (Beckert & Duschl 2004). We concentrate on Type 1 cases where inclinations i are smaller than the half opening angle of the torus and thus our line of sight toward the central engine is free of any model cloud.

²The *K-correction* accounts for the fact that, due to the expansion of spacetime, the photometric standard bandpass in the observer restframe is different from the bandpass in the object restframe. In principle, a certain spectral shape is assumed (here: black body + accretion disk composition) and the wavelength band, λ_{obs} , is “shifted” to the actual wavelength when emitted, $\lambda_e = \lambda_{\text{obs}}/(1+z)$ (simplified for infinitely small bandpass; z = object’s redshift).

We calculated spectra with a dust sublimation temperature T_{sub} of 1200-1500 K and a radial distribution of the number of clouds $\eta_r(r) \propto r^\beta$ where $\beta = -1.1 \dots 2.0$. For each set of model parameters, we calculated 10 random arrangements of cloud placements with a fixed opening angle, or more precisely, a fixed ratio of scale height to radius corresponding to an average half opening angle of $\sim 40^\circ$. More detailed explanations can be found in Chapter 2. We measured colors for the inclination angles free of clouds along the line of sight. These colors are plotted in small gray squares in Fig. 5.3. Overlaid on these gray square points is a small grid of $(T, i) = (1200 - 1500 \text{ K}, 0^\circ - 40^\circ)$ with $\beta = -1.5$, which shows the averaged colors of the 10 random arrangements for each set. The comparison of this single-radial-index grid with the gray square points (which include the indices from -1.1 to -2.0) shows that the radial index generally has a minor effect on colors for this half-opening angle case with Type 1 inclinations. As the inclination increases from 0° to 40° , the colors become slightly bluer since the fractional contribution from the hotter side of the innermost clouds becomes more significant. This trend holds until the inclination becomes close to the half opening angle of the torus, when the colors start to become much redder. For comparison we also have plotted the model colors of Type 2 or intermediate-type inclinations for which one or more clouds are along the line of sight, as small gray crosses. They generally show much redder colors and much larger scatters than those of Type 1 cases.

We have calculated the colors of optically-thin emission from dust grains with various sizes (radii a from 0.001 to $10 \mu\text{m}$) for two temperatures, 1200 and 1500 K, using absorption efficiencies calculated by Draine & Lee (1984) and Laor & Draine (1993). The color tracks for graphite grains are plotted in Fig. 5.3 in gray-blue curves, where colors for $a = 0.01, 0.1, 0.3 \mu\text{m}$ are marked as plus signs. The colors of silicate grains are shown only for $T = 1500 \text{ K}$ and $a = 0.01, 0.1, 0.3, 1, \text{ and } 10 \mu\text{m}$ cases in triangles for clarity, and they are connected with purple dashed lines. As expected, the colors are approaching the blackbody colors of the same temperature as the grain size becomes larger. The curves for graphite grains are truncated at $a = 0.35 \mu\text{m}$, beyond which the colors are almost the same as that of a blackbody.

The spectra of our clumpy tori essentially corresponds to the case of $a = 0.05 \mu\text{m}$ for $\sim 1:1$ mixture of graphite and silicate grains (Hönig et al. 2006). Then the NIR colors of the clumpy tori with a given T_{sub} can be seen as sitting roughly between the blackbody and the optically-thin case (average of graphite and silicate grains with $a = 0.05 \mu\text{m}$) with $T = T_{\text{sub}}$. In more detail, the overall $J - H$ colors of the clumpy tori with a given T_{sub} are roughly the same as the optically-thin color with $T = T_{\text{sub}}$, because the $J - H$ wavelength region is dominated by the emission from the hottest grains. On the other hand, the $H - K$ colors are slightly redder, somewhere between the optically-thin and blackbody case, since it has some contribution from slightly cooler grains at the K -band. Because of this relatively simple behavior, our results can easily be extrapolated toward slightly higher and lower T_{sub} cases, and the results for a particular grain size can also be roughly inferred. If, for example, the grains in the innermost torus region is dominated by those with radii much larger than $0.05 \mu\text{m}$, which we actually argue in the next section, the torus NIR color grid shown in Fig. 5.3 will slightly shift to the red (both in $J - H$ and $H - K$), much closer to the corresponding blackbody colors.

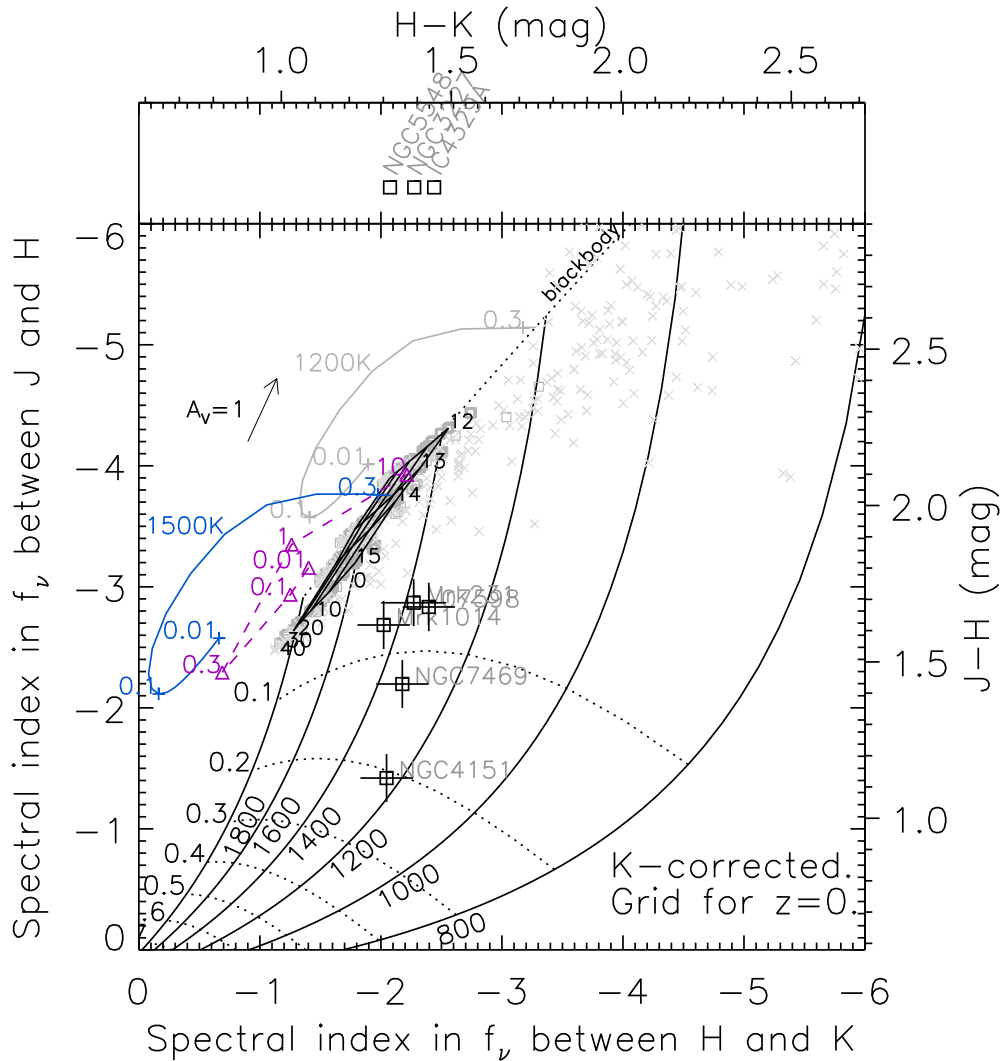


Figure 5.3.: The same $J - H$ and $H - K$ colors for the Type 1 objects in Fig. 5.1 are shown but with a K-correction (see text; no-correction for the objects with only $H - K$ color in the upper panel). A grid for $J - H$ and $H - K$ colors of a blackbody with temperature $T = 800 - 1800$ K, plus a blue power-law component with $f_\nu \propto \nu^{1/3}$ which has a fractional contribution f_{AD} at K -band from 0 with a 0.1 step, has also been plotted. The $J - H$ and $H - K$ spectral indices for each set of (T, f_{AD}) are calculated using the transmission curves of F110W, F160W and F222M filters for the NIC2 camera. The small gray squares concentrated near the blackbody point of $T \sim 1400 - 1800$ K are the colors of our clumpy torus models with Type 1 inclinations, while the small gray crosses which are spread toward much redder colors are for intermediate or Type 2 inclinations. The small flat grid overlaid on the small gray squares, labeled with inclinations ($0 - 40^\circ$) and temperature (12 - 15, in units of 100 K) shows the average colors for Type 1 models. The tracks of colors for optically-thin graphite grains with different sizes are plotted in gray curves for $T = 1200$ (gray) and 1500 K (gray-blue), where the colors for grain radii $a = 0.01, 0.1, 0.3 \mu\text{m}$ are marked as plus signs. The same colors for silicate grains with $T = 1500$ K and $a = 0.01, 0.1, 0.3, 1, \text{ and } 10 \mu\text{m}$ are marked as triangles and connected with purple dashed lines.

In all cases, the overall colors of Type 1 torus models stay quite close to the locus of blackbody colors. Therefore, the above estimate of the fraction of the accretion disk contribution, $f_{\text{AD}} \lesssim 25\%$, essentially stays the same. Furthermore, the observed colors of the HST point sources constrain the plausible range of T_{sub} at least to some extent. The colors appear to disfavor the cases with T_{sub} much higher than ~ 1500 K. This would be true even in the large-grain case described in Sect. 5.4.

5.3.3. The NIR spectral shape of the big blue bump

In the estimation above, we have assumed the NIR spectral shape of the big blue bump (BBB) as $f_{\nu} \propto \nu^{1/3}$. The NIR part of the BBB is still quite unknown, simply because we usually cannot measure it due to the strong dominance of the thermal dust emission from the torus. However, there are a few pieces of observational evidence that the NIR part of the BBB is quite blue, as blue as the long wavelength limit of a non-truncated standard accretion disk, $f_{\nu} \propto \nu^{1/3}$, which is much bluer than the observed optical BBB shape (e.g. $f_{\nu} \propto \nu^{-0.2}$; Neugebauer et al. 1987; Francis et al. 1991). One piece of evidence is from a NIR polarization study of one quasar by Kishimoto et al. (2005). They show that the NIR polarized flux spectrum, which is argued to represent the intrinsic shape of the NIR BBB, is of the form $f_{\nu} \propto \nu^{0.42 \pm 0.29}$. Further evidence comes from the reverberation measurements between the optical and NIR for one nearby Seyfert 1 galaxy by Tomita et al. (2006). They show that the putative disk component has a spectral form of $f_{\nu} \propto \nu^{-0.1 \dots +0.4}$. Of course, these are still far from measuring the spectral shape for the whole population, but pointing towards a color bluer than the observed optical BBB shape. The detailed form of the disk component essentially does not affect our conclusions, as long as it remains relatively blue. The disk component color is the convergence point of the grid in Fig. 5.3 (lower left, outside of the figure), and if the color is bluer than, e.g., the observed optical BBB shape cited above, an estimate for f_{AD} will not change significantly.

5.3.4. Other components

One potential contamination by an additional component in the NIR would be synchrotron emission from radio jets (see also Chapter 4). This is quite unlikely for our sample since we have restricted our objects to radio-quiet objects. On the other hand, it is possible that the NICMOS PSF fluxes have some contribution from a nuclear young stellar cluster on top of the host galaxy profile extrapolated from larger scales. In fact, recent high-spatial-resolution integral field spectroscopic studies (Davies et al. 2007, and references therein) indicate the existence of such young stars with estimated ages of 10-300 Myr in the nuclear vicinity of nearby Seyfert galaxies, including a few objects in our sample (NGC 3227, NGC 7469, Mrk 231). However, its effect on our estimation of f_{AD} is expected to be quite small based on the following reasons: (1) The young stellar cluster luminosity contributes only a few percent on $\sim 10 - 100$ pc scales in most of the Type 1 objects in the Davies et al. (2007) studies; (2) The NIR colors of these young stars are much bluer than the observed colors of the NICMOS point sources studied here — the spectral index for $J - H$ and $H - K$ is $\alpha_{J-H} = -0.5$ and $\alpha_{H-K} = +0.5$, respectively (Scoville et al. 2000, , Fig. 5). Even if these stars are signifi-

cantly reddened by dust, which could be the case for a few luminous infrared galaxies in our sample (Mrk 231, IRAS07598+6508, Mrk 1014), the reddened color ($\alpha_{J-H} = -2.0$, $\alpha_{H-K} = -0.5$; Scoville et al. 2000) is still bluer than the observed point-source colors at least in $H - K$. Therefore, the subtraction of these young stellar component can only make the remaining components redder, which might even decrease the estimation of f_{AD} , but not increase.

A possible foreground reddening of the nuclear point source light can lead to an underestimation of f_{AD} (Fig. 5.3). At least an approximate upper limit on the foreground reddening can be obtained from the broad line ratios. No significant reddening in the ratios ($A_V < 0.5$) has been obtained for NGC4151, NGC5548, NGC7469 (Lacy et al. 1982) and Mrk1014 (Wu et al. 1998). For the rest of the sample, some reddening is present: $A_V \sim 1.5$ for Mrk 231 (Lacy et al. 1982), $A_V \sim 1.4$ for IRAS07598+6508 (Hines & Wills 1995), and $A_V \sim 2 - 4$ for IC4329A (due to an edge-on dust lane, Winkler et al. 1992, and references therein). The estimation of f_{AD} for these objects slightly increases accordingly, but is still consistent with $f_{AD} \lesssim 25\%$.

Therefore, we conclude that, at least for the sample studied here, the fractional contribution from an accretion disk in the K -band is less than $\sim 25\%$. Similar conclusions have been obtained from a detailed analysis of the NIR reverberation data for a Seyfert 1 galaxy (Tomita et al. 2006) and from detailed NIR spectroscopy of quasars (Kobayashi et al. 1993), suggesting the validity of our simple approach.

5.4. The inner boundary of AGN tori

In this section we focus on the expected physical and angular size of the inner torus boundary, which is another critical issue in the high spatial resolution studies of AGN tori. We first summarize the dust sublimation radius in physical and angular size, and compare it with the time-lag radius from the near-IR reverberation measurements in the literature, and then discuss the implications.

5.4.1. Dust sublimation radius

The inner boundary of tori is believed to be set by the sublimation of dust grains. A theoretical calculation of dust sublimation radius r_{sub} by Barvainis (1987) is a well-referenced, quite robust estimation of this inner boundary, which is given as

$$r_{\text{sub}} = 1.3 \text{ pc} \times \left(\frac{L_{\text{UV}}}{10^{46} \text{ erg s}^{-1}} \right)^{1/2} \left(\frac{T_{\text{sub}}}{1500 \text{ K}} \right)^{-2.8} \left(\frac{a}{0.05 \mu\text{m}} \right)^{-1/2} \quad (5.2)$$

(see also Sect. 1.4). In this calculation, Barvainis adopted absorption efficiencies for graphite grains, since they have higher sublimation temperatures T_{sub} than silicate grains and thus are supposed to survive in regions further inwards. The value of $T_{\text{sub}} = 1500 \text{ K}$ is also adopted by Barvainis (1987). For a plausible range of ambient gas pressures, T_{sub} for graphite and silicate grains are estimated to be $\sim 1500 - 1900 \text{ K}$ and $\sim 1000 - 1400 \text{ K}$, respectively (e.g. Salpeter 1977; Huffman 1977; Guhathakurta & Draine 1989; Laor & Draine 1993). We explicitly included the grain radial size a of $0.05 \mu\text{m}$ assumed by Barvainis (1987), which sits in the middle of the inferred

size distribution for interstellar graphite grains (Mathis et al. 1977). The approximate proportionality $r_{\text{sub}} \propto a^{-1/2}$ comes from the absorption efficiency Q_{abs} of a dust grain being roughly proportional to its radius a at a certain wavelength in the NIR (Draine & Lee 1984). L_{UV} is the UV-optical luminosity of the central engine, or more precisely, the integration of the central engine luminosity weighted by Q_{abs} of a dust grain in question.

We can write a corresponding angular radius $\theta_{r_{\text{sub}}}$ in milliarcsecond (mas) as

$$\theta_{r_{\text{sub}}} = 1.2 \text{ mas} \times \left(\frac{L_{\text{UV}}}{6\nu L_{\nu}(V)} \frac{f_{\nu}(V)}{50 \text{ mJy}} \right)^{1/2} \left(\frac{T_{\text{sub}}}{1500 \text{ K}} \right)^{-2.8} \left(\frac{a}{0.05 \mu\text{m}} \right)^{-1/2} \quad (5.3)$$

for $z \ll 1$ cases. Here $f_{\nu}(V) = 50 \text{ mJy}$ approximately corresponds to the V -band flux of the nucleus of the brightest Seyfert 1 galaxy NGC 4151. $L_{\text{UV}}/6\nu L_{\nu}(V)$ is roughly unity for a generic AGN SED (Elvis et al. 1994; Sanders et al. 1989). Note that the angular size is simply proportional to the square root of the observed flux for $z \ll 1$ cases.

5.4.2. The near-IR reverberation radius

The variability in the NIR flux of several nearby Seyfert 1 galaxies has been observed to be delayed with respect to the UV/optical variability (Suganuma et al. 2006, and references therein), and the time lags in these objects have been shown to be consistent with being proportional to $L_{\text{opt}}^{1/2}$ where L_{opt} is the optical luminosity (Suganuma et al. 2006). The light travel distance for the time lag at K -band, R_{τ_K} , has been interpreted to be the distance from the compact UV/optical source to the K -band emitting region, which is thought to be the innermost region of the torus where dust grains are nearly at their sublimation temperature.

The observed proportionality $R_{\tau_K} \propto L_{\text{opt}}^{1/2}$ is in a nice agreement with the proportionality $r_{\text{sub}} \propto L_{\text{UV}}^{1/2}$ for a generic AGN SED. However, the values suggested by the time-lag radii R_{τ_K} and by r_{sub} (with $T_{\text{sub}} = 1500 \text{ K}$ and $a = 0.05 \mu\text{m}$) are actually quite different. Fig. 5.4 compares r_{sub} and the observed R_{τ_K} in physical linear scale as a function of L_{UV} , and Fig. 5.5 in angular scale as a function of optical V -band flux $f_{\nu}(V)$. A fit to the time-lag data points given by Suganuma et al. (2006) can be written as

$$R_{\tau_K} = 0.47 \text{ pc} \times \left(\frac{6 \nu L_{\nu}(V)}{10^{46} \text{ erg s}^{-1}} \right)^{1/2}, \quad (5.4)$$

and the corresponding angular radius for $z \ll 1$ cases is given as

$$\theta_{\tau_K} = 0.43 \text{ mas} \times \left(\frac{f_{\nu}(V)}{50 \text{ mJy}} \right)^{1/2}. \quad (5.5)$$

These fits are plotted in dotted lines in Figs. 5.4 and 5.5. As can be seen clearly, the time-lag radii are systematically *smaller* than r_{sub} by a factor of ~ 3 .

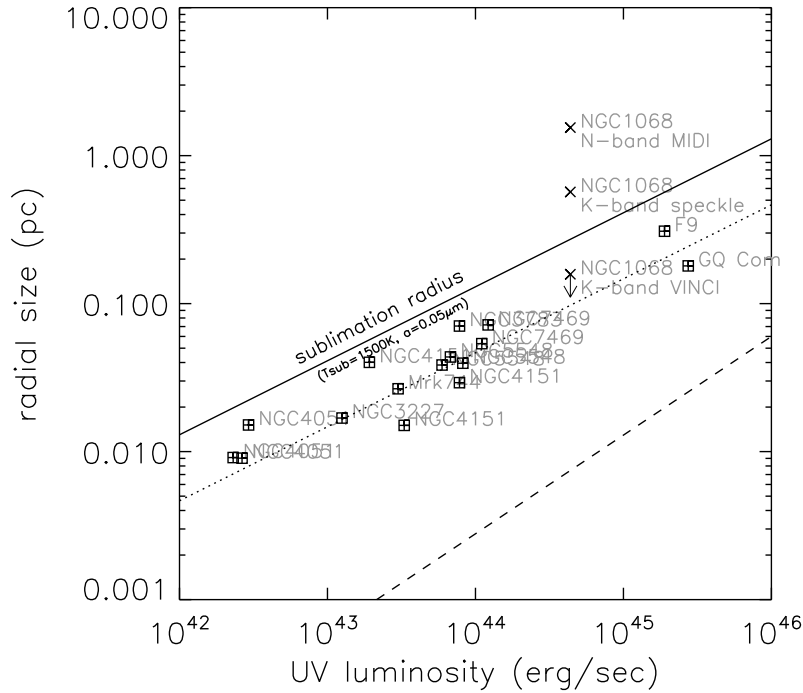


Figure 5.4.: Dust sublimation radius given by Barvainis (1987, ; solid line) for $T_{\text{sub}} = 1500\text{ K}$ and grain size $a = 0.05\ \mu\text{m}$ as a function of UV luminosity L_{UV} , as compared with K -band time-lag radii R_{τ_K} for various Type 1 AGN (Suganuma et al. 2006, and references therein). For the latter, $L_{\text{UV}} = 6\ \nu L_{\nu}(V)$ is assumed, and a fit in $R_{\tau_K} \propto L^{1/2}$ given by Suganuma et al. (2006) is shown as a dotted line. The dashed line is a rough estimation of K -band emitting radii for an untruncated standard accretion disk. Also plotted are the interferometrically measured radial sizes approximately perpendicular to the innermost linear radio structure for NGC 1068 (crosses). The UV luminosity for NGC 1068 here is an unobscured (thus estimated) value.

5.4.3. Implications

The case for the time-lag radius to be the radius of the dominant K -band emitting region, which is thought to be the innermost torus region, seems likely, since the reverberation monitorings show that quite a significant fraction of the K -band emission is varying in response to the UV/optical in many Type 1 objects (e.g. Glass 2004; Minezaki et al 2004; Suganuma et al. 2006). Some minor part of the factor 3 in size might be from a geometrically shortened delay, if the directly illuminated region is only the surface or skin-like region of the inner torus with a relatively small opening angle. However, this would probably not be a dominating factor, as long as the most dominant emission region is still roughly in the equatorial plane of the torus.

Then one implication might be that the sublimation temperature is much higher than 1500 K, and/or the typical grain radius is much larger than $0.05\ \mu\text{m}$. In fact, this has

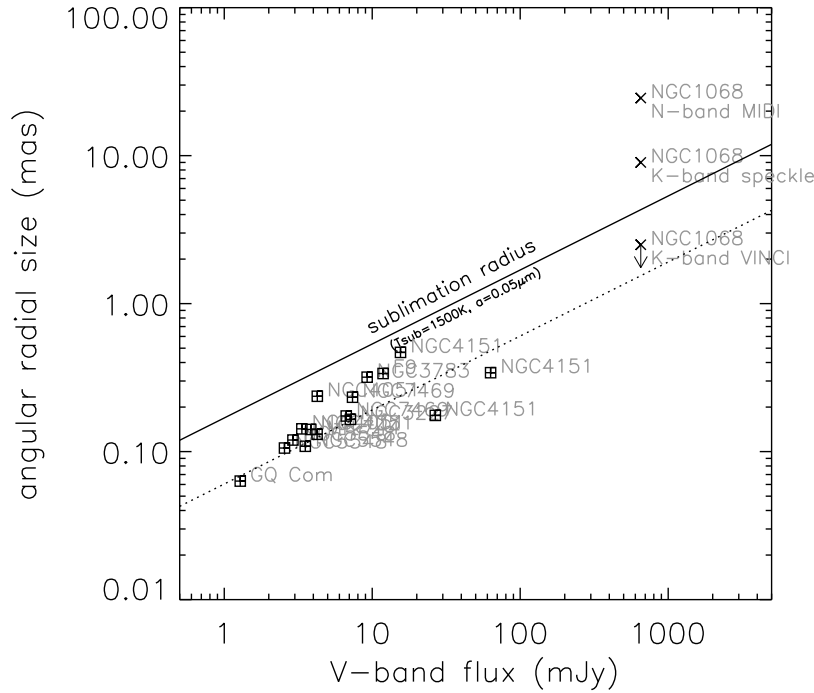


Figure 5.5.: The same comparison as in Fig.5.4 but in angular radius versus V -band flux, with the solid and dotted line corresponding to Eqns. 5.3 and 5.5, respectively (i.e. $z \ll 1$ cases). The V -band flux for NGC 1068 here is an unobscured (thus estimated) value.

been inferred for some individual time-lag cases (e.g. Clavel et al. 1989, Barvainis 1992 for Fairall 9; Sitko et al. 1993 for GQ Com). However, as we noted in Sect. 5.3.2, sublimation temperatures much higher than ~ 1500 K appear to be disfavored by the observed NIR colors of the HST point sources (Fig. 5.3). In this case, the above comparison of r_{sub} and R_{τ_K} might simply suggest the dominance of large grains in the innermost region, and this would systematically be true (at least among these reverberation objects), not just in some individual objects. The sublimation radius as a function of T_{sub} and grain size is well illustrated graphically in Fig. 8 of Laor & Draine (1993). If the sublimation temperature is ~ 1500 K, the typical grain size in radius would be $\sim 0.2 \mu\text{m}$, large enough to be rather close to the blackbody limit. Note that a dominance of large grains in AGN tori has been suggested and discussed on different grounds (e.g. Maiolino et al. 2001a,b; Gaskell et al. 2004).

Another possibility is an intrinsic anisotropy of the central engine radiation, with a factor of ~ 10 reduction from a polar to equatorial direction. This might be consistent with accretion disks where we expect the effects of projected area and limb darkening (e.g. Netzer 1985). Alternatively, there might be a significant extinction, i.e. absorption and/or scattering, of the central engine radiation before reaching the torus. However, its consequences have to be carefully considered. In any case, the

systematic difference between the time-lag radii and r_{sub} indicates that dust properties and/or anisotropy/extinction in the innermost region is somehow similar in these various objects.

5.5. The NIR interferometry of Type 1 nuclei

Small angular sizes of AGN tori require IR interferometric observations to spatially resolve the structure, and some structures actually have been resolved in a few objects with interferometry both in the NIR (Wittkowski et al. 1998, Weinberger et al. 1999, Weigelt et al. 2004, Wittkowski et al. 2004 for NGC 1068; Swain et al. 2003 for NGC 4151) and MIR (Jaffe et al. 2004 for NGC 1068; Tristram 2007 for Circinus). Based on the discussion of the accretion disk flux fraction and the angular size of the inner torus boundary in the previous sections, we discuss some updated expectations for NIR interferometric studies of the innermost region of AGN tori, and also discuss the existing measurements.

5.5.1. Simulated interferometric observations

For the sample studied in Sects. 5.2 and 5.3, the fractional contribution at K -band from a putative accretion disk is suggested to be only $\sim 25\%$ or less, so that the point-source K -band flux is essentially dominated by the flux from the torus. On the other hand, the physical size of the NIR emitting region in the accretion disk is expected to be much smaller than the inner torus boundary. Assuming a simple geometrically-thin optically-thick multi-temperature blackbody disk (Shakura & Sunyaev 1973), we can at least formally estimate the K -band emitting radius $r_{\text{AD},K}$ as a radius where the disk temperature goes down to ~ 1500 K. We obtain

$$r_{\text{AD},K} \simeq 0.06 \text{ pc} \times \left(\frac{\eta}{0.1} \right)^{-1/3} \left(\frac{L}{10^{46} \text{ erg s}^{-1}} \right)^{2/3} \left(\frac{L/L_{\text{Edd}}}{0.1} \right)^{-1/3}, \quad (5.6)$$

where η is the radiative efficiency (the luminosity $L = \eta \dot{M} c^2$; \dot{M} is the mass accretion rate), and L_{Edd} is the Eddington luminosity. This is shown in Fig. 5.4 as a dashed line. The effective size of the K -band emitting region might be even smaller due to the truncation of the outer part of the disk by self-gravity (e.g. Goodman 2003).

Figs. 5.6 and 5.7 show the simulation of interferometric observations for a simple case of a ring-like torus plus a much more compact source, corresponding to an accretion disk, with various fractional flux contributions f_{AD} . Fig. 5.6 is for a ring radius of 1.2 mas corresponding to the angular size in Eqn. 5.3 (r_{sub} case), and Fig. 5.7 is for 0.4 mas in Eqn. 5.5 (R_{τ_K} case). Here, the FWHM w of the ring is set to 1/5 of the ring radius r_{ring} , but the results for the spatial frequency range shown in these Figures essentially do not change as long as $w \ll r_{\text{ring}}$.

The model image (not shown here), or the surface brightness distribution, can apparently be dominated by a point source even for an $f_{\text{AD}} \sim 0.2$ case, simply because of the small emitting size of the accretion disk. However, in the Fourier-transformed image, the low spatial frequency part of the Fourier amplitude profile, or visibility profile, is

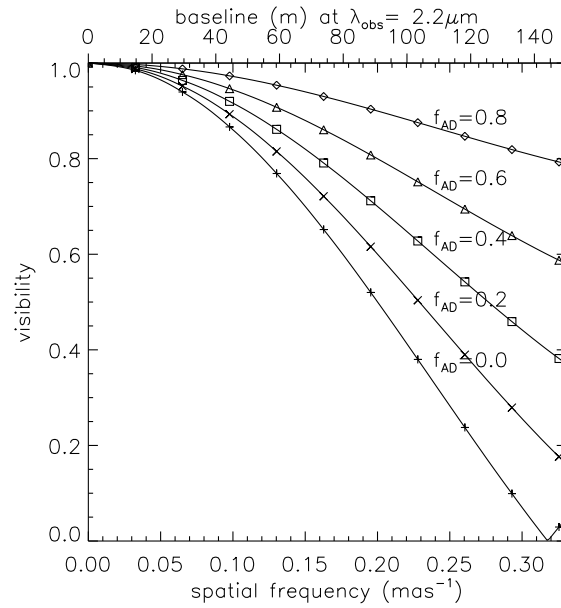


Figure 5.6.: Visibilities, or normalized amplitudes of the Fourier transform, for a model surface brightness image of a 1.2 mas radius ring plus a much more compact source at the center with various flux fractions f_{AD} of the latter. The baselines corresponding to the spatial frequencies in the bottom x -axis are shown in the top x -axis label for an observing wavelength of $2.2 \mu\text{m}$.

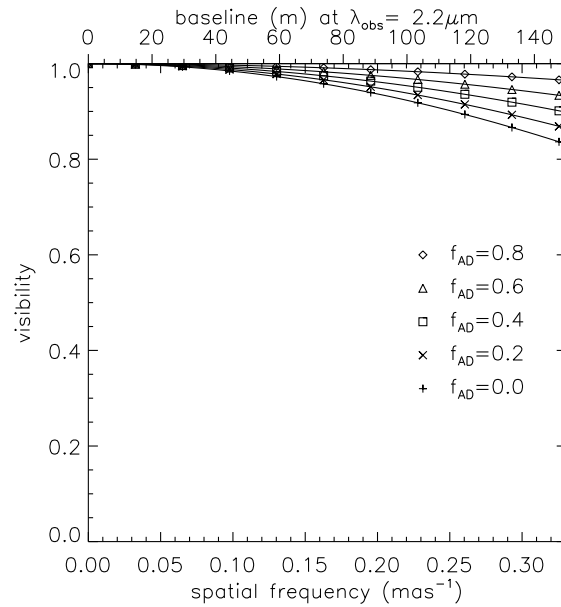


Figure 5.7.: The same as Fig. 5.6 but for a ring radius of 0.4 mas. The same symbols for each f_{AD} are used.

essentially determined by the size of the torus in the cases of low fractional contributions from the disk. Figs. 5.6 and 5.7 show that, when f_{AD} goes down to ~ 0.2 , the profile is already quite similar to the torus-only case (i.e. $f_{\text{AD}}=0$). Simulations with different ring radii show that, if f_{AD} is confined to low values of $\lesssim 0.2$, the dispersion of the visibility curves for a given ring radius caused by this small range of f_{AD} is roughly equivalent to the dispersion due to a ring radius change by $\pm \sim 10\%$ or less. Therefore, if f_{AD} is confined to low values of $\lesssim 0.2$, which seems to be the case at least for the Type 1 objects studied here, the size measurement of the torus in the K -band will not be significantly affected by the accretion disk component.

For both cases with the inner boundary given by r_{sub} (with $T_{\text{sub}} = 1500$ K and $a = 0.05 \mu\text{m}$) and by R_{τ_K} , Figs. 5.6 and 5.7 show that we can measure the size of the innermost region of the torus with a baseline of ~ 100 m at K -band, which is achievable with existing facilities, although we would need at least an accuracy of a few in the visibility measurements for the latter case. Note that the actual visibility for a more realistic torus case would be smaller than the ring case whose radius is equal to the inner boundary radius of the torus, since the intensity distribution would be more extended outwards and not inwards.

5.5.2. Comparison with existing measurements

For the nucleus of the Seyfert 1 galaxy NGC 4151, Swain et al. (2003) measured a squared visibility V^2 of 0.84 ± 0.06 (or $V = 0.92 \pm 0.03$) at a projected baseline of 83 m in K -band with the Keck interferometer. They favored that most of the K -band emission is coming from an unresolved accretion disk, rather than having a ring-like torus emission as the dominant component. One major reason was that, if a ring-like geometry is assumed, the ring radius implied by the measured visibility is ~ 0.5 mas (~ 0.04 pc) which is much smaller than r_{sub} for $T_{\text{sub}} = 1500$ K and $a = 0.05 \mu\text{m}$ (~ 1.2 mas or 0.10 pc for NGC 4151; see Fig. 5.5). However, this implied ring radius is essentially consistent with the time-lag radius which is ~ 0.4 mas for NGC4151. The Keck visibility measurement is consistent with the visibility curves in Fig. 5.7 – note that f_{AD} is estimated to be ~ 0.2 – 0.25 for NGC 4151 (Fig. 5.3). Therefore the interpretation can drastically change if the time-lag radius represents the actual innermost torus radius.

For the nucleus of the Seyfert 2 galaxy NGC 1068, a few interferometric observations have been carried out. In the MIR, a structure has been resolved with VLTI/MIDI (Jaffe et al. 2004) where a Gaussian-modeled³ radial size perpendicular to the innermost radio jet axis is ~ 25 mas (HWHM; ~ 1.6 pc). At K -band, bispectrum speckle interferometry (Wittkowski et al. 1998; Weigelt et al. 2004) has shown that the visibility goes down quite quickly from unity to ~ 0.7 at short baselines (0–6 m), with a measured radial size perpendicular to the jet being ~ 9 mas (Gaussian HWHM; ~ 0.6 pc). Then the visibility has been measured to go down to ~ 0.4 at a long baseline of 46 m at PA 45° with VLTI/VINCI (Wittkowski et al. 2004). When combined together, a multi-component

³Note that an elliptical Gaussian is probably an adequate model for Type 2s rather than a ring, and the visibility curves for a Gaussian and a ring are quite similar at low spatial frequencies before the first visibility minimum (zero) for the latter, if the Gaussian HWHM is equal to the ring radius.

model is favored for the K -band emission where a significant part is coming from spatial scales clearly smaller than ~ 2.5 mas (HWHM; ~ 0.16 pc; see Fig. 1.6).

These measurements are plotted in Figs. 5.4 and 5.5, where the estimation for the intrinsic luminosity is taken from Pier et al. (1994). Although there is inevitable uncertainty in the luminosity estimation, the 2.5 mas upper limit for the compact component from the VINCI measurement appears to fall between r_{sub} (for $T_{\text{sub}} = 1500$ K and $a = 0.05 \mu\text{m}$) and the time-lag radius. The former is ~ 4.3 mas for NGC 1068 (~ 0.27 pc), while the latter is ~ 1.6 mas (~ 0.098 pc). The physical interpretation for the compact component critically depends on the adoption of the correct innermost torus radius R_{in} . It might correspond to, e.g., the clumpiness of the torus if R_{in} is r_{sub} (Wittkowski et al. 2004; Hönig et al. 2006). However, if R_{in} is the time-lag radius, then the small-scale component (< 2.5 mas) might nicely correspond to the inner boundary region, extinguished and partly seen through a clumpy torus.

5.6. Summary and conclusions

The high-spatial-resolution observations of Type 1 AGN tori in the NIR involves a contribution from the NIR part of the big blue bump, i.e., the putative accretion disk emission. We quantified this contribution for the nuclear point sources in the HST/NICMOS images of nearby Type 1 AGN. At least for the available sample, the K -band point-source flux appears to be dominated by a blackbody-like emission from the innermost region of a torus, with only a small contribution from the accretion disk. For the sample studied, the latter fraction is roughly $\sim 25\%$ or less. We also used our clumpy torus model to simulate the NIR torus spectra, and conclude that the estimation for the accretion disk component stays essentially the same.

A theoretical prediction for the inner torus boundary size can be given as a dust sublimation radius. We have shown that the time-lag radius from the NIR reverberation measurements is systematically smaller by a factor of ~ 3 than the predicted sublimation radius with a reasonable assumption for graphite grains of sublimation temperature 1500 K and $0.05 \mu\text{m}$ radius. If the time-lag radius is the correct innermost torus radius, this might indicate a much higher sublimation temperature, though this appears to be disfavored by the observed colors of the HST point sources studied here, or a typical grain size being much larger in the innermost region. Alternatively the central engine radiation might intrinsically be highly anisotropic, or there might be a significant extinction in the equatorial plane between the central engine and torus.

Based on the inferred dominance of the torus emission in K -band and the expected innermost torus radius, we quantified the current expectations for the NIR interferometric observations of Type 1 nuclei. These observations, with a long baseline of ~ 100 m, including the observations of NGC 4151 with different baselines, should provide independent measurements for the innermost torus radius. This will be important for the physical interpretation of the current and future data obtained for AGN tori.

6. Clumpy Dust Tori at Low and High Luminosities

This chapter is based on work published in the paper

Hönig, S. F., & Beckert, T. 2007, MNRAS, 380, 1172

6.1. Overview and context

As discussed in the previous chapters, NGC 1068 seems to host an AGN which is surrounded by a dust torus. Moreover, the combination of infrared interferometric observations and modeling suggests that the structure of the torus is clumpy. A similar conclusion was drawn by Tristram (2007) for the Circinus galaxy. Since the torus is presumably the matter reservoir for fueling the central accretion disk, it is interesting to have a closer look on the actual feedback between AGN and torus. For that, a physical model for clumpy tori has to be studied. Beckert & Duschl (2004) presented a scenario where the torus builds up in the vicinity of the AGN by accretion of matter from galactic scales to the accretion disk. The matter in this torus model is arranged in clouds. They are balanced by self-gravitation and the shear of the gravitational potential of the central supermassive black hole and a possible nuclear star cluster. As the clouds move inwards, their size and optical depth change until they evaporate close to the sublimation radius.

The actual physical properties (e.g., dynamics and dust composition) of the tori are still poorly understood. In particular, the geometrical thickness, which determines the covering factor (obscuration), remains a puzzle: Although axisymmetric, rotating gas and dust configurations with cooling will form thin disks, the torus should keep an aspect ratio $H/r \geq 0.5$ for most of the AGN activity phase. Besides the geometrical thickness, the dynamics of dust in the torus is strongly affected by radiation pressure from the primary AGN emission. It has been suggested that the (radiation) pressure by starformation inside the torus may solve the problem of its geometrical thickness (e.g., Ohsuga & Umemura 1999; Wada & Norman 2002). In a competing scenario, the torus consists of a large number of small, self-gravitating, dusty molecular clouds which form a clumpy torus (Krolik & Begelman 1988; Beckert & Duschl 2004).

In the following study, we describe the feedback of the AGN radiation pressure on a clumpy torus. In Sect. 6.2, we describe the Eddington limit on gas and dust. In Sect. 6.3 and 6.4, we introduce a lower and an upper luminosity limit, respectively, where tori are expected to exist. In Sect. 6.5, some consequences for the appearance of tori at different AGN luminosities are discussed. The results are summarized in Sect. 6.6.

6.2. The Eddington limit for the torus

In the classical picture, the Eddington limit is defined as the state when the gravity of the enclosed mass balances the radiation pressure from the central source, so that

$$L_{\text{edd}} = 4\pi cGM(r) \cdot \frac{m}{\sigma} . \quad (6.1)$$

Here G is the gravity constant, c is the speed of light, and m and σ are the mass and the cross section of the particle which is exposed to the radiation. For a fully ionized plasma around a black hole, the inverse opacity $m/\sigma = \kappa^{-1}$ is dominated by the proton mass and Thomson scattering of electrons. This changes in the region of the torus where dust is mixed with gas. For reference, we use $\kappa_0 = \sigma_T/m_p = 0.4 \text{ cm}^2/\text{g}$ for the fully ionized gas. Assuming that gravity is dominated by the black hole mass $M = M_{\text{BH}} = M_7 \times 10^7 M_\odot$, we obtain the classical Eddington limit

$$L_{\text{edd}}^{(\text{std})} = 1.26 \times 10^{45} \text{ erg s}^{-1} \cdot M_7 . \quad (6.2)$$

The time-averaged AGN luminosity is expected to scale with the mass accretion rate in the accretion disk by $L = \eta \dot{M}_{\text{AD}} c^2$. In a stationary scenario, the accretion disk itself is fueled by mass transported through the torus from galactic scales. The mass transport rate through the torus \dot{M}_{Torus} is related to \dot{M}_{AD} via $\dot{M}_{\text{AD}} = \dot{M}_{\text{Torus}} - \dot{M}_{\text{outflow}}$. This relation considers mass loss in an outflow or jet during the accretion process from the torus towards the inner accretion disk. With $\tau = 1 - \dot{M}_{\text{outflow}}/\dot{M}_{\text{Torus}}$, we obtain

$$L = \eta\tau \dot{M}_{\text{Torus}} c^2 . \quad (6.3)$$

The combination of theory and observation for radiative efficient accretion with outflows suggests $0.01 \lesssim \eta \lesssim 0.1$ and $0.1 \lesssim \tau \lesssim 1$ (e.g., Emmering et al. 1992; Pelletier & Pudritz 1992). In the following we will use a representative value of $\eta\tau = 0.05$. From Eqn. (6.3), we obtain $\dot{M}_{\text{Torus}} = 0.4 M_\odot \text{ yr}^{-1} \times L_{45}$. Here, L_{45} is the bolometric luminosity of the accretion disk in units of $10^{45} \text{ erg s}^{-1}$, with peak emission at UV/optical wavelengths.

We will now investigate the accretion properties for a dusty medium in the AGN torus considering a smooth dust distribution and a clumpy structure, respectively.

6.2.1. Smooth dust distribution

Radiative transfer simulations of AGN dust tori frequently use dust which is smoothly distributed (e.g., Pier & Krolik 1992; Granato & Danese 1994; Schartmann et al. 2005). The radiation which comes from the central AGN directly acts on the dust grains in the torus. The absorption cross section of the dust grains in the optical and UV regime can be approximated by their geometrical cross section $\sigma = \pi r_{\text{Dust}}^2$. Standard size distributions assume dust grain sizes between $0.025 \mu\text{m}$ and $0.25 \mu\text{m}$ (e.g., Mathis et al. 1977). Using a typical dust grain density of $2 - 3 \text{ g/cm}^3$, we obtain an opacity $\kappa_{\text{Dust}} \sim 3 - 40 \times 10^4 \kappa_0$. Using κ_{Dust} in Eqn. (6.1), the Eddington luminosity for smoothly distributed dust becomes

$$L_{\text{edd}}^{(\text{smooth})} = 0.3 - 5 \times 10^{40} \text{ erg s}^{-1} \cdot M_7 \quad (6.4)$$

Due to the large value of κ , the Eddington luminosity decreases by 5 orders of magnitude. As a consequence, typical AGN luminosities of 10^{45} erg s $^{-1}$ would require a black hole mass of $10^{12} M_{\odot}$. This is, however, inconsistent with observed $M_{\text{BH}}/L_{\text{bol}}$ -ratios (e.g., Kaspi et al. 2000; Woo & Urry 2002). As a consequence the dust can not be gravitationally bound to the black hole.

The result with the approximated κ_{Dust} is consistent with recent opacity calculations for a more realistic dust and gas mixture (e.g., Semenov et al. 2003). They show that dust opacities for UV temperatures, which are dominating the AGN accretion disk radiation, are about 4 orders of magnitude larger than the Thomson opacity κ_0 . In principle, IR photons coming from more external regions of the torus act as a counter force to the the UV photon pressure from the AD. However, the IR opacity of the gas and dust mixture is $\sim 10^3$ times smaller than the UV opacity, resulting in an insignificant effect of IR photons when compared to the dominating UV photons. Furthermore, the geometry of the torus causes the diffuse IR torus radiation to act more or less isotropically on the inner wall of the torus (at least in the torus plane), so that a possible IR counter pressure is even weakened. To the contrary, it is rather expected that the main effect of the IR photon pressure inside the torus is a vertical thickening (Krolik 2007).

Eqn. (6.4) considers dust grains which are decoupled from the gas. However, even for a perfect coupling of gas and dust in the torus (no drift of the dust relative to the gas), the usually assumed mass ratio of gas to dust of 100 raises the limit $L_{\text{edd}}^{(\text{smooth})}$ to only 0.001 of the classical limit in Eqn. (6.2). The limit $L_{\text{edd}}^{(\text{smooth})}$ is valid for an optically thin gas dust mixture, while AGN tori are necessarily optically thick, providing self-shielding of most of the torus against the AGN radiation. This creates a radiation pressure gradient at the inner boundary layer (width $\tau_{\text{UV}} \sim 1$) of the torus. The corresponding outward force on this layer is $L/L_{\text{edd}}^{(\text{smooth})} \sim L_{\text{edd}}^{(\text{std})}/L_{\text{edd}}^{(\text{smooth})} \sim 10^3$ times stronger than the gravitational pull of the central black hole. This outward force would have to be counterbalanced by an enormous inward pressure gradient in the inner boundary layer.

6.2.2. Clumpy dust torus

An alternative model to smoothly distributed dust was proposed by Krolik & Begelman (1988). They argue that most of the gas and dust in the torus around an AGN has to be arranged in optically thick, self-gravitating clouds. Vollmer et al. (2004) and Beckert & Duschl (2004) presented a stationary accretion model for the clumpy torus (hereafter: SA model), including relations for torus and dust cloud properties. The main idea behind this model is that clouds are very compact with a large optical depth in the UV due to dust which provides self-shielding against the AGN radiation and allows the cloud's interior to be cold. Dust grains on the directly illuminated sides of the clouds are exposed to the AGN and individual dust grains are potentially accelerated and expelled from the cloud due to the radiation pressure. Both magnetic fields and dynamical friction of grains in the gas phase of the cloud (e.g., see Spitzer 1978, Sect. 9) can prevent this and transfer the momentum to the gas. In a self-gravitating cloud the radiation pressure is therefore received by the whole cloud. Thus, the torus is limited

by the radiation pressure from the central AGN acting on the dust clouds instead of single grains, so that we can define a cloud opacity $\kappa_{\text{cl}} = \pi R_{\text{cl}}^2 / M_{\text{cl}}$.

The SA model assumes the clouds to be self-gravitating, so that the free-fall time equals the sound crossing time R_{cl}/c_s . This provides a linear relation between cloud mass M_{cl} and R_{cl} . These clouds should be stable against tidal forces in the gravitational field of the central black hole. This requires $R_{\text{cl}}^3/r^3 \leq 2M_{\text{BH}}/M_{\text{cl}}$. When combining both limits (see Beckert & Duschl 2004), one finds an upper limit for the cloud size

$$R_{\text{cl,max}} = \frac{\pi}{\sqrt{8G}} \cdot \frac{c_s r^{3/2}}{M^{1/2}} \quad (6.5)$$

and a corresponding mass

$$M_{\text{cl}} = \frac{\pi^2 c_s^2}{8G} R_{\text{cl}}. \quad (6.6)$$

Here c_s is the cloud-internal speed of pressure waves which is of the order of 1 km s^{-1} . We use this value as the unit for c_s in the following. This speed characterizes the cloud internal pressure which is required to balance self-gravity, and can be understood as the speed of supersonic turbulence in the clouds. Alternatively, the clouds may be magnetically supported¹. Due to their large cross section, large clouds at the shear limit dominate the absorption, scattering, and IR re-emission. From the relations for R_{cl} and M_{cl} , we get an upper envelope for the opacity of $\kappa_{\text{cl}} = 0.7\kappa_0 \cdot r_{\text{pc}}^{3/2} / (c_s M_7^{1/2})$. The distance from the black hole r_{pc} is measured in pc and the speed c_s in km s^{-1} . For clouds smaller than the shear limit, the opacity $\kappa_{\text{cl}} \propto R_{\text{cl}}$ becomes smaller. With Eqn. (6.1), we obtain the Eddington limit for clouds in a clumpy torus, which are directly exposed to the primary AGN radiation,

$$L_{\text{edd}}^{(\text{cl})} = 1.78 \times 10^{45} \text{ erg s}^{-1} \cdot \frac{c_s M_7^{3/2}}{r_{\text{pc}}^{3/2}}. \quad (6.7)$$

This is of the same order as in the classical Eddington limit (Eqn. 6.2) and is consistent with observed AGN luminosities and black hole masses. Since $L_{\text{edd}} \propto \kappa^{-1}$, the Eddington limit for small clouds is even larger than in Eqn. (6.7).

Eqn. (6.7) shows that $L_{\text{edd}}^{(\text{cl})} \propto r^{-3/2}$. This implies that at larger distances, self-gravitating clouds which are directly exposed to the AGN radiation become unbound by the radiation pressure. Thus, distant clouds have to be shielded against the AGN radiation by clouds at small radii. As a consequence, there should be no significant vertical flaring for a clumpy torus; i.e., we expect $H/r \approx \text{const}$. Further consequences of this behavior will be discussed in Sect. 6.4.

¹The mass density of clouds from Eqn. (6.5) and (6.6) is $\rho = 1.6 \times 10^{-16} \text{ g cm}^{-3} M_7 r_{\text{pc}}^{-3}$. A dynamically relevant B -field will have to have a strength of a few mG. This leads to gyration times of grains shorter than the dynamical time of the clouds $R_{\text{cl,max}}/c_s$. The large densities $n_H \sim 8 \times 10^7 \text{ cm}^{-3} M_7 r_{\text{pc}}^{-3}$ are sufficient to effectively transfer momentum from grains to the gas and to limit the drift velocity of grains to about c_s . Both mechanisms support the above claim that radiation pressure acts on the whole cloud.

6.3. The torus at low AGN luminosities

In the previous section, we argued that the Eddington limit for clumpy dust tori is well in agreement with the range of observed AGN luminosities and black hole masses. To be clumpy, a torus requires a small volume filling factor $\Phi_V \ll 1$ for the dusty clouds. In the context of the SA model, Beckert & Duschl (2004) find a mass transport rate through the torus $\dot{M}_{\text{Torus}} = 3\pi\nu\Sigma$, where $\nu = \frac{\tau}{1+\tau^2}H^2\Omega_{\text{Kepler}}$ is the effective viscosity for a torus, Σ is the surface density, and Ω_{Kepler} is the Keplerian velocity. For an obscuring torus, the scale height, H , cannot be smaller than the mean free path of clouds $H \geq l = (4/3)R_{\text{cl}}/\Phi_V$. Otherwise the torus would become transparent for AGN photons. The parameter τ in the viscosity prescription measures the ratio $\tau = l/H$. The geometric thickness of the torus and the viscosity is maximized for $\tau = 1$. For $H \gg l$ the cloud density in the torus grows rapidly and the torus would collapse to a thin disk. We therefore adopt $H = l$ for a working model. After replacing the mean free path by the appropriate expression from Beckert & Duschl (2004), we get Φ_V in terms of \dot{M}_{Torus} ,

$$\Phi_V = \frac{\pi^{7/4}}{\sqrt{6G}} \cdot \frac{c_s^{3/2}}{\dot{M}_{\text{Torus}}^{1/2}}. \quad (6.8)$$

The volume filling factor only depends on the mass transport rate through the torus, which we parameterized by $\dot{M}_{\text{Torus}} = 0.4 M_{\odot} \text{ yr}^{-1} \times L_{45} \cdot (\eta\tau/0.05)^{-1}$ (see Sect. 6.2). By substituting \dot{M}_{Torus} , we obtain a hard lower luminosity for the existence of an obscuring torus according to the SA model,

$$L_{\text{low}} = 5 \times 10^{42} \text{ erg s}^{-1} \cdot \left[\frac{\eta\tau}{0.05} \right] \quad (6.9)$$

at which $\Phi_V = 1$. For clumpy obscuring tori as described here, it is necessary that the AGN luminosity is $L \gg L_{\text{low}}$. If $L \gtrsim L_{\text{low}}$, the volume filling factor becomes $\Phi_V \rightarrow 1$. At this point, the SA model would require that the torus collapses to a geometrically thin disk. As a consequence, most of the dust would be driven away (see Sect. 6.2.1). It is, however, known that this situation can be avoided: Lower luminosities go along with lower accretion rates. Vollmer et al. (2004) showed that for low mass accretion rate, a clumpy and almost transparent ($l \gg H$) circumnuclear disk (CND) can form, similar to what has been found around the central black hole in our Galaxy (Güsten et al. 1987). The difference between the clumpy torus and the CND is that the latter one loses most of its obscuration properties while there can still be IR re-processing.

Several observational studies show that at about $10^{42} \text{ erg s}^{-1}$, the $L_{\text{bol}} - L_{\text{MIR}}$ - or $L_X - L_{\text{MIR}}$ -relation show a significant change in behavior compared to higher luminosities (e.g., Lutz et al. 2004; Horst et al. 2006). Apparently, the main source of MIR emission at $L \sim 10^{42} \text{ erg s}^{-1}$ is not the proposed, geometrically thick torus anymore. A similar low-luminosity limit has been found for models where the dust clouds are not produced in a torus but released into a wind from an accretion disk (Elitzur & Shlosman 2006). The cutoff at lower luminosities is a result of the fact that the mass outflow rate in the wind cannot exceed the mass accretion rate in the disk. Taking the same τ and η as used in Elitzur & Shlosman (2006), we obtain $L_{\text{low}} = 2 \times 10^{42} \text{ erg s}^{-1}$.

6.4. The dust torus in the high luminosity regime

In Sect. 6.2.2, we have shown that the Eddington luminosity for clouds in the clumpy torus, $L_{\text{edd}}^{(\text{cl})}$, depends on the cloud-AGN distance as $r^{-3/2}$. A large fraction of AGN radiate close to or at the classical Eddington limit for Thomson scattering (McLure & Dunlop 2001). We therefore scale the actual luminosity to the classical limit $L = L_{\text{edd}}^{(\text{std})} \ell_{\text{Edd}}$, where $\ell_{\text{Edd}} \leq 1$ is the Eddington ratio for the AGN. Once $L_{\text{edd}}^{(\text{cl})}$ becomes smaller than L , the clouds of corresponding $R_{\text{cl}}(r)$ which are directly exposed to the radiation of the central source can no longer resist the radiation pressure. This defines the condition $L/L_{\text{edd}}^{(\text{cl})} < 1$ for the existence of dust clouds of radius $R_{\text{cl}}(r)$ in the AGN radiation field. Since $L_{\text{edd}}^{(\text{cl})}$ is r -dependent, we obtain a maximum distance from the AGN, $r_{\text{max}}(R_{\text{cl}})$, at which the largest clouds can withstand the radiation pressure:

$$r_{\text{max}}(R_{\text{cl}}) = 1.3 \text{ pc} \cdot \ell_{\text{Edd}}^{-2/3} c_s^{2/3} M_7^{1/3} \cdot \left(\frac{R_{\text{cl}}}{R_{\text{cl,max}}} \right)^{-2/3}. \quad (6.10)$$

The factor $(R_{\text{cl}}/R_{\text{cl,max}}) \leq 1$ accounts for different cloud radii R_{cl} up to the shear limit $R_{\text{cl,max}}$ (see Eqn. (6.5)). As mentioned in Sect. 6.2.2, clouds at distances $r > r_{\text{max}}$ need to be shielded, so that no vertical flaring should occur beyond r_{max} . We want to note that r_{max} does *not* refer to an outer radius of the torus. It relates the maximum possible size of a dust cloud to the radiation pressure from the central AGN.

A proper scaling of the limiting radius, r_{max} , is in units of the dust sublimation radius which presumably sets the inner radius of the torus. The sublimation radius is depending on the actual dust chemistry and grain sizes. A well-referenced estimation of r_{sub} was introduced by Barvainis (1987), providing $r_{\text{sub}} = 0.4 \text{ pc} \times L_{45}^{1/2} T_{\text{sub};1500}^{-2.8} a_{0.05}^{-1/2}$, where sublimation of graphite grains of radius $0.05 \mu\text{m}$ and a sublimation temperature of 1500 K is assumed. For different grain sizes and chemistry, the sublimation temperature and the temperature exponent change. Thus, in the case of silicate grains with similar grain size, the sublimation radius is larger by about a factor of about 3. While the actual chemistry, grain sizes and sublimation temperatures around AGN are still a matter of debate (e.g., Barvainis 1992; Sitko et al. 1993; Kishimoto et al. 2007, see Chapter 5), reverberation measurements of type 1 AGN support $r_{\text{sub}} \propto L^{1/2}$ (Suganuma et al. 2006). In the following, we will use the simplified relation $r_{\text{sub}} = 0.5 \text{ pc} \times L_{45}^{1/2}$, keeping in mind the uncertainty due to the actual dust mixture.

Finally, this allows for a comparison of r_{max} with the inner boundary of the torus:

$$\frac{r_{\text{max}}}{r_{\text{sub}}} = 2.3 \cdot c_s^{2/3} L_{45}^{-1/6} \cdot \ell_{\text{Edd}}^{-1} \left(\frac{R_{\text{cl}}}{R_{\text{cl,max}}} \right)^{-2/3}. \quad (6.11)$$

Interestingly, $r_{\text{max}}/r_{\text{sub}}$ is approximately of the order of unity. That means that at $L \gtrsim L_{45}$, the maximum dust cloud size can be limited by the radiation pressure rather than the shear limit. Which mechanism dominates for an individual AGN depends on its actual L/M . We will, thus, distinguish between radiation-limited tori (AGN with higher ℓ or L) and shear-limited tori (AGN with lower ℓ or L) in the following.

An effect of Eqn. (6.11) is a change in obscuration properties with higher luminosities. In Sect. 6.3, we briefly summarized the results from the SA model which requires

$H = l = 4/3 R_{\text{cl}}/\Phi_{\text{V}}$. Contrary to the situation at lower AGN luminosities, R_{cl} is now defined by the radiation limit (Eqn. (6.11)) instead of the shear limit (Eqn. (6.5)). From $R_{\text{cl}} \propto L^{-1/4}$ (Eqn. (6.11)) and $\Phi_{\text{V}} \propto \dot{M}_{\text{Torus}}^{-1/2} \propto L^{-1/2}$ (Eqn. (6.3)), we obtain $H \propto L^{1/4}$. Since the torus is expected to have $H/R = \text{const}$, the thickness of the torus is determined at the reference distance $R = r_{\text{sub}} \propto L^{1/2}$. This results in an average thickness of the torus,

$$H/R \propto L^{-1/4}. \quad (6.12)$$

Thus, we expect to see more type 1 AGN at higher luminosities for objects which have radiation-limited clumpy tori.

This result can be interpreted in the framework of the “receding torus” (Lawrence 1991): It has been observed that for high-luminosity sources, the observed hydrogen column density is lower than in low-luminosity sources (e.g., Ueda et al. 2003; Barger et al. 2005; La Franca et al. 2005; Akylas et al. 2006). This is interpreted as a decrease of the covering factor of the torus with luminosity; i.e., H/R appears to be anti-correlated with L . Recently, Simpson (2005) analyzed the luminosity-dependence of the type 1 and type 2 AGN fraction by combining the results from different surveys. While the original receding torus (Lawrence 1991) predicts a type-2-fraction $f_2 \propto L^{-1/2}$, a better fit was found for a situation where the height of the torus depends on luminosity. From Eqn. (6.12), we would approximately expect $f_2 \propto L^{-0.25}$ for radiation-limited dust tori. This is remarkably close to the correlation $f_2 \propto L^{-0.27}$ derived by Simpson. We note, however, that for objects with low ℓ_{Edd} , the $L^{-1/4}$ -dependence should not hold but can even be inverted (see Eqn. 6.5). This would imply that it depends on the actual AGN sample properties if a receding torus is observed or not.

For flux-limited AGN samples where only the brighter objects with higher Eddington ratios are observed, we expect that the type 2 fraction follows approximately the $L^{-1/4}$ relation. To be more quantitative, the type 2 fraction, f_2 , can be derived by determining the solid angle around the AGN which is covered by the dust torus. As simulations with our clumpy torus model have shown, the transition angle, θ_0 , between viewing a type 1 and a type 2 AGN can be approximated by $\tan \theta_0 = H/R$. Thus, the solid angle Ω_{Torus} occupied by the torus is

$$\Omega_{\text{Torus}} = 2\pi \int_{-\theta_0}^{\theta_0} \cos \theta \, d\theta = 4\pi \sin \theta_0 \quad (6.13)$$

where θ is measured from the torus plane. The torus covering fraction (or type 2 fraction) becomes $f_2 = \Omega_{\text{Torus}}/(4\pi) = \sin \theta_0$. Using the trigonometric conversion $\sin(\arctan x) = x/(\sqrt{1+x^2})$ finally leads to the expression for f_2

$$f_2 = \frac{H/R}{\sqrt{1+(H/R)^2}} \quad (6.14)$$

After inserting the L -dependent relation of H/R , we obtain

$$f_2 \approx \frac{0.6 \times L_{45}^{-1/4}}{\sqrt{1 + 0.36 \times L_{45}^{-1/2}}} \quad (6.15)$$

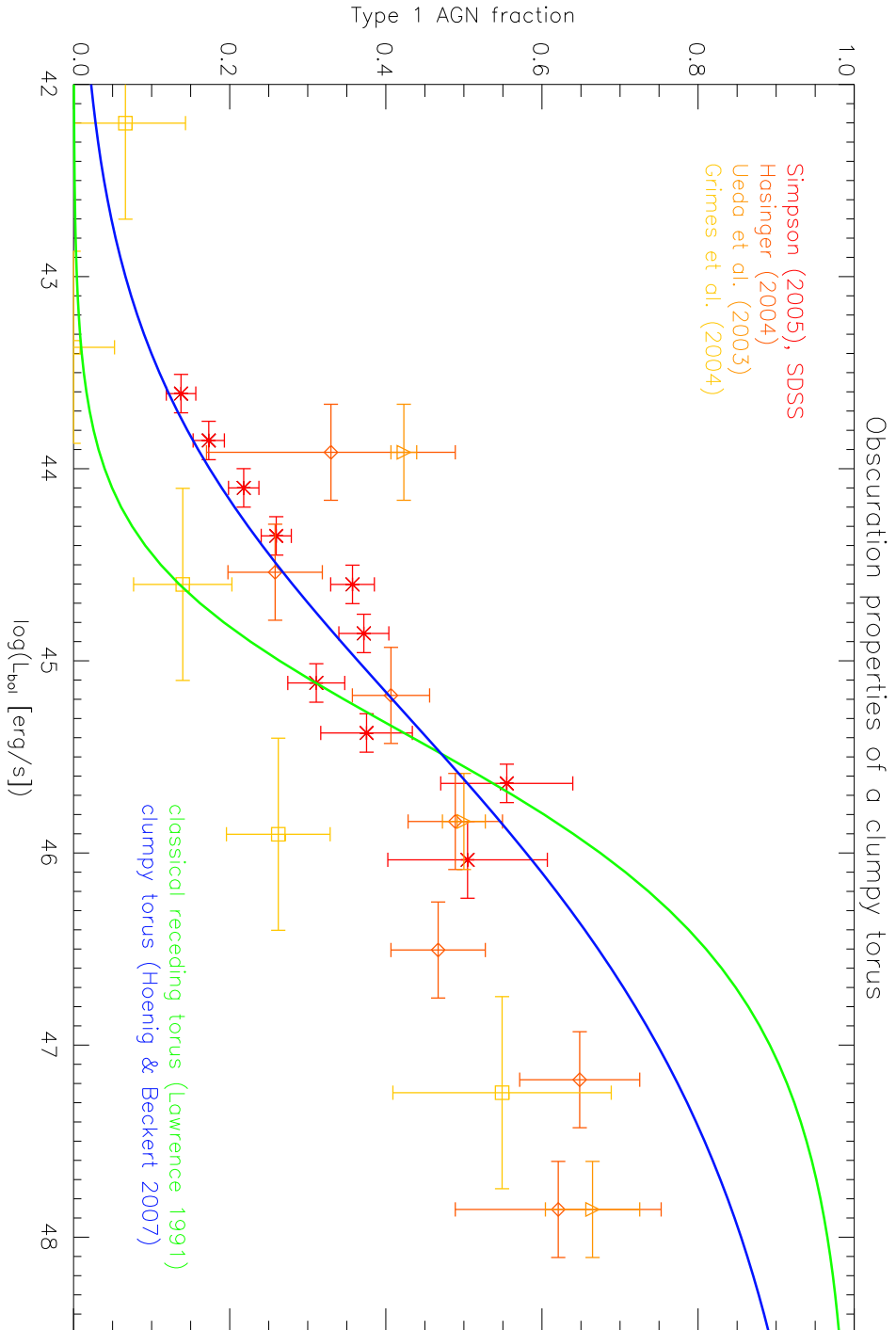


Figure 6.1: Comparison between the type 1 fractions as extracted from various kinds of AGN surveys (Simpson 2005), and the expectations from the original receding torus (green; Lawrence 1991) and our model (blue).

For typical AGN luminosities of $L \gtrsim 10^{44} \text{ erg s}^{-1}$, the denominator of Eqn. (6.15) is ~ 1 , so that the dominating dependence is $L^{-1/4}$ for the radiation limited tori. In Fig. 6.1, we show a compilation of type 1 fractions versus luminosity as derived from several surveys (Ueda et al. 2003; Grimes et al. 2004; Hasinger et al. 2004; Simpson 2005). The type 1 fraction, f_1 , is defined as $f_1 = 1 - f_2$. The luminosities have been converted to bolometric luminosities by using the $L_X - L_{\text{bol}}$ -relation as presented by Marconi et al. (2004). Overplotted are expectations for the classical receding torus picture (Lawrence 1991) and our model according to Eqn. (6.15). While the classical receding torus shows higher residuals, the derived $L^{-1/4}$ seems to be better in agreement with observations. The remaining discrepancy can be explained by considering that only a fraction of the observed high-luminosity AGN actually contain radiation-limited tori. The deeper a survey goes, the more shear-limited objects with low Eddington ratios will show up. As a result, the distribution flattens and might even inverse its slope.

6.5. Mismatch between AGN type and X-ray obscuration

Several authors noted that the UV-to-IR dust extinction in AGN is lower than what would be inferred from the X-ray column density, in particular referring to AGN showing broad-lines in the optical and significant absorption in the X-rays (e.g., Wilkes et al. 2002; Perola et al. 2004; Barger et al. 2005). In the clumpy torus model, the AGN's X-ray emission region is completely obscured by an average number, N , of optically thick clouds along a line of sight passing through the torus. Since the size of the X-ray source is smaller than the typical cloud radius, $R_X < R_{\text{cl}}$, the X-ray column density is $n_X \sim N \cdot n_{\text{cl}}$, where n_{cl} denotes the column density of an individual cloud. On the other hand, the broad-line region (BLR) is only fractionally (and statistically) obscured by a number of N optically thick clouds, since $R_{\text{BLR}} > R_{\text{cl}}$. As a result, the average optical depth in the optical wavelength range, τ_V , can be approximated by $\tau_V \sim N$ (Natta & Panagia 1984). Thus, the inferred optical depth from the X-rays, $N \cdot \tau_{\text{cl}}$, overestimates the measured optical depth $\tau_V \approx N$ for a more extended emission region like the BLR. Here, $\tau_{\text{cl}} \gg 1$ is the optical depth of an individual dust cloud. Furthermore, if N is sufficiently small, there exists a high probability that parts of the BLR are directly visible to the observer, while the X-ray source is still obscured ($R_{\text{BLR}} > R_{\text{cl}} > R_X$). This effect should become stronger at higher AGN luminosities when the clumpy tori become radiation-dominated, since $N \propto l^{-1} \propto L^{-1/4}$. Actually, Perola et al. (2004) report that $\sim 10\%$ of their observed broad-line AGN show high column densities, all of them having X-ray luminosities $L_{2-10 \text{ keV}} > 10^{44} \text{ erg s}^{-1}$.

6.6. Summary and Conclusions

We studied the effect of dust on the Eddington limit in the molecular dusty torus of an AGN. While the Eddington limit for smooth dust distributions is approximately 5 orders of magnitudes smaller than the classical Eddington limit for a fully ionized plasma, a clumpy dust torus provides a similar $L_{\text{edd}} - M_{\text{BH}}$ -relation as the classical one, and is in good agreement with observed luminosities and black hole masses. The idea of a clumpy torus is based on self-gravitating, optically thick dust clouds which are limited in size

by the shear of the gravitational potential of the central black hole. In the framework of this model, we were able to derive a low-luminosity limit for the existence of an obscuring clumpy torus, which is of the order of $L \sim 10^{42} \text{ erg s}^{-1}$. Below this limit, the physical and geometrical properties of the torus change significantly. Furthermore, we investigated the behavior of the clumpy torus at high luminosities. We found that the largest clouds in the torus become gravitationally unbound to the central black hole if the AGN radiates close to the classical Eddington limit. In such a case, the dust clouds in the torus are no longer limited in size by the shear of the gravitational potential but by the AGN luminosity. The effective scale height of the radiation-limited tori decreases with luminosity, $H/R \propto L^{-1/4}$. The resulting L -dependence for the fraction of type 2 AGN, $f_2 \propto L^{-0.25}$ is consistent with an analysis of several AGN surveys by Simpson (2005). We showed that the clumpy torus can account for broad-line AGN with high X-ray column densities, and that more such objects should be found at high rather than at low luminosities.

7. Dust Tori in Obscured QSOs

This chapter is based on work published in the paper

Polletta, M., Weedman, D., Hönig, S. F., Lonsdale, C. J., Smith, H. E., Houck, J. 2007, ApJ, in press (astro-ph/0709.4458)

The work on this project resulted from an invitation by first author Maria Polletta, which resulted in a very close and fruitful collaboration. In the framework of the PhD thesis, the new radiative transfer models were used to interpret the IR observations of obscured QSOs at intermediate redshift. On the basis of the model results, the idea of an additional cold absorber was introduced and consequences were discussed.

7.1. Introduction

7.1.1. Obscured AGN at high luminosities

Multiple X-ray studies show that the fraction of active galactic nuclei (AGN) whose emission is heavily absorbed ($N_{\text{H}} \geq 10^{22} \text{ cm}^{-2}$) decreases with increasing luminosity (from $>80\%$ at $L_X = 10^{42} \text{ erg s}^{-1}$, to 38% at $10^{45} \text{ erg s}^{-1}$; Akylas et al. 2006). However, because of the difficulty in detecting and identifying absorbed AGN, it is still unclear whether their paucity at high luminosities is an observational selection effect or real (La Franca et al. 2005; Treister & Urry 2006; Akylas et al. 2006; Tozzi et al. 2006). In order to overcome these uncertainties, searches for absorbed QSOs have focused on observations at wavelengths less affected by absorption, i.e., infrared (IR) and radio, e.g., FIRST, 2MASS and various Spitzer surveys (e.g. Wilkes et al. 2002; Urrutia et al. 2005; Polletta et al. 2006; Martínez-Sansigre 2006; Lacy et al. 2007).

These searches have unveiled a large population of QSOs obscured at optical wavelengths. Assuming that all optically obscured QSOs are also absorbed in X-rays, the fraction of absorbed QSOs would be $\geq 50\%$ of all QSOs (Martínez-Sansigre 2005). This fraction is still significantly lower than the fraction measured for AGN at lower luminosities, 80% (Osterbrock & Martel 1993; Akylas et al. 2006).

7.1.2. The obscuring matter in AGN

Obscuration in AGN at X-ray energies is caused by a mixture of neutral and ionized gas, as well as dust. Absorption by gas is usually observed in the X-rays through the suppression of soft X-ray emission with an energy cut-off that increases with the gas column density, N_{H} . The absorbing gas is mainly located in the circumnuclear region as suggested by measured variability (Risaliti et al. 2005, 2007), but gas in our Galaxy and in the host galaxy will also contribute to the overall absorption. Obscuration by dust is usually observed at optical and IR wavelengths where the continuum and broad

emission lines are reddened and, in some cases, completely suppressed. In the near- and mid-IR (NIR and MIR), dust obscuration interplays with thermal re-emission from the putative parsec-scaled dust torus. Depending on the actual geometry, optical depth and chemistry, dust absorption features at about 10 and $18\mu\text{m}$ due to silicates (Si) can be present in the IR.

According to AGN unification models (e.g. Antonucci 1993) and to torus models (e.g., Pier & Krolik 1992; Efstathiou & Rowan-Robinson 1995; Granato et al. 1997; Nenkova et al. 2002; Hönig et al. 2006) optical depths are expected to be at least roughly correlated from the X-ray to the MIR, although this correlation might be very weak for clumpy tori. In obscured AGN, the line of sight (LOS) intercepts the putative torus and thus absorbs radiation from the nucleus (broad emission lines, X-rays and thermal radiation from hot dust), while in unobscured AGN the radiation from the nucleus is directly visible and thus unabsorbed. An edge-on view of the torus is characterized by red optical through IR colors and Si features in absorption (at 10 and $18\mu\text{m}$), while a face-on torus has bluer colors and absent or Si features in emission. Sources with narrow emission lines in their optical spectra, red colors and strong Si absorption features are usually associated with a highly inclined torus and thus are expected to be also absorbed in the X-rays. However, there is emerging evidence for a surprising mismatch between the absorption measured in the X-rays and that measured in the optical through IR for a significant fraction of sources, especially at high luminosities.

AGN selected in the mid-IR sometimes show broad optical emission lines, though having absorption features in their IR spectra (Brand et al. 2007). The comparison between X-ray absorption and optical obscuration in various X-ray selected AGN samples shows that about 20–30% of obscured AGN are not absorbed in the X-rays and vice versa (e.g. Perola et al. 2004; Tozzi et al. 2006; Tajer et al. 2007; Gliozzi et al. 2007). The MIR spectra of a sample of type 2 QSOs with heavy X-ray absorption did not reveal the Si feature in absorption at $10\mu\text{m}$ (Sturm et al. 2006) as expected. This mismatch is even more pronounced at high luminosities. Indeed, absorption signatures in the IR, e.g. the Si absorption feature at $10\mu\text{m}$, are more prominent at the high luminosities of ultra luminous IR galaxies (ULIRGS) (Sanders & Mirabel 1996; Hao et al. 2007), while X-ray absorption is progressively less common in AGN with increasing luminosity (Ueda et al. 2003; Hasinger et al. 2005). These results suggest that a non-negligible fraction of obscured AGN might not be obscured by a torus, but by dust in either the narrow line region (Sturm et al. 2005) or in the host galaxy and that large X-ray column densities are not always associated with geometrically and optically thick dust distributions (see also Rigby et al. 2006; Martínez-Sansigre 2006). Alternatively, this mismatch can be explained by a low dust-to-gas ratio (A_V/N_H) or by a different path for the IR and the X-ray LOSs, e.g. due to clumpiness (Maiolino et al. 2001a; Shi et al. 2006, and also Sect. 6.5).

Large optical depths for Si absorption features (>1.7) usually imply a compact source deeply embedded in a smooth distribution of material which is both geometrically and optically thick, rather than absorption by a foreground screen of dust (Levenson et al. 2007; Imanishi et al. 2007). On the other hand, a detached foreground cold absorber which is far enough from the heating source to be cold can produce large Si optical depths. Deep ($\tau_{Si} > 1.7$) Si absorption features are usually considered as indicators of

a buried compact source such as an AGN. However, it is not clear whether the optical depth is a consequence of a random alignment of Si clouds or a specific dust distribution and orientation. The observed MIR spectra of obscured AGN do not favor the latter scenario because the Si absorption features are not always present in the spectra of optically obscured and X-ray absorbed AGN, as would be expected if the Si absorbers were associated with the same material which suppresses the broad emission lines and the soft X-ray emission.

In order to investigate the nature of the obscuring matter in extremely luminous AGN and assess how often the absorption signatures at optical, X-ray and infrared wavelengths do not correlate, a comprehensive analysis of the absorption properties at all wavelengths of obscured AGN at high luminosity is necessary, as well as detailed studies of their absorbing matter. Observations at various wavelengths from X-ray to optical and IR constrain the absorption along multiple LOSs and thus the geometry and distribution of the absorbing matter.

In this work, we investigate the observed properties of the obscuring matter in a sample of obscured and extremely luminous AGN, and we model their SEDs with our clumpy torus models (Hönig et al. 2006, see Chapter 2) to explore the dust geometries associated with large obscuration. This study is based on a sample of extremely luminous and obscured AGN for which multi-wavelength SEDs and IR spectra are available. The selected sample includes sources from the three widest *Spitzer* extragalactic surveys which were observed with the *Spitzer* InfraRed Spectrograph (IRS; Houck et al. 2004). In Sect. 7.2, we describe the sample selection, and in Sect. 7.3 the observations and the data used in this work are explained. In Sect. 7.4, the photometry and IRS spectra are presented and compared to model SEDs obtained by our clumpy torus model. The composite spectra of two sub-samples defined on the basis of the model results are analyzed in Sect. 7.5. The X-ray properties and a comparison between the absorption seen in the X-ray and the optical depth in the IR are described in Sect. 7.6. Implications on the nature of the obscuring medium are discussed in Sect. 7.7. Our results are summarized in Sect. 7.8.

Throughout the paper, the term “absorbed” refers to X-ray sources with effective column densities $N_{\text{H}} \geq 10^{22} \text{ cm}^{-2}$, and “obscured” to sources with red optical-IR colors, e.g. $F(3.6\mu\text{m})/F(r') > 20$ or $F(24\mu\text{m})/F(r') > 100$, implying dust extinction. The IR SEDs are defined “red” if they are as red or redder than a power-law model, $F_{\nu} \propto \nu^{\alpha}$, with slope $\alpha = -2$. The terms type 1 and type 2 refer to AGN with broad and narrow optical emission lines, respectively, in their optical spectra. We adopt a flat cosmology with $H_0 = 71 \text{ km s}^{-1} \text{ Mpc}^{-1}$, $\Omega_M = 0.27$ and $\Omega_{\Lambda} = 0.73$ (Spergel et al. 2003).

7.2. Sample description

There are three large area *Spitzer* surveys with IRAC, MIPS, and optical photometric coverage, the 50 deg^2 *Spitzer* Wide-Area Infrared Extragalactic Survey (SWIRE¹; Lonsdale et al. 2003, 2004); the 9 deg^2 NOAO Deep Wide-Field Survey (NDWFS) of

¹<http://swire.ipac.caltech.edu/swire/swire.html>

the Boötes field (Murray et al. 2005); and the 3.7 deg² Extragalactic First Look Survey (E-FLS²).

The initial objective for *Spitzer* IRS spectroscopy of sources chosen from these surveys was to understand populations of new sources that would not have been known prior to *Spitzer*. Consequently, priority was given to sources which are optically very faint, typically $\text{mag}(R) > 24$, and IR bright, i.e. $F(24\mu\text{m}) > 1 \text{ mJy}$. Various selection criteria based on IRAC colors also entered choices of spectroscopic targets, but the common characteristic of existing spectroscopic samples is their high ratio of mid-infrared to optical flux, $\text{IR/opt} = \nu F_\nu(24\mu\text{m})/\nu F_\nu(R)$. Most sources chosen for spectroscopy have $\text{IR/opt} \geq 10$. For 58 sources observed in Boötes (Houck et al. 2005; Weedman et al. 2006c), 70 sources observed in the FLS (Yan et al. 2007; Weedman et al. 2006b), and 20 sources in the SWIRE Lockman Hole field (Weedman et al. 2006a), the majority are at high redshift ($z \sim 2$) and many have infrared spectra dominated by a strong silicate (*Si*) absorption features at rest frame $9.7\mu\text{m}$. The presence of this absorption combined with the red colors and high luminosities of these sources led these previous observers to the conclusion that IR bright sources with large IR/optical flux ratios are dominated by obscured AGN (or QSOs because of their very high luminosities). A minority of sources in these studies show strong PAH emission features characteristic of starbursts, but these sources generally do not show strong *Si* absorption, so different populations of AGN and starbursts are observed.

If the interpretation of the obscured sources as AGN is correct, this implies a significant population of luminous, obscured QSOs. It is essential, therefore, to verify the AGN classification and to understand the obscured sources in context of models for AGN.

Our goal in this work is to determine quantitative AGN models for the most luminous of these obscured sources. The primary objectives is to investigate the properties of the AGN emission and the nature of the obscuration in AGN at high luminosities. To achieve this goals, we have selected, for detailed modeling, the most luminous of the obscured sources with AGN-dominated MIR SEDs from the archival *Spitzer* spectroscopy in the survey fields mentioned. Our selection criteria are the following: (1) high redshift, i.e. $z > 1$; (2) large MIR luminosities, i.e. $6\mu\text{m}$ luminosities, $\nu L_\nu(6\mu\text{m}) = L(6\mu\text{m}) \geq 10^{12} L_\odot$; (3) the presence of *Si* in absorption in the IRS spectra; and (4) red MIR SEDs consistent with being AGN-dominated (see e.g. Polletta et al. 2006; Alonso-Herrero et al. 2006). There are 21 sources that satisfy all those criteria; 15 are from the literature (Houck et al. 2005; Weedman et al. 2006a; Yan et al. 2007, Smith et al., in prep.), and 6 are from our own IRS observing programs. As a consequence of these selection criteria, all sources have $24\mu\text{m}$ fluxes greater than 1 mJy and have relatively large IR/optical flux ratios, i.e. $F(24\mu\text{m})/F(r') > 400$. To our knowledge this sample contains all sources in the literature that satisfy the mentioned selection criteria. However, this sample is not meant to be complete or unbiased since it is mainly based on the availability of IRS spectra.

The selected sample includes the most luminous obscured QSOs currently known. The large MIR luminosities of the selected targets enable us to measure the emission from the hottest dust in the torus with negligible contribution from the host galaxy,

²<http://ssc.spitzer.caltech.edu/fls/>

providing a laboratory to test the predictions of torus models in obscured AGN. Up to now, these kinds of uncontaminated SEDs could be sampled only using high spatial resolution data in nearby AGN (e.g. in NGC 1068; Hönig et al. 2006). By combining samples from the widest *Spitzer* surveys, we were able to find a significant number of these rare objects.

The list of selected sources, coordinates, optical and IR fluxes are reported in Table 7.1. For simplicity, we use throughout the paper simplified names for the selected sources. Official IAU names are reported in Table 7.1. For the SWIRE sources, the first two letters in their names designate the field where they were discovered (LH for Lockman Hole, N1 for ELAIS-N1, and N2 for ELAIS-N2). The first letter of the NDWFS source names is B for Boötes. The names of the FLS sources correspond to those in Yan et al. (2007).

7.3. Observations and Data Analysis

7.3.1. Sample Data

Multi-band photometric data in the optical from the ground and in the IR from *Spitzer* are available for all sources. The available data and references are listed in Table 7.1. All sources are detected with the Multiband Imaging Photometer on *Spitzer* (MIPS; Rieke et al. 2004) at $24\ \mu\text{m}$ with fluxes ranging from 1.0 to 10.6 mJy, and median flux of 2.6 mJy. All sources have been observed with the *Spitzer* Infrared Array Camera (IRAC; Fazio et al. 2004) in 4 bands, from 3.6 to $8.0\ \mu\text{m}$. The FLS sources have few detections with IRAC, probably because of the less sensitive observations compared to the NDWFS and SWIRE surveys. Eight sources have been observed in 5 optical bands, from *U*- to *z*-band, 3 in 4 bands, 5 in 3 bands, and 5 in 1 band. IRAC fluxes for the FLS sources were obtained from Sajina et al. (2007), and those for the SWIRE sources were taken from the latest internal catalogs that will be released in the Data Release 6 (for details on the data reduction see Surace et al. 2005).

The IRAC fluxes of the sources in the NDWFS survey were measured from the post-BCD images in the *Spitzer* archive. Aperture fluxes were measured within a $2''.9$ radius aperture at their position and background subtracted. Aperture corrections as derived from the SWIRE survey were applied. The aperture corrections are 1.15, 1.15, 1.25, and 1.43, for the four IRAC bands, respectively.

All sources have been observed in the optical *r'*- or *R*-band and 16/21 have been detected. The $f_{24\mu\text{m}}/f_R$ flux ratio ranges from 575 to 25000 with a median value of 3500.

IRS data were in part taken from the archive and in part from our own projects (Houck et al. 2005; Weedman et al. 2006a). The spectroscopic observations were made with the IRS Short Low module in order 1 (SL1) and with the Long Low module in orders 1 and 2 (LL1 and LL2), described in Houck et al. (2004)³ providing low resolution spectral coverage from $\sim 8\ \mu\text{m}$ to $\sim 35\ \mu\text{m}$. The main parameters of the IRS observations are listed in Table 7.2.

³The IRS was a collaborative venture between Cornell University and Ball Aerospace Corporation funded by NASA through the Jet Propulsion Laboratory and the Ames Research Center

Table 7.1: Optical and infrared data of the obscured QSOs sample

Survey Name	Source Name	LAT Name	F_{U}^a (μ Jy)	$F_{g'/r'}^a$ (μ Jy)	$F_{r'/r}^a$ (μ Jy)	$F_{i'/i}^a$ (μ Jy)	F_z^a (μ Jy)	$F_{3.6\mu m}$ (μ Jy)	$F_{4.5\mu m}$ (μ Jy)	$F_{5.8\mu m}$ (μ Jy)	$F_{8.0\mu m}$ (μ Jy)	$F_{24\mu m}$ (μ Jy)	$F_{70\mu m}$ (mJy)	$F_{160\mu m}$ (mJy)	Ref.
SWIRE	LH_01	SWIRE J104148.93+592233.0	<0.441	<0.326	<0.486	<0.821	...	5.4	12	<43	120	1351	<17.0	<90	1
SWIRE	LH_02	SWIRE J104605.50+585742.4	<0.441	<0.326	<0.486	<0.821	...	12	20	69	124	1407	<17.0	<90	1
SWIRE	LH_A4	SWIRE J104409.95+585224.8	0.360	1.038	1.186	1.312	1.823	64	150	391	1093	4134	<17.0	<90	3
SWIRE	LH_A5	SWIRE J104453.07+585453.1	0.236	0.333	0.409	0.611	<1.000	69	141	292	467	1190	<17.0	<90	3
SWIRE	LH_A6	SWIRE J104613.48+585941.4	1.115	1.799	1.993	2.850	3.535	27	34	58	127	1147	<17.0	<90	3
SWIRE	LH_A8	SWIRE J104528.29+591326.7	<0.441	0.517	1.042	2.223	3.654	32	45	91	207	2462	9.8	<90	3
SWIRE	LH_A11	SWIRE J104314.93+585606.3	<0.411	<2.473	<2.324	<3.269	...	9.2	22	60	117	968	<17.0	<90	3
SWIRE	N1_09	SWIRE J160532.69+535226.4	<0.801	1.107	1.491	1.914	<3.784	15	21	<43	73	2894	8.5	<90	2
SWIRE	N2_06	SWIRE J163511.43+412256.8	<0.801	<0.409	<0.752	<1.324	<3.784	14	18	36	116	4231	10.3	<90	2
SWIRE	N2_08	SWIRE J164216.93+410127.8 ^b	<0.801	<0.409	<0.752	<1.324	<3.784	72	176	475	1178	3984	<17.0	80.5	2
SWIRE	N2_09	SWIRE J164401.40+405715.0	<0.801	<0.409	<0.752	<1.324	<3.784	39	58	86	143	3715	27.5	121	2
NDWFS	B1	SST24 J143001.91+334538.4 ^c	...	0.142	0.302	0.521	...	8	29	102	586	3800	<30.0	...	2
NDWFS	B2	SST24 J143644.22+350627.4 ^d	...	0.325	0.525	0.753	...	43	97	380	732	2300	<30.0	...	2
NDWFS	B3	SST24 J142827.19+354127.7	...	0.980	2.290	5.210	...	296	621	1601	3939	10550	<30.0	...	2
NDWFS	B4	SST24 J142648.90+332927.2 ^e	...	0.514	0.912	1.194	...	53	178	493	911	2300	<30.0	...	2
NDWFS	B5	SST24 J143508.49+334739.8	...	0.390	0.692	0.905	...	12	21	34	237	2600	<30.0	...	2
FLS	MIPS42	SST24 J171758.44+592816.8	0.186	<9	30	103	680	4712	12.8	...	4, 5
FLS	MIPS78	SST24 J171538.18+592540.1	0.186	<9	39	<72	268	2973	<3.9	...	4, 5
FLS	MIPS15840	SST24 J171922.40+600500.4	0.462	18	25	62	197	1821	<4.8	...	4, 5
FLS	MIPS22204	SST24 J171844.38+592000.5	2.996	<27	39	132	478	4101	13.2	...	4, 5
FLS	MIPS22303	SST24 J171848.80+585115.1	0.395	<9	<12	<54	103	2030	7.2	...	4, 5

Note — Typical uncertainties to the optical and IR fluxes are $\sim 4\%$, and 10% of the measured fluxes, respectively. Upper limits correspond to 5σ .

^a The optical data correspond to $U_g/r'/i'/z$ in SWIRE, to UBRI in NDWFS, and R in FLS.

^b Also known as ELAIS15 J164216.9+410128.

^c N. 9 in Houck et al. (2005).

^d Also known as NDWFS J143644.3+350627 and N. 13 in Houck et al. (2005).

^e Also known as FIRST J142648.9+332927 and ELAIS15 J142648.9+332927.

References — (1) Smith et al., in prep.; (2) this work; (3) Weedman et al. (2006a); (4) IRAC data from Sajina et al. (2007); (5) R-band and MIPS[24] data from Yan et al. (2007).

Table 7.2.: IRS Low resolution Spectroscopy Observation Log

Source Name	Program ID	SL1 (seconds)	LL2 (seconds)	LL1 (seconds)
LH_01	136	3×60	6×120	6×120
LH_02	136	3×60	6×120	6×120
LH_A4 ^a	15	2×60	3×120	3×120
LH_A5 ^a	15	3×60	6×120	6×120
LH_A6 ^a	15	3×60	6×120	6×120
LH_A8 ^a	15	2×60	3×120	3×120
LH_A11 ^a	15	5×60	6×120	6×120
N1_09	15	3×60	3×120	3×120
N2_06	15	2×60	2×120	2×120
N2_08	15	2×60	2×120	2×120
N2_09	15	2×60	2×120	2×120
B1	12	1×240	2×120	2×120
B2	15	3×60	3×120	3×120
B3	15	2×60	2×120	2×120
B4	15	2×60	3×120	3×120
B5	15	3×60	3×120	3×120
MIPS42	3748	2×240	2×120	3×120
MIPS78	3748	2×240	2×120	3×120
MIPS15840	3748	2×240	6×120	7×120
MIPS22204	3748	2×240	2×120	3×120
MIPS22303	3748	...	2×120	3×120

^a IRS data processed with version 11.0 of the SSC pipeline.

Since the objects have similar properties in terms of SED and fluxes, we applied the same reduction procedure to all spectra for uniformity. The reduction method is described in detail in Weedman et al. (2006a) and briefly summarized here. Six SWIRE sources (see details in Table 7.2) were processed with version 11.0 of the SSC pipeline; the remaining sources were processed with version 13.0. Extraction of source spectra was done with the SMART analysis package (Higdon et al. 2004). Since the selected sources are faint and the spectra are dominated by background signal, we restricted the number of pixels used to define the source spectrum to a width of only 4 pixels (scaling with wavelength) in order to improve the spectral signal-to-noise (S/N). The flux correction necessary to change the fluxes obtained with the narrow extraction to the fluxes that would be measured with the standard extraction provided for the basic calibrated data was measured by extracting an unresolved source of high S/N with both techniques, and this correction (typically $\sim 10\%$ but varying with wavelength) was applied to all sources.

A search in the literature provided additional data for 6 sources in the sample, an ISO 15 μ m flux measurement for N2_08 (Gonzalez-Solares et al. 2005), and MAMBO 1.2mm flux upper limits for all 5 E-FLS sources (Lutz et al. 2005).

7.3.2. Luminosities, redshift, and optical depth

The SEDs and IRS spectra of all sources in the sample are shown in Fig. 7.1. The displayed spectra have been boxcar-smoothed to three times the approximate resolution of the different IRS modules ($0.2 \mu\text{m}$ for SL1, $0.3 \mu\text{m}$ for LL2, and $0.4 \mu\text{m}$ for LL1). The MIPS $24 \mu\text{m}$ fluxes typically agree within 10% to the $24 \mu\text{m}$ IRS flux. Spectroscopic redshifts are derived from the IRS spectra based on the location of the *Si* feature. Only in 2 cases (LH_A4, and B3) are optical spectroscopic redshifts available (Polletta et al. 2006; Desai et al. 2006). For most of the sources, IR spectroscopic redshifts were previously reported (Weedman et al. 2006a; Yan et al. 2007; Houck et al. 2005), although we have revised some of them. The estimated redshifts are reported in Table 7.3. Based on the comparison with previous z determinations and with the spectroscopic redshifts, we estimate that uncertainties associated with these redshifts are as much as ± 0.2 for the sources with the poorest S/N.

The *Si* feature in absorption is clearly observed in 18 objects (LH_02, LH_A4, LH_A5, LH_A6, LH_A8, LH_A11, N1_09, N2_08, N2_09, B1, B2, B3, B4, B5, MIPS42, MIPS78, MIPS22204, MIPS22303), and only marginally observed in 3 objects (LH_01, N2_06, MIPS15840). The apparent optical depth of the *Si* feature, τ_{Si} , is measured as $\ln(F_{9.7\mu\text{m}}^{\text{int}}/F_{9.7\mu\text{m}}^{\text{obs}})$, where $F_{9.7\mu\text{m}}^{\text{obs}}$ is the observed flux at $9.7 \mu\text{m}$, at the minimum of the *Si* feature, and $F_{9.7\mu\text{m}}^{\text{int}}$ is the intrinsic flux at $9.7 \mu\text{m}$ that would arise from an extrapolated, unabsorbed continuum. Since in most of the cases, the SEDs and spectra do not sample the wavelength region beyond the *Si* feature, we cannot use the standard method to derive the intrinsic continuum (see e.g. Spoon et al. 2004). The intrinsic flux at $9.7 \mu\text{m}$ is thus estimated using two different methods, (1) by extrapolating a 4–8 μm rest-frame power-law fit to $9.7 \mu\text{m}$, and (2) by normalizing an unobscured AGN template to the observed $7.4 \mu\text{m}$ flux, after redshifting it to the redshift of each source, and reddening it using the Galactic Center extinction curve (Chiar et al. 2006) until the observed *Si* feature is well reproduced. The *Si* optical depth, τ_{Si} , is measured only in sources at $z < 2.7$, 18 sources. For the remaining objects, we estimate a lower limit since we have only an upper limit to the flux at the bottom of the *Si* feature. The measured values, reported in Table 7.3, vary from >0.2 to 3.4.

7.4. Modeling the SEDs with clumpy torus models

7.4.1. Torus Models

The optical-IR SEDs and re-binned IRS spectra of all 21 sources are shown in Fig. 7.1. The IR SEDs, from 3.6 to $24 \mu\text{m}$, and IRS spectra are modeled with a grid of torus models from Hönig et al. (2006), and the residuals in the near-IR (NIR) are fit with a galaxy template to represent the host galaxy. The model parameters are the cloud density distribution (from compact to extended), the vertical distribution (with various degrees of flaring or non-flaring), the number of clouds along the LOS (\sim optical depth), and the torus inclination (from face-on to edge-on). The best model is the one that gives the best fit, based on a χ^2 -test, to the five broad-band photometric data points from 3.6 to $24 \mu\text{m}$ and to a maximum of six additional data points derived by interpolating the IRS spectrum at $\lambda = 3, 5, 7, 8.5, 9.7,$ and $12 \mu\text{m}$ in the rest-frame.

Table 7.3.: Redshift, observed 6 μm luminosity, and optical depths of our QSO2 sample.

Source ID	z	$\log \nu L_\nu(6.0 \mu\text{m})^{\text{a}}$	$\tau_{Si}^{PL}{}^{\text{b}}$	$\tau_{Si}^{Temp}{}^{\text{c}}$
LH_01	2.84	46.09	>0.79	>0.37
LH_02	2.12	45.67	1.98	0.91
LH_A4	2.54 ^d	46.45	0.87	0.57
LH_A5	1.94 ^e	45.64	0.63	0.41
LH_A6	2.20 ^e	45.68	0.43	0.18
LH_A8	2.42 ^e	46.16	0.86	0.33
LH_A11	2.30 ^e	45.73	0.85	0.38
N1_09	2.75	46.40	>0.86	>0.42
N2_06	2.96	46.61	>0.67	>0.20
N2_08	2.40	46.42	1.78	1.14
N2_09	1.98	46.09	1.01	0.15
B1	2.46	46.41	2.36	1.49
B2	1.77	45.90	0.88	0.71
B3	1.293 ^d	46.30	0.43	0.21
B4	1.82	45.78	1.72	1.21
B5	2.00	46.04	2.43	1.39
MIPS42	1.90 ^f	46.21	0.42	0.13
MIPS78	2.43 ^f	46.23	1.04	0.58
MIPS15840	2.23 ^f	45.97	0.37	0.10
MIPS22204	2.08	46.20	1.04	0.58
MIPS22303	2.50 ^f	46.14	1.10	0.80

^a Luminosity is given in unit of erg s^{-1} .

^b Silicate optical depth derived from $\ln(F_{9.7\mu\text{m}}^{\text{int}}/F_{9.7\mu\text{m}}^{\text{obs}})$ with $F_{9.7\mu\text{m}}^{\text{int}}$ estimated extrapolating a power-law model fit to the data at $\lambda < 7\mu\text{m}$ in the rest-frame.

^c Silicate optical depth derived from $\ln(F_{9.7\mu\text{m}}^{\text{int}}/F_{9.7\mu\text{m}}^{\text{obs}})$ with $F_{9.7\mu\text{m}}^{\text{int}}$ estimated from a type 1 QSO template normalized at the observed $24\mu\text{m}$ flux and redshifted to the redshift of the source.

^d Optical spectroscopic redshift for LH_A4 from Polletta et al. (2006) and for B3 from Desai et al. (2006).

^e LH_A5: $z=1.89$, LH_A6: 2.10, LH_A8: 2.31, LH_A11: 2.25 in Weedman et al. (2006a).

^f MIPS42: $z=1.95\pm 0.07$, MIPS78: $z=2.65\pm 0.1$, MIPS15840: $z=2.3\pm 0.1$, MIPS22303: $z=2.34\pm 0.14$ in Yan et al. (2007).

The best-fit models are shown in Fig. 7.1 and the best-fit parameters are listed in Table 7.4. In order to fit the stellar component we adopt a 3 Gyr old elliptical template (from GRASIL, Silva et al. 1998). The choice of an elliptical template is justified by the evidence of ellipticals as hosts in the vast majority of quasars (e.g. Dunlop et al. 2003). In order to check the validity of our assumption on the host-galaxy, we estimated the associated R -band ($\lambda^{rest} = 0.7\mu m$) absolute magnitudes, M_R , and compared them with those measured for the large sample of quasars in Dunlop et al. (2003). The measured M_R range from -25.9 to -22.2 , and the median value is -23.7 . These values are consistent with those found by Dunlop et al. (2003), $M_R = -23.53 \pm 0.09$, but our sample shows a wider dispersion that can be attributed to the large uncertainty of our method and to the different redshift range. A host galaxy of later type cannot be ruled out, but the low number of detections in the optical, the lack of NIR (JHK) data, and contamination from the AGN light do not allow us to better constrain the host type. In most of the cases, the elliptical template provides an acceptable fit. Only in one source, LH_A8, the SED of the stellar component is not well fitted with an elliptical template because of an excess of emission at $\lambda^{rest} < 0.3\mu m$ and a late spiral template could provide a better fit. Note that a heavily obscured starburst galaxy would have an optical-NIR SED that is very similar to that of an elliptical galaxy.

The reduced χ^2 obtained by comparing the model with the data at $\lambda > 1\mu m$ in the rest-frame are reported in Table 7.4. We will refer to these as T (for torus) models (see also Table 7.4). In 11 cases, a T model well reproduces the observed IR SED and spectrum ($\chi^2_\nu < 1$). In the remaining 10 cases, poorer fits are obtained ($1 < \chi^2_\nu < 10$). In 3 cases the model underestimates the NIR emission (LH_A4, LH_A5, and N2_08), in 4 cases the model fails to reproduce the depth of the Si feature (B1, B4, MPS78, and MIPS22303), and in the remaining 3 cases the large χ^2_ν values are caused by either a noisy IRS spectrum (LH_02, and N2_09), or a poor fit at short wavelengths (N2_09, and MIPS22304). There are also 2 sources with good χ^2_ν but their fits do not well reproduce the Si feature. This is due to the fact that the feature is not well sampled by the representative values for the IRS spectrum. There is indeed only one data point in the Si feature.

7.4.2. Introducing a cold absorber

The main cause of failure in the fits with large χ^2_ν is the incapability of the models to simultaneously reproduce a prominent NIR emission and a deep Si absorption feature. Sources with deep Si features are expected to have weak NIR emission (e.g. Pier & Krolik 1992; Levenson et al. 2006). A NIR excess requires that hot dust is seen directly by the observer (typically happening only in weakly obscured objects), while the Si absorption feature requires the presence of a significant amount of optically and geometrically thick dust in the LOS (e.g. Pier & Krolik 1992; Granato et al. 1997; Levenson et al. 2006; Imanishi et al. 2007). This cooler dust component should absorb the hot dust emission from the vicinity of the obscured AGN.

We attempted, therefore, to model the SEDs of the objects with poor fits, as well as those of the rest of the sample with an alternative model that includes a cold absorber detached from the torus. We assume the Galactic Center extinction curve (Chiar et al. 2006) for the cold absorber. For simplicity, we do not model its re-emission, however

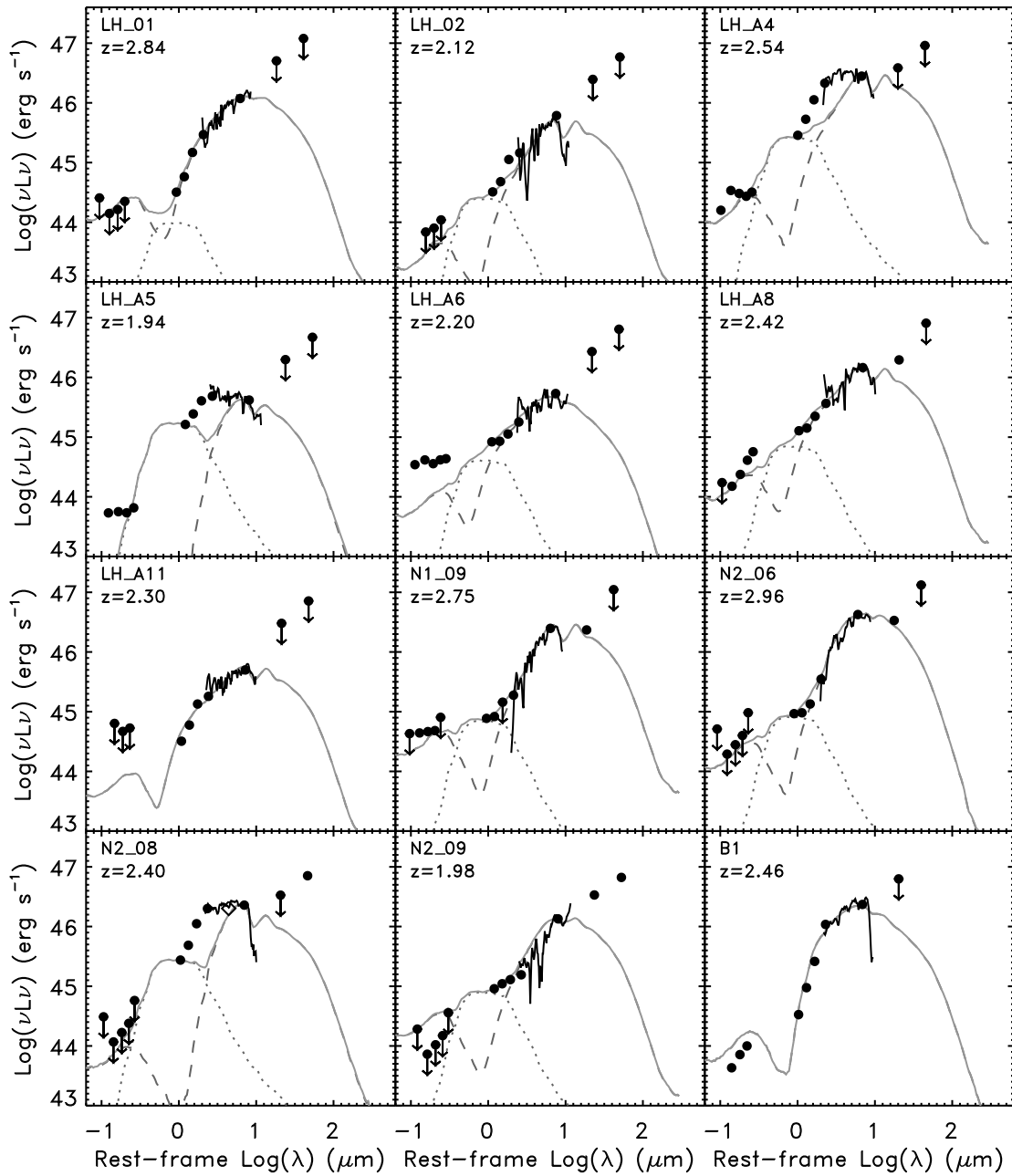
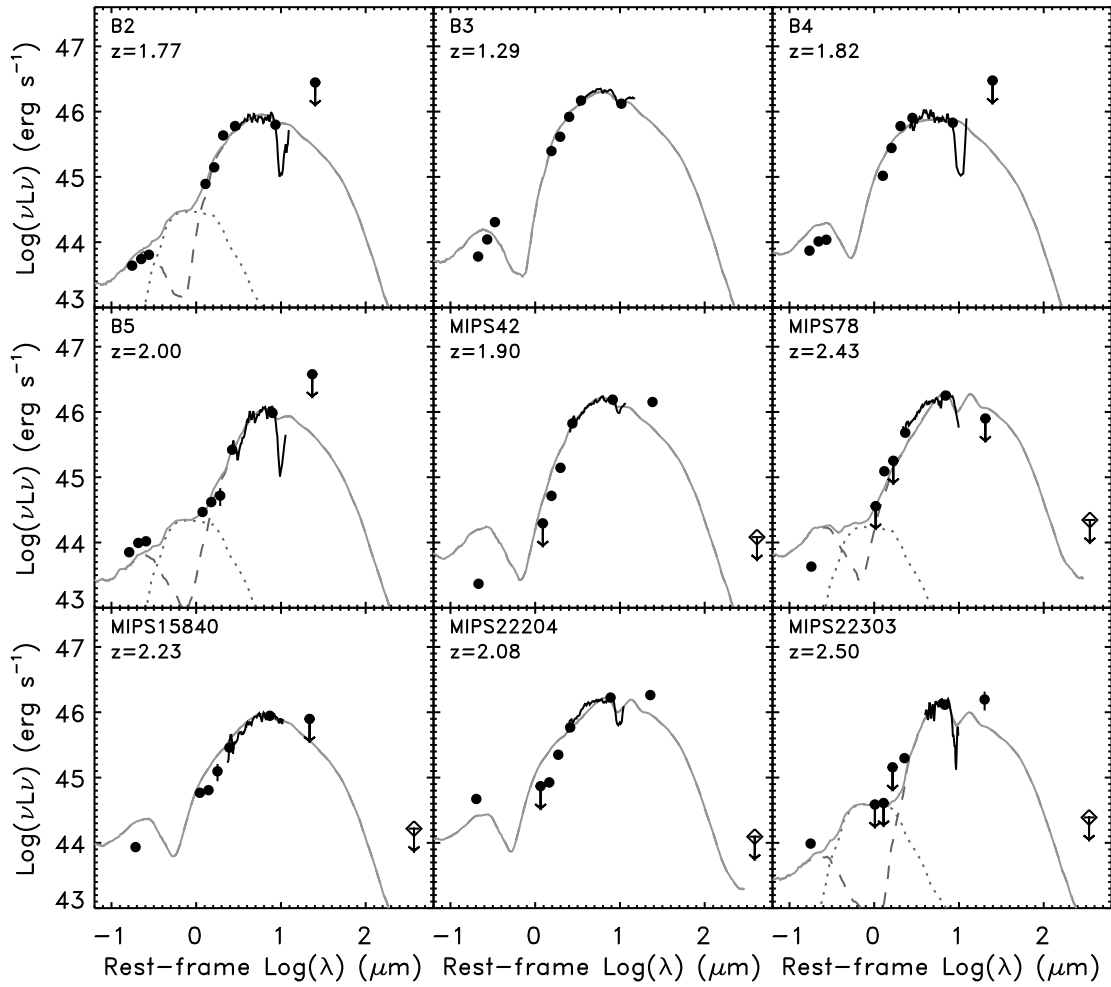


Figure 7.1.: Rest-frame spectral energy distributions in νL_ν vs λ (photometry: black symbols; IRS spectrum: black line) and best-fit model (solid grey line) obtained from a torus model (dashed grey line) and an elliptical template (dotted grey line) to fit the residuals in the near-IR. Open diamonds represent ISO $15\mu\text{m}$ and MAMBO 1.2mm data from Gonzalez-Solares et al. (2005) and Lutz et al. (2005), respectively. Downward arrows represent 5σ upper limits for the optical and infrared data points, and 3σ upper limits for millimeter data. Source names and redshifts are annotated.

Figure 7.1.: *Continued*

this should not affect our results since its re-emission is expected to occur at FIR wavelengths. The number of degrees of freedom in the χ^2_ν estimates is 4 in case of T models and 5 in case of T+C models. The cold absorber is able to produce deeper S_i features, and significantly improve the fits for 9 sources, as shown in Fig. 7.2. In 2 cases the χ^2_ν actually worsened, these are for B2 and B5, which already had good fits with the simple torus model. In these two sources the χ^2_ν is more sensitive to the broad-band photometric data than to the IRS spectrum because of our limited sampling in the observed deep S_i feature. But the two fits look equally good and from a visual inspection of the fits, we choose the model with the cold absorber component as preferred model because it better fits the S_i feature.

The torus+cold absorber models (T+C models hereinafter) were adopted for these 2 sources and for 7 sources for which the T+C model gives a significantly better fit (LH_A4, LH_A5, N2.08, B1, B2, B4, B5, MIPS78 and MIPS22303). In two cases (B4, and N2.08), even the T+C model does not provide a good fit to the NIR emission, although it is an improvement with respect to the T model. No improvement was obtained for the 3 sources with poor χ^2_ν (LH.02, N2.09, and MIPS22204), therefore for these we keep the simple T model. In addition to the T+C models, we also show in Fig. 7.2 the torus model before applying the extinction due to the cold absorber (see dot-dashed curve in Fig. 7.2). The cold absorber can absorb up to 60% of torus emission in the near-IR, as shown in Fig. 7.2.

In modeling the SEDs, we neglected the optical data. However, we notice that in most of the cases the predicted optical flux from the torus model is lower than the observed optical emission. The additional optical light might be associated with the host galaxy or with scattered light from the AGN. In 6 sources detected in the optical, the SED shows an upturn or a blue continuum toward shorter wavelengths, i.e. in the rest-frame far ultraviolet. This feature can be reproduced by either a population of young stars or by emission from the AGN accretion disk. The latter scenario is favored by source LH_A4 (aka SW104409). Its optical spectrum is dominated by a blue faint continuum, narrow emission lines, e.g. Ly α and C 4 λ 1549 with asymmetric and weak broad components (Polletta et al. 2006). The most likely explanation for the properties of the observed optical spectrum is that it is dominated by scattered light, and the scattering fraction is estimated to be <1% (Polletta et al. 2006).

In one case (N2.06), the LOS is at only 30° from the torus axis, implying an almost clear view of the nuclear region. Since no additional absorber is required by the data, we expect to see the nuclear emission directly. This seems in apparent contradiction with the faint optical emission of this object. Its best-fit model, however, predicts one optically thick cloud, associated with the torus, along the LOS (see Table 7.4). The presence of such a cloud in front of the optical emission source would be enough to absorb its intrinsic optical emission. The estimated apparent S_i optical depth in the model is $\tau_{S_i}=0.07-0.34$ which corresponds to a visual optical depth of 0.4–2.1 or to a suppression factor of the optical flux of 40%–0.8%. However, τ_{S_i} is poorly constrained by the data and in the model because this source is at $z=2.96$. The red MIR SED of this object would imply a much higher optical depth than derived by the S_i feature. A deeper S_i might be present implying a higher torus inclination or the presence of a cold absorber. On the other hand, it is also possible that our best-fit model is correct and

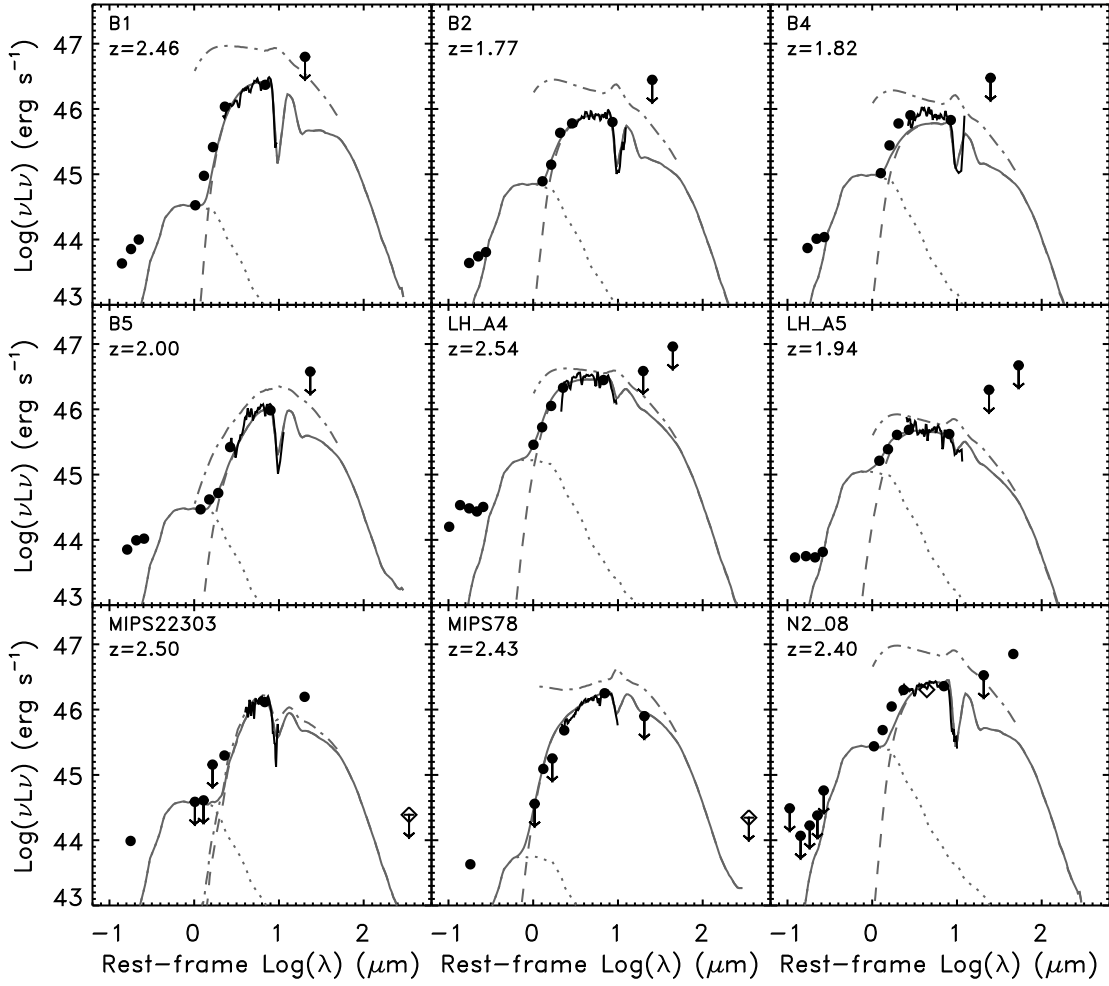


Figure 7.2.: Rest-frame spectral energy distributions in νL_ν vs λ (photometry: black symbols; IRS spectra: black line) and best-fit model (solid grey line) obtained from a torus+cold absorber model (dashed grey line) and an elliptical template (dotted grey line) to fit the residuals in the near-IR. The dot-dashed curve represents the torus model, in the 1–50 μm rest-frame wavelength range, before including the cold absorber. Symbols as in Figure 7.1. The name and redshift of each source are annotated.

that the source has only a weak Si absorption feature and a low inclination torus, as well as one optically thick cloud along the line-of-sight which is responsible for suppressing the optical and NIR nuclear light. This scenario might be quite common in obscured QSOs as suggested by a recent study of the IRS spectra of a sample of type 2 absorbed QSOs (Sturm et al. 2006).

7.4.3. Model parameters

Here, we analyze the model parameters of the best-fit models. In case of the 9 sources for which the T+C model is preferred, we consider only the parameters obtained with this model (see Table 7.4). The cloud density distribution, which can be considered as an indicator for a compact or extended torus, is expressed by a power-law, $n_r(r) \propto r^{-a}$, where r is the torus radius. In the models grid, the index a varies from 1 to 3 in steps of 0.5. Larger values of the index a indicate more compact distributions. Since values lower than 1 are not supported by theoretical considerations for an accretion scenario (Beckert & Duschl 2004), we set a minimum value for the parameter a of unity.

Trends of Si strength with a are different for our models compared to the models in Levenson et al. (2007). They do not model the dust distribution in a torus but instead use different dust distributions (slab and shell) around a central heating source and they do not consider the combination of a clumpy medium and an additional absorber as proposed here. According to Levenson et al. (2007), the strength of the Si absorption feature is a function of the temperature contrast in dust material, and, thus, a deep absorption feature favors a more extended dust distribution, i.e. $a=0-1$. However, for the majority of sources a compact torus is favored, $a=3$ is chosen in 9 cases, $a=2$ in 10 cases, and smaller values, $a \leq 1.5$, are preferred in only 2 sources.

The clouds' vertical distribution (flaring or non-flaring) is approximated by a power-law, $H(r) \propto r^b$, where H is the torus scale height and r the torus radius. In the model grid, the index b can assume values 1, 1.5, and 2. A non-flaring distribution ($b=1$) is preferred by 17 sources, and moderately flaring ($b=1.5$) is preferred only by 4 sources.

The torus inclination is defined by the angle θ between the torus axis and the LOS. A face-on torus has $\theta=0^\circ$ and an edge-on torus has $\theta=90^\circ$. In the models grid, the angle θ varies from 0 to 90° in steps of 15° . Our sources do not show a preferred torus inclination, indeed θ ranges from 0° to 90° , with most of the sources (13 sources) at intermediate values ($\theta=30-45^\circ$). All but two (B5 and MIPS22303) of the sources modeled with the T+C model and one of those with weak Si absorption feature (N2.06) favor a torus with little inclination, $\theta=0-30^\circ$. All of the others have inclined tori, $\theta \geq 45^\circ$. Therefore, optical obscuration or Si in absorption do not necessarily imply a LOS intercepting the torus (see also Rigby et al. 2006; Brand et al. 2007).

An additional model parameter is the number of clouds along the LOS, N_0^{LOS} . This parameter is the average number of clouds obtained from five different cloud arrangements for the same set of model parameters, and is thus indicative of the extinction of the AGN emission produced by the torus, $\tau_V^T \simeq N_0^{LOS}$ (Natta & Panagia 1984). The apparent optical depth in the Si feature of the T and T+C models, τ_{Si}^T and τ_{Si}^{T+C} , is measured following the same procedure applied to the data (see Sect. 7.3.2). The apparent optical depths so derived are reported in Table 7.4. The line-of-sight optical depths associated with the torus in the T models are $\tau_{Si}^T \leq 1.04$, with a median value

Table 7.4.: Torus model parameters

Source ID	Model ^a	a^b	b^c	θ^d	N_o^e	N_o^{LOSf}	τ_V^g	τ_{Si}^{PLh}	$\tau_{Si}^{Temp^h}$	χ_ν^{2i}
LH_01	T	3.0	1.5	60	12	6.0	0	0.29	0.01	0.016
LH_02	T	3.0	1.0	90	26	26.0	0	1.00	0.32	5.085
LH_A4	T	3.0	1.0	60	12	9.0	0	1.00	0.32	4.638
	T+C	2.0	1.0	15	26	0.0	6	0.62	0.35	0.575
LH_A5	T	1.5	1.5	60	18	17.5	0	0.83	0.27	6.665
	T+C	2.0	1.0	30	26	0.2	7	0.62	0.36	0.703
LH_A6	T	2.0	1.0	45	26	5.6	0	0.32	0.07	0.050
LH_A8	T	3.0	1.0	60	9	6.5	0	0.81	0.26	0.078
LH_A11	T	3.0	1.0	45	12	4.6	0	0.75	0.25	0.533
N1_09	T	3.0	1.0	60	12	9.0	0	1.04	0.29	0.021
N2_06	T	1.1	1.5	30	13	1.0	0	0.34	0.06	0.004
N2_08	T	2.0	1.0	90	26	26.0	0	1.05	0.40	10.120
	T+C	2.0	1.0	30	26	0.2	21	2.33	1.35	2.515
N2_09	T	3.0	1.5	45	8	5.2	0	0.49	0.04	2.307
B1	T	2.0	1.0	45	26	5.6	0	0.37	0.11	1.435
	T+C	3.0	1.0	15	26	0.0	25	2.94	1.64	0.042
B2	T	2.0	1.0	45	26	5.6	0	0.37	0.12	0.391
	T+C	2.0	1.0	30	26	0.2	18	1.85	1.07	0.540
B3	T	2.0	1.0	45	26	5.6	0	0.37	0.11	0.530
B4	T	2.0	1.0	30	26	0.2	0	0.01	0.00	10.000
	T+C	2.0	1.0	30	26	0.2	16	1.60	0.92	4.898
B5	T	2.0	1.0	45	26	5.6	0	0.56	0.14	0.006
	T+C	1.5	1.5	90	6	6.0	15	2.02	0.93	0.295
MIPS42	T	2.0	1.0	45	26	5.6	0	0.43	0.14	0.390
MIPS78	T	3.0	1.0	60	12	4.6	0	1.00	0.31	2.153
	T+C	3.0	1.0	30	9	0.3	10	0.93	0.40	0.003
MIPS15840	T	2.0	1.0	45	26	5.6	0	0.32	0.07	0.155
MIPS22204	T	3.0	1.0	45	12	4.6	0	0.75	0.25	2.957
MIPS22303	T	2.0	1.0	90	26	26.0	0	1.06	0.40	2.438
	T+C	2.0	1.0	90	26	26.0	4	1.54	0.68	0.775

^a T: torus model, T+C: torus+cold absorber model. The parameters for the T+C model are given only when the torus only (T) model gives a poor fit ($\chi_\nu^2 > 0.1$) to the observed SED and spectrum, or the T+C model significantly improves the χ^2 .

^b Index of the torus density radial distribution, $n_r(r) \propto r^{-a}$, where r is the torus radius.

^c Index of the vertical cloud distribution, $H \propto r^b$, where H is the torus scale height.

^d Inclination of the torus axis with respect to the line of sight in degrees.

^e Average number of clouds along an equatorial LOS.

^f Average number of clouds along the LOS, which approximately corresponds to the optical depth of the torus in the visual (Natta & Panagia 1984).

^g Cold absorber (C) optical depth in the optical.

^h Absorber (torus for model T and torus+cold absorber for model T+C) optical depth associated with the Si feature measured by extrapolating a power-law model (τ_{Si}^{PL}) or by fitting a QSO template (τ_{Si}^{Temp}) (see text).

ⁱ Reduced χ^2 obtained from the best-fit model and the observed data at $\lambda > 1 \mu\text{m}$ in the rest-frame.

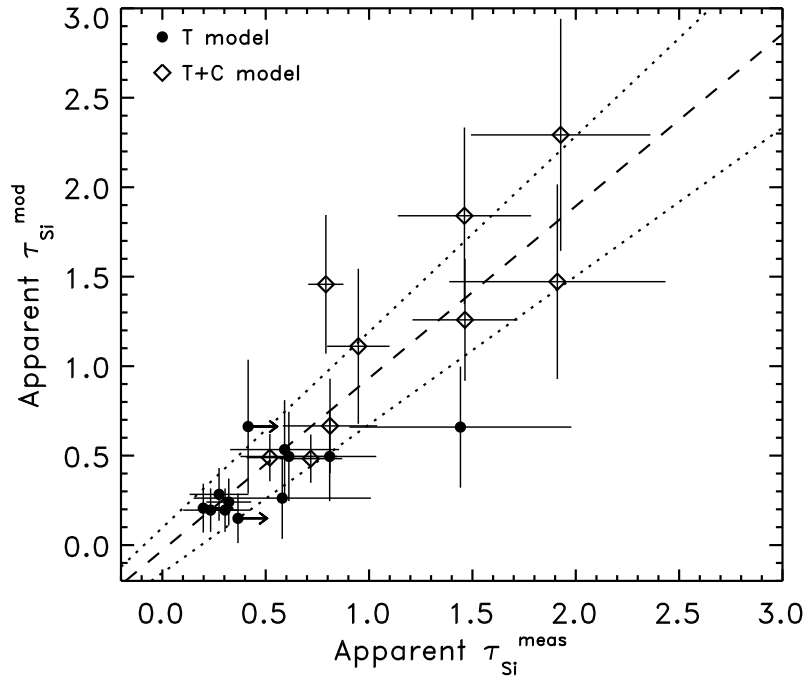


Figure 7.3.: Comparison between the apparent Si optical depth at $9.7\ \mu\text{m}$ measured from the SED and spectrum, as described in Sect. 7.3.2, and from the torus models, as described in Sect. 7.4. Full circles represent sources fit with a T model, diamonds represent sources fit with a T+C model. The dashed line represents the best linear fit between the modeled and the measured τ_{Si} , and the dotted lines include the 1σ uncertainties on the best-fit parameters.

of $\tau_{Si}^T = 0.13$ or 0.46 , depending on the method applied to estimate τ_{Si}^T . The optical depths associated with the cold absorber are $\tau_V^C = 4\text{--}25$, with a median value of 15. The apparent optical depths for the sources fit with the T+C model, τ_{Si}^{T+C} , range from 0.6 to 2.9, with a median value of 1.6, or from 0.4 to 1.4 with a median value of 0.9, depending on the method used to measure them.

In Fig. 7.3, we compare the modeled optical depths in the Si feature, τ_{Si}^{mod} , with the observed optical depths, τ_{Si}^{meas} (see Sect. 7.3.2). The modeled optical depths range from 0.01 to 2.9, considering both the T and T+C models. The modeled and measured τ_{Si} satisfy the relation

$$\tau_{Si}^{\text{mod}} = 0.96 \pm 0.13 \times \tau_{Si}^{\text{meas}} - 0.03 \pm 0.13. \quad (7.1)$$

Although there is a general agreement between the two estimates, it is clear that these kind of measurements are characterized by large uncertainties, especially in objects at high redshift for which the Si feature is not well sampled, and that it is a difficult task to model both the NIR–MIR continuum and the Si absorption feature.

In summary, we find that there is no preferred torus inclination associated with the detection of a *Si* feature in absorption. However, in the cases where the absorption feature is well detected and can be modeled by the torus model, the inclination is always higher than $\theta=45^\circ$, consistent with the LOS intercepting the torus. Sources with a less inclined torus require an additional absorber to explain the observed *Si* feature or show a weak *Si* feature. A compact non-flaring torus is preferred by the majority of the sources. The radial cloud density distribution indeed indicates that the torus emission region is compact, or that the near- and mid-IR emission is dominated by dust in the vicinity of the nucleus. The preferred non-flaring torus in the majority of these luminous sources is consistent with the predictions of the receding torus models (e.g. Simpson 2005; Hönig & Beckert 2007). According to these models, the opening angle of the torus increases at larger luminosities. Our results are in agreement with the predictions from Hönig & Beckert (2007). These authors claim that flaring should not occur in high luminosity sources because large clouds at large distances from the AGN should be driven away by the radiation pressure.

7.5. Composite IR spectra

In order to search for weak spectral features in the IRS spectra, the individual spectra were combined to obtain a composite spectrum with higher S/N. Composite spectra were made for 2 sub-samples: (1) sources fit with the T model (12 sources); and (2) sources fit with the T+C model (9 sources). The composite spectra were obtained by taking the median of all available spectra in bins of $\Delta(\log(\lambda))=0.007$ with λ in μm , after normalizing them at $6\mu\text{m}$ in the rest-frame. The uncertainty associated with the median value per bin corresponds to the uncertainty of the mean. The two composite spectra and associated 1σ uncertainties are shown in Fig. 7.4. The composite spectrum of the T group is characterized by a large dispersion, especially at $\lambda \simeq 10\mu\text{m}$. This large dispersion indicates that we combined sources with a broad range of depths in the *Si* feature.

Some spectral features other than *Si* that might be detected in the two composite spectra are highlighted, e.g., absorption features due to ice at $6.15\mu\text{m}$ and hydrocarbons (HAC) at $6.85\mu\text{m}$, the atomic emission feature [SIV] $\lambda 10.54\mu\text{m}$, the molecular hydrogen emission line H₂(S₃) $\lambda 9.66\mu\text{m}$, and the 6.2, 7.7, 8.6, and $11.3\mu\text{m}$ PAH emission features. Of these, the strongest feature that may be detected in both composite spectra is the $7.7\mu\text{m}$ PAH. This PAH is the strongest feature in starburst galaxies (Sturm et al. 2000; Brandl et al. 2006).

Absorption due to HAC might be present in both composite spectra. This might be associated with the matter that is also responsible for the deep *Si* feature, as in IRAS 00183–7111 (Spoon et al. 2004).

In order to facilitate a comparison between the two spectra, we overplotted a power-law model with slope of 2 normalized at $6\mu\text{m}$ in both panels of Fig. 7.4. The main differences among the spectra are the 2– $6\mu\text{m}$ spectral slopes and the depths and shapes of the *Si* feature. In group (1) (T model), the FWHM of the *Si* feature is $1.8\mu\text{m}$, the apparent optical depth is 0.4, and the 2– $6\mu\text{m}$ rest-frame power-law slope is 2.0. In group (2) (T+C model), the FWHM of the *Si* feature is $3.9\mu\text{m}$, the apparent optical

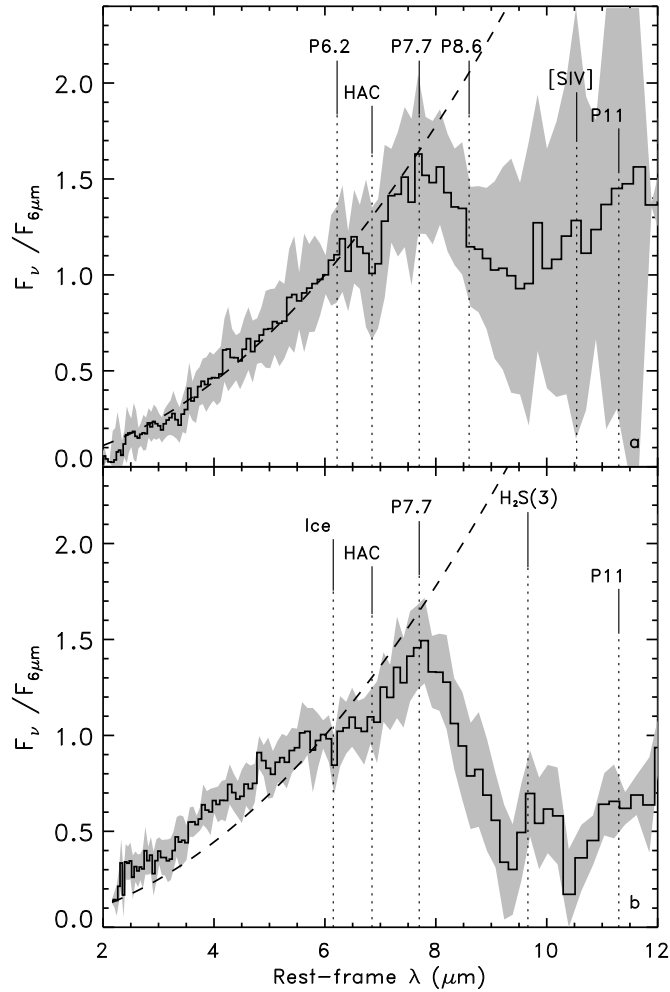


Figure 7.4.: Median normalized IRS spectra of two sub-groups of sources: (a) 12 sources modeled with the T model; and (b) 9 sources modeled with T+C model. The shaded area represents the mean absolute deviation. The dashed curve represents a power-law of slope $\alpha=2$ ($F_\nu \propto \nu^{-\alpha}$) normalized at $6\mu\text{m}$. Some spectral features that might be present are annotated.

depth is 0.9, and the $2\text{--}6\mu\text{m}$ rest-frame power-law slope is 1.7. It is interesting to note that, contrary to the expectation from torus models that the coldest dust is associated with the deepest Si absorption, the spectrum with the deepest Si feature (group 2) has the flattest NIR slope. This result supports the scenario proposed in Sect. 7.4 for the sources fit with the T+C models in which the hot dust close to the AGN is directly visible, and an additional absorber is required to reproduce the deep Si feature.

7.6. X-ray properties

7.6.1. Available data

X-ray data from *Chandra* are available for 11 sources, but only 5 are detected (LH_02, LH_A4, LH_A5, LH_A6, and LH_A8; Weedman et al. 2006a; Polletta et al. 2006, Smith et al., in prep.). *Chandra* 5 ksec observations are available for the 5 sources in the Boötes field (Murray et al. 2005), but none of the selected sources is detected. We report an upper limit to the broad-band (0.3-8 keV) X-ray flux for these sources corresponding to the 90% completeness limit (10^{-14} ergs cm $^{-2}$ s $^{-1}$) (Murray et al. 2005). LH_A11 is part of the 70 ksec SWIRE/*Chandra* survey (Polletta et al. 2006), but was not detected, thus we report an upper limit to the broad band flux of 10^{-15} ergs cm $^{-2}$ s $^{-1}$. *Chandra* observations for B2 are scheduled (CXO Proposal 08700396) and XMM-*Newton* observations are pending for N2_06, B1, N2_08, and B3 (XMM-*Newton* Proposal 050326). In Table 7.5, we list observed X-ray fluxes, estimated effective column densities and luminosities for the detected 5 sources, and upper limits to the fluxes for the remaining 6 sources. Here, we compare the absorption measured in the X-rays with the extinction measured in the IR and use the MIR to X-ray luminosity ratio to investigate the dust covering fraction in the selected sample.

7.6.2. X-ray absorption and IR extinction

The effective gas column densities responsible for absorption in the X-rays are derived from the X-ray hardness ratios using the method described in Polletta et al. (2006). The estimated values are reported in Table 7.5. The absorption measured in the X-rays and the dust extinction measured in the IR, τ_{Si} , are compared in Fig. 7.5. We also show a curve (dotted line) corresponding to equivalent N_H and τ_{Si} assuming a gas-to-dust ratio of 100, instead of the Galactic value, a dust density of 2.5 g/cm 3 and 0.1 μ m radius per dust grain, or $N_H \simeq 2.26 \times 10^{22} \times \tau_{Si}$ cm $^{-2}$.

In four sources, the N_H is significantly larger than that derived in the IR. The only exception, where the N_H is lower, is LH_A2 which is characterized by a soft X-ray spectrum. However, there is evidence, based on the X-ray/IR luminosity ratio, that in LH_A2 the observed X-ray spectrum corresponds to a small fraction of the intrinsic X-ray emission due to scattering, while the intrinsic emission is absorbed by a Compton-thick column density ($N_H > 10^{24}$ cm $^{-2}$) (Smith et al., in prep.). This source is also characterized by the highest IR extinction.

The large N_H values compared to the extinction measured in the IR by τ_{Si} are easily explained. The apparent Si optical depth underestimates the true extinction in the IR because its measurement does not take into account re-emission of radiation at the same wavelengths where absorption takes place. Moreover we expect the correlation between the two measurements of absorption to have a wide dispersion because the absorption measured in the X-rays can be highly variable (see e.g. Risaliti et al. 2007), and because the two columns, in the X-ray and in the IR, are measured along different paths as the emitting sources have different spatial locations and distributions. It is also quite plausible that, in addition to the absorption produced by the medium that is responsible for the extinction seen in the IR, the X-ray source suffers also from

Table 7.5.: X-ray properties of some of our sample objects.

Source ID	$F_{0.3-8keV}^a$ (10^{-15} ergs cm^{-2} s $^{-1}$)	N_H^{effb} (10^{22} cm $^{-2}$)	$\log(L_{0.3-8keV})$ (erg s $^{-1}$)	$\log(L_{0.3-8keV}^{corr}{}^c)$ (erg s $^{-1}$)
LH_02	4.51	$0.12_{-0.00}^{+4.10}$	44.07	44.08
LH_A4	1.95	105_{-29}^{+192}	43.83	45.08
LH_A5	19.31	$9.4_{-3.1}^{+4.3}$	44.61	45.06
LH_A6	24.94	$6.3_{-2.4}^{+3.5}$	44.78	45.10
LH_A8	4.45	40_{-17}^{+29}	44.19	45.00
LH_A11	<1.0	...	<43.46	...
B1	<10.0	...	<44.53	...
B2	<10.0	...	<44.21	...
B3	<10.0	...	<43.89	...
B4	<10.0	...	<44.23	...
B5	<10.0	...	<44.33	...

^a Broad-band (0.3–8 keV) X-ray flux.

^b Effective column density derived from the hardness ratios assuming that the intrinsic spectrum is a power-law model with photon index Γ equal to 1.7, and Galactic N_H of 6×10^{19} cm $^{-2}$. Uncertainties reflect only the statistical errors from the observed counts and do not include uncertainties in the spectral model.

^c Absorption-corrected X-ray luminosities derived assuming the effective column density, N_H^{eff} , and an intrinsic spectrum modeled with a power-law model with photon index $\Gamma=1.7$.

Note — For more details on the X-ray data see Polletta et al. (2006). Upper limits to the X-ray fluxes correspond to 90% completeness.

absorption by gas clouds, possibly ionized, close to the nucleus that may be dust-free, and thus not contribute to any emission or absorption in the IR.

A similar comparison was presented by Shi et al. (2006) for a large compilation of AGN of different types. Instead of the apparent Si optical depth, τ_{Si} , they define the Si strength as an indicator of IR extinction. The Si strength is equivalent to $e^{-\tau_{Si}} - 1$, thus for our sources it ranges from -0.3 to -0.8 . We report their best linear fit obtained for their entire AGN sample in Fig. 7.5 after converting the Si strength to the apparent τ_{Si} . By comparing our sources with their relationship and their Fig. 3, we find that our sources occupy the lower boundary region of the Si strength- N_H relation they observe, and overlap with the most IR obscured sources in their sample which are all Seyfert 2 galaxies. Thus, the N_H and τ_{Si} of our sources are consistent with those found in other AGN, but they overlap with those observed in the most IR obscured ones. This is a consequence of our sample selection.

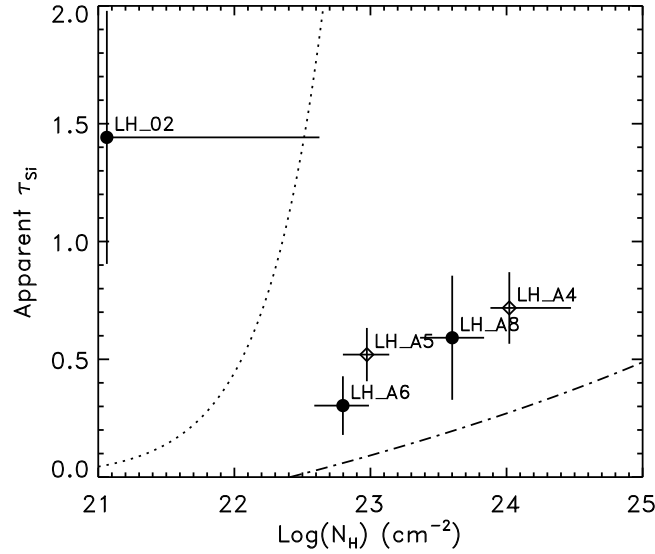


Figure 7.5.: Comparison between the apparent Si optical depth and the column density estimated from the X-ray hardness ratio. The dotted line corresponds to the expected agreement in case both absorptions occur in the same medium and assuming a Galactic gas-to-dust ratio of 100. The dashed curve corresponds to the linear fit found for a large compilation of AGN by Shi et al. (2006).

7.7. Obscuration at high luminosities

A comparison between the MIR properties of our sample with other samples from the literature shows that the selected sources can be as luminous as the most luminous MIR selected type 1 AGN in the same redshift range. The estimated ratio between obscured and unobscured AGN in our sample at these luminosities ($L_{6\mu m} \simeq 10^{45.5-46.5} \text{ erg s}^{-1}$) is about 1.5–1.9:1, and the surface density is 17–22 obscured QSOs deg^{-2} to the limits of the SWIRE survey.

However, the ratio between obscured and unobscured QSOs derived here does not correspond to the ratio between QSOs seen through the obscuring torus and those seen through the torus opening cone. Indeed, from our study, it emerges that the obscuring matter along the LOS is not always associated with the torus. Only about half (12 sources) of obscured QSOs are seen through the torus. Overall and including the unobscured AGN population, we conclude that 35–41% of MIR selected red QSOs are unobscured, 37–40% are obscured by the torus, and the remaining 23–25% are obscured, but not by the torus. These values constrain the covering factor of the torus at these extreme luminosities to be ~ 37 –40%, and the torus half opening angle, measured from the torus axis, to be $\sim 65^\circ$. This is significantly larger than the value of $\sim 45^\circ$ estimated for FIR selected Seyfert galaxies (Schmitt et al. 2001). Our results thus support the receding torus scenario, but are based on the interpretation that a large fraction of

obscured QSOs are obscured by dust detached from the torus located along or outside the torus opening cone.

The presence of foreground cold dust detached from the torus that might absorb the nuclear emission was first suggested by Keel (1980) and, subsequently supported by other studies at optical, IR, and X-ray wavelengths (Lawrence & Elvis 1982; Rigby et al. 2006; Martínez-Sansigre 2006; Brand et al. 2007). In our Galaxy, a gas-rich spiral, τ_{S_i} is estimated to be ~ 2.5 in an equatorial direction (Rieke et al. 1989). It is possible, therefore, to produce the observed obscuration with dust in a normal spiral galaxy if this host galaxy is viewed edge-on, or in a very disturbed system as a merging galaxy.

Whether the obscuring dust is in a gas-rich spiral host or in a starburst component, it clearly suggests that these extremely luminous and obscured AGN are not hosted by dust-free elliptical galaxies as commonly seen in luminous AGN in the nearby universe (e.g. Dunlop et al. 2003). The sources in this study are thus powerful AGN and they might be hosted by dusty galaxies.

The cold absorber will also absorb the nuclear X-ray emission if located along its path. Thus, we can expect that all obscured QSOs, including those obscured only by the cold absorber and those obscured by the torus, will have large column densities in the X-rays ($N_{\text{H}} > 10^{22} \text{ cm}^{-2}$). Are our predictions consistent with the findings from X-ray studies?

The lack of X-ray data for the majority of the sources in our sample does not allow us to verify that these sources are also absorbed in the X-rays. Only 5 sources have available X-ray data, and they all show large column densities ($N_{\text{H}} \geq 10^{23} \text{ cm}^{-2}$), strongly suggesting that the same might be true for all these sources. At the X-ray luminosities of our sources, $\sim 10^{45} \text{ erg s}^{-1}$, the observed ratio between X-ray absorbed and unabsorbed AGN in X-ray selected AGN samples is, unfortunately, still largely unconstrained, $\sim 0.6\text{--}1.5:1$ (e.g. Akylas et al. 2006; Tajer et al. 2007), mainly because of the difficulty of detecting absorbed sources in the X-rays. These values are lower than our predicted 1.5–1.9:1 ratio. On the other hand, when the selection effects against absorbed sources are minimized and the spectroscopic completeness is maximized, the absorbed to unabsorbed fraction can be as high as 2.5:1 (Wang et al. 2007). This ratio is tending more into the direction of our estimates.

Instead of adding the cold absorber, an alternative way to reproduce the observed SEDs is to include an additional dusty component to reproduce the observed NIR emission. The spectrum of this NIR component must decline steeply above $\sim 8 \mu\text{m}$, and thus have a very narrow range of temperatures $> 700 \text{ K}$. This NIR component could be produced by direct emission from warm dust around the AGN and not associated with the torus, e.g. in the narrow line region (Efstathiou & Rowan-Robinson 1995; Ruiz et al. 2000; Axon 2001), but models do not usually reproduce the high temperatures as observed in our sample (Groves et al. 2006). A more viable origin for this hot dust component might be scattered light in the NIR. This last hypothesis requires the presence of optically thin dust in the NLR which scatters the nuclear NIR emission into the LOS (Pier & Krolik 1993; Efstathiou & Rowan-Robinson 1995). This scenario, initially suggested by theoretical works (Pier & Krolik 1993; Efstathiou & Rowan-Robinson 1995), is also supported by speckle interferometric NIR observations of the Seyfert 2 galaxy NGC 1068 (Weigelt et al. 2004). Reconstructed K -band images show

that the nuclear emission is extended parallel to the outflow and jet direction, instead of perpendicular as expected for the torus. Observations in polarized light would be necessary to test this scenario for our objects. Other possible explanations are a more complex geometry, or a different extinction curve.

7.8. Summary and Conclusions

In this work, we modeled the IR SEDs and IRS spectra of a sample of 21 MIR selected red AGN at $z=1.3-3.0$ with extreme MIR luminosities ($\nu L_\nu(6\ \mu\text{m}) \simeq 10^{46}\ \text{erg s}^{-1}$) with the goal of investigating the properties of their obscuring matter and dependence on luminosity. The sample was drawn from the three largest *Spitzer* surveys (SWIRE, NDWFS, & FLS) by means of their extremely red infrared colors and presence of a *Si* absorption feature in their IRS spectra. Eighteen sources clearly show the *Si* absorption feature with various optical depths (see Fig. 7.1 and Table 7.3). In the remaining three sources, the *Si* absorption is only tentatively observed.

The obscured sources are as MIR luminous as the most luminous mid-infrared selected type 1 AGN currently known at similar redshifts, but are characterized by *Si* optical depths typical of ULIRGs and Seyfert 2 galaxies, that are usually less luminous MIR sources. The presented sample thus covers a new parameter space in the $L(\text{MIR})-\tau_{Si}$ region.

The observed SEDs and spectra are fit with our clumpy torus models. In 11 objects, the models produce a good fit to the data with the torus axis at inclination $\theta \geq 45^\circ$ from the LOS, consistent with the expectations from AGN unification models (e.g. Antonucci 1993). One of the sources with a weak *Si* feature is also well fit by a simple torus model, but with inclination $\theta=30^\circ$. The remaining nine sources are not well fit by a simple torus model, but they require an additional component of cold dust to reproduce the depth of the *Si* feature. The additional component is characterized by large optical depths ($\tau_V^{CA}=4-25$). Seven of the sources fit with the additional cold absorber are characterized by tori at low inclination angles, $\theta = 0-30^\circ$. The low inclination angles are required by the observed NIR emission which implies a view of the hottest dust components in the inner parts of the torus. Even though all sources show the *Si* feature in absorption, we conclude from the modeling that there is no preferred torus inclination in our sample such that these obscured sources have been selected because they are observed through the torus.

The best-fit models indicate that a compact non-flaring torus is preferred by the majority of the sources. The torus emission region is compact (more concentrated towards the nucleus) with the NIR emission being mainly due to dust in the vicinity of the nucleus. The preferred non-flaring torus in the majority of these luminous sources is consistent with the predictions of the receding torus models (e.g. Simpson 2005; Hönig & Beckert 2007).

Deep ($\tau_{Si} \geq 1.0$) *Si* features, usually observed in ULIRGs and now for the first time in our sample of obscured QSOs, indicate the presence of optically thick material along the LOS. According to the modeling presented in Sect. 7.4, we find that the obscuring matter responsible for the deep *Si* absorption is associated with either the torus or with detached foreground dust.

Based on an estimate of the surface density of unobscured QSOs derived from MIR luminosity functions (Brown et al. 2006), and of obscured QSOs derived from a color-selected sample of IR sources, the estimated surface densities are about 17-22 deg^{-2} for the obscured QSO population and 11.7 deg^{-2} for the unobscured QSOs at $z=1.3-3.0$. The estimated ratio between obscured and unobscured AGN at these luminosities ($L(6\mu m) \simeq 10^{45.5-46.5} \text{ ergs}^{-1}$) and redshift range is, thus, $\sim 1.5-1.9$. Overall we find that $\sim 35-41\%$ of MIR selected red AGN are unobscured, 23-25% are obscured but not by the torus, and the remaining 37-40% by the torus. These values constrain the torus half opening angle, measured from the torus axis, to be $\sim 65^\circ$. This value is significantly larger than found for FIR selected samples of AGN at lower luminosity ($\sim 45^\circ$ Schmitt et al. 2001), supporting the receding torus scenario.

8. Summary of the thesis and outlook

The aim of this PhD thesis was to gain further insight into the nature of AGN dust tori, which are a cornerstone of the unification scheme of AGN. For that, a 3-dimensional radiative transfer model of clumpy dust tori has been developed. With this model, it is possible to physically interpret photometric and interferometric data of AGN. The model has been applied to the prototypical type 2 AGN NGC 1068 (approximately edge-on torus), a sample of Seyfert 1 AGN (approximately face-on torus), and to the recently discovered type 2 counterparts of the luminous QSOs. In the following, the work for this PhD thesis is summarized and an outlook for future work is given.

Clumpy torus model. A new method has been developed to model the near- and mid-infrared emission of AGN with a 3-dimensional clumpy torus model using Monte Carlo simulations. In a first step, the radiation fields of individual clouds are calculated at various distances from the AGN, accounting for direct illumination by the AGN and heating by diffuse radiation from surrounding clouds. In a second step, these clouds are distributed within the torus region and their emission is added to the final torus spectrum as seen by the observer. The properties of the individual clouds and their distribution within the torus are determined from a theoretical approach of self-gravitating clouds close to the shear limit in a gravitational potential. It has been demonstrated that clumpiness in AGN tori can overcome the problems of moderate silicate features and the relatively blue NIR colors, which has been a general issue with smooth dust torus models.

Outlook: The clumpy torus models proved a powerful tool to study AGN dust tori and test the unification scheme. On the basis of the now available code, the models can be further developed. As a near-future project, the treatment of the diffuse radiation field will be improved as suggested in Sect. 2.5.3. Due to the results from the type 1 objects, different dust chemistry and grain sizes will be included in the code. This also concerns possible chemical segregation within the individual clouds and the torus. For that, new cloud data bases have to be simulated using the Monte Carlo code. As a long-term project, it is interesting to investigate if more powerful Computers will allow us to simulate clumpy tori with small volume filling factors completely with Monte Carlo methods. In addition, the gas component of the torus should be included in future, which requires 3-dimensional radiative transfer simulations of lines (mainly atomic and molecular Hydrogen) in addition to the dust continuum.

NGC 1068. The torus model was applied to high-spatial resolution photometric and interferometric IR observations of the NGC 1068 nucleus. With the clumpy torus, it was possible to simultaneously reproduce the SED and interferometry in the NIR and MIR. In particular, the clumpy torus model follows the trend of deeper silicate absorp-

tion features at larger baselines, as observed in the $8 - 13 \mu\text{m}$ range with VLTI/MIDI. It was also shown that the high visibility observed with VLTI/VINCI in the K -band ($V = 0.4 \pm 0.1$) can be the result of a clumpy structure inside the torus. Other possibilities for interpreting the high K -band visibility involve contamination by a Synchrotron source or the accretion disk which are directly seen through “holes” in the torus. This was studied by using the multi-wavelength SED of NGC 1068 in the Radio and IR regimes. It was shown that the accretion disk and possible free-free emission from a source close to the center are disfavored as possible K -band contributors, while Synchrotron emission seen through the clumpy torus is still possible. Nevertheless, Radio emission components are most likely too weak to account for the unresolved MIR flux of VLTI/MIDI observations at the longest baselines.

Outlook: NGC 1068 is the primary object for GTO observations on AGN with the VLTI/AMBER instrument. With these observations, the big gap in the K -band visibilities between 6 m and 42 m can be closed. This will provide further insight into the structure of the torus, and allows us to test the origin of the high VINCI visibility. In addition, an exploratory project in P80 aims for using the VLT/NACO instrument as a Speckle camera with Laser Guide Star assistance on NGC 1068. If successful, it will open a new window for interferometric torus studies with the VLT.

Dust tori in Seyfert 1 AGN. Radio-quiet type 1 AGN have been studied to quantify how much of the observed NIR emission originates from the torus and what fraction is contributed by the accretion disk. Archival HST/NICMOS J , H , and K -band observations have been used to compare observed NIR colors with expectations for black-body radiation and more realistic clumpy torus models. It has been shown that in the sample objects, the accretion disk contribution is $\lesssim 25\%$ of the total K -band flux, so that the torus dominates the overall emission in this wavelength band. This result is important for planned interferometric observations with VLTI/AMBER (or the second-generation VLTI instrument VSI) which aim for resolving dust tori in the NIR. In addition, it was found that dust sublimation temperatures significantly larger than 1500 K are disfavored by the observed NIR colors. This is in agreement with theoretical considerations of dust evaporation, but poses some problems for inner torus radii as observed by NIR reverberation mapping which favors smaller radii or higher temperatures. A possible solution to this problem might be the presence of large carbon grains at small distances from the AGN.

Outlook: Sample studies of nearby Seyfert 1 and 2 AGN appear to be a useful tool to learn more about the physics of the tori and their role in feeding the AGN, provided that the angular resolution is high enough. By comparing low-spatial resolution mid-infrared *Spitzer* spectra with those from the VLT/VISIR instrument, we want to test which spatial scales are necessary to obtain “true” torus spectra where contributions from, e.g., starbursts are negligible. A pilot project on three Seyfert 2 AGN has already shown that with VISIR, scales of $\lesssim 100$ pc can be reached (for an example, see Fig. 8.1). This project will be extended to type 1 objects and a larger sample of nearby AGN. By modeling the dust continuum and silicate features of type 1 and 2 objects, we will gain further insight into the chemical composition of the tori.

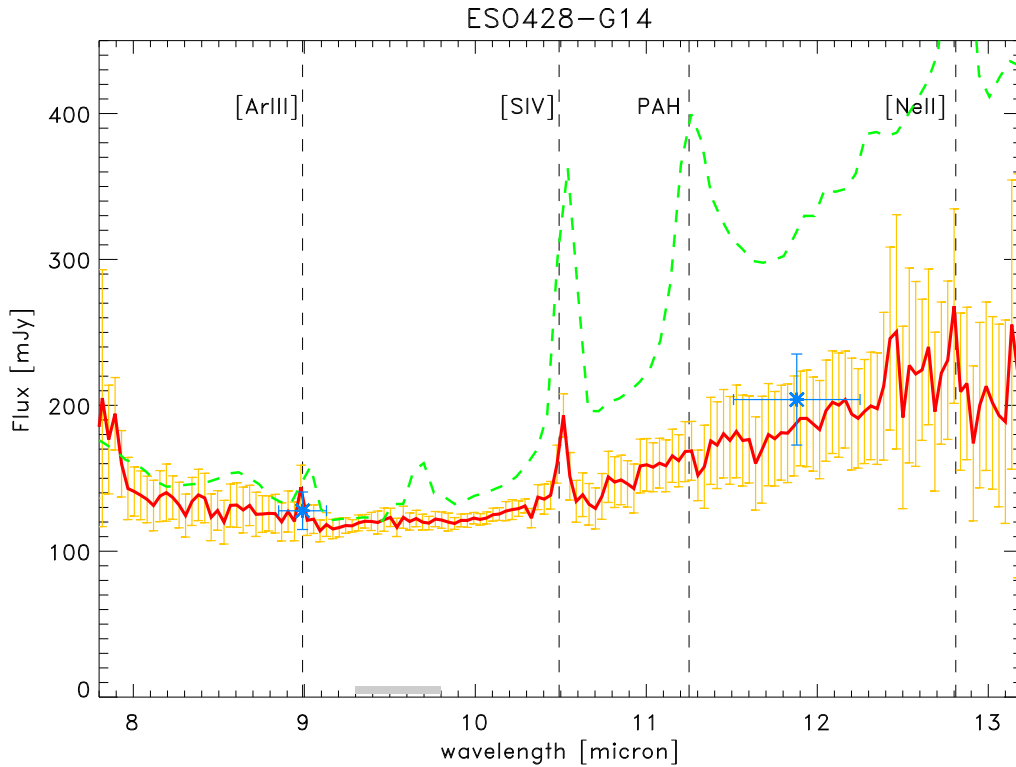


Figure 8.1.: Comparison between the 8 – 13 μm nuclear spectrum of the Seyfert 2 AGN ESO 428–G14 as observed with VLT/VISIR (red) and *Spitzer* (green). This preliminary result shows that the common starburst signatures (here: 11.3 μm PAH line and the [NeII] line at 12.8 μm) disappear at the resolution of the VLT, which suggests that the remaining emission is mainly coming from the dust torus.

AGN feedback mechanism on the dust torus. In a theoretical work, a physically motivated clumpy torus model was used to study the influence of the strong UV/optical radiation from the accretion disk on the dust in the torus. It was shown that due to the radiation pressure on the dust grains, accretion through the torus becomes very inefficient if the dust is smoothly distributed in the torus. On the other hand, clumpy tori can provide the necessary matter supply to feed the accretion disk since the clouds efficiently compensate the radiation pressure acting on the dust. With these results, criteria for the existence of clumpy dust tori were derived using the accretion scenario as presented by Beckert & Duschl (2004). For low luminosities, the torus is expected to change its appearance in the range of $\lesssim 10^{42} \text{ erg s}^{-1}$ where it is supposed to resemble a circumnuclear disk as observed in the center of our Galaxy. At high luminosities in the QSO regime, the torus can start to disappear since large clouds become unbound in the torus, depending on the actual Eddington rate of the AGN. It was shown that for large Eddington ratios, this effect can explain the apparently “receding torus” since more type 1 objects are expected.

The nature of obscuration in type 2 QSOs. Recently, obscured QSOs – the “missing link” in the AGN unification scheme – have been found by several X-ray surveys with *XMM-Newton*, *Chandra*, and *Spitzer*. By using *Spitzer*, it was possible to establish rest-frame near-to-mid-IR SEDs of these objects. The clumpy torus model has been used to interpret SEDs of a sample of 21 QSO2s. For several of these objects, the observed blue NIR-colors seem to be inconsistent with the deep silicate features at $9.7\ \mu\text{m}$. By using the model results, it was proposed that a second dust component can act as an additional cold absorber in the type 2 QSOs. Thus, it is possible that the tori are seen face on (= blue NIR color), while a cold absorber in the host galaxy produces deep silicate features. This is similar to local Seyfert AGN where galactic dust lanes can provide significant obscuration of the nuclear emission.

Outlook: In this work, it was possible to compare observations and torus models in highly obscured QSOs. Even though this represents a novelty with respect to previous studies, it is evident that the models require more tests, additional components, and some refinements. Here, a cold absorber component was added to act as foreground absorption. A more detailed analysis of the observational signatures that suggest such a component would be necessary to test our hypothesis. In addition, its geometrical and physical properties should be investigated by modeling its emission and absorption in relation with the radiation field of an AGN, a starburst, and a host galaxy. This kind of analysis will soon be possible thanks to high signal-to-noise IRS spectra of some of the sources presented here that will be obtained during Spitzer cycle 4 (Proposals 40398 and 40793).

A. Radiation in a Dusty Medium

The torus models aim for simulating the radiative transfer in a dusty and clumpy medium. Here, some basics on the radiative transfer will be provided, following the description of Unsöld & Baschek (2005).

A.1. Radiative Transfer Equations

An infinite small ray of light with intensity I_ν is crossing a volume element dV . Due to the medium inside the volume element, the ray of light experiences extinction on its path ds through the medium,

$$\frac{dI_\nu}{ds} = -k_\nu I_\nu, \quad (\text{A.1})$$

where k_ν is the extinction coefficient of the medium. The extinction is a combination of scattering and absorption, so that $k_\nu = \sigma_\nu + \kappa_\nu$, where σ_ν is the scattering coefficient and κ_ν is the absorption coefficient. At the same time, the volume element dV adds the energy dE_ν into the spectral interval $[\nu, \nu + d\nu]$ to the ray by emission into solid angle $d\Omega$,

$$dE_\nu = j_\nu d\nu dV d\Omega. \quad (\text{A.2})$$

Here, j_ν is the emission coefficient of the medium. Thus, we can write for the total change in intensity of the ray when it travels a finite distance ds ,

$$\frac{dI_\nu}{ds} = -k_\nu I_\nu + j_\nu. \quad (\text{A.3})$$

If the ray of light crosses a non-emitting layer of matter (i.e. $j_\nu = 0$), Eqn. (A.3) can be easily solved, so that we obtain

$$I_\nu = I_0 \exp(-\tau_\nu) \quad (\text{A.4})$$

where $\tau_\nu = \int_0^s k_\nu ds$ is the optical depth of the medium. Eqn. (A.4) is the basis for the ray-tracing of individual cloud emission through the clumpy torus.

A.2. Absorption and thermal re-emission of dust

Let us consider a dust grain which is in local thermal equilibrium. This situation was introduced in Sect. 1.4. As already shown in Eqn. (1.3), energy conservation for the absorbed and re-emitted radiation (local thermal equilibrium) requires

$$\pi a^2 \int Q_{\text{abs}}(\nu) F_\nu^+(r) d\nu = 4\pi a^2 \int Q_{\text{abs}}(\nu) \pi B_\nu(T) d\nu. \quad (\text{A.5})$$

In this notation, $B_\nu(T)$ is the Planck function, which reads

$$B_\nu(T) = \frac{2h\nu^3}{c^2} \frac{1}{\exp(h\nu/(k_B T)) - 1}, \quad (\text{A.6})$$

where c is the speed of light, h is the Planck constant, and k_B the Boltzmann constant. Eqs. (A.3) & (A.5) describe the principle of the radiative transfer problem within a dust cloud which is solved with the Monte Carlo code.

The frequency, ν_{\max} , of maximum emission of the Planck function B_ν can be obtained from its derivative, giving Wien's law

$$\frac{\nu_{\max}}{10^{14} \text{ Hz}} = \frac{T}{1700 \text{ K}}, \quad (\text{A.7})$$

or, for the wavelength λ by using the corresponding function B_λ and replacing $d\lambda = -(c/\nu^2) d\nu$,

$$\left(\frac{\lambda_{\max}}{1 \mu\text{m}} \right)^{-1} = \frac{T}{2900 \text{ K}}. \quad (\text{A.8})$$

Bibliography

- Akylas, A., Georgantopoulos, I., Georgakis, A., Kitsionas, S., Hatziminaoglou, E. 2006, *A&A*, 459, 693
- Alonso-Herrero, A., Quillen, A. C., Simpson, C., Efstathiou, A., Ward, M. J. 2001, *AJ*, 121, 1369
- Alonso-Herrero, A., Pérez-González, P. G., Alexander, D. M., et al. 2006, *ApJ*, 640, 167
- Axon, D. J. 2001, in *Astronomical Society of the Pacific Conference Series*, Vol. 249, *The Central Kiloparsec of Starbursts and AGN: The La Palma Connection*, ed. J. H. Knapen, J. E. Beckman, I. Shlosman, & T. J. Mahoney, 193
- Antonucci, R. R. J., & Miller, J. S. 1985, *ApJ*, 297, 621
- Antonucci, R. 1993, *ARA&A*, 31, 473
- Barger, A. J., Cowie, L. L., Mushotzky, R. F., et al. 2005, *ApJ*, 129, 578
- Barvainis, R. 1987, *ApJ*, 320, 537
- Barvainis, R., 1992, *ApJ*, 400, 502
- Beckert, T., Duschl, W. J., Mezger, P. G., Zylka, R. 1996, *A&A*, 307, 450
- Beckert, T., & Duschl, W. J. 2004, *A&A*, 426, 445
- Beckert, T. 2005, *MmSAI*, 76, 150
- Bjorkman, J. E., & Wood, K. 2001, *ApJ*, 554, 615
- Bock, J. J., Neugebauer, G., Matthews, K., Soifer, B. T., Becklin, E. E., et al. 2000, *AJ*, 120, 2904
- Brand, K., Dey, A., Desai, V., et al. 2007, *ApJ*, 663, 204
- Brandl, B. R., Bernard-Salas, J., Spoon, H. W. W., et al. 2006, *ApJ*, 653, 1129
- Brown, M. J. I., Brand, K., Dey, A., et al. 2006, *ApJ*, 638, 88
- Camenzind, M. 1995, *Reviews of Modern Astronomy*, 8, 201
- Capetti, A., Macchetto, F., Axon, D. J., Sparks, W. B., Boksenberg, A. 1995, *ApJ*, 452, L87

- Chiar, J. E., Adamson, A. J., Whittet, D. C. B., et al. 2006, *ApJ*, 651, 268
- Davies, R., Mueller Sanchez, F., Genzel, R., et al. 2007, *ApJ*, in press (astro-ph/0704.1374)
- Desai, V., Armus, L., Soifer, B. T., et al. 2006, *ApJ*, 641, 133
- Draine, B. T., & Lee, H. M. 1984, *ApJ*, 285, 89
- Dressel, L. L., Tsvetanov, Z. I., Kriss, G. A., Ford, H. C. 1997, *Ap&SS*, 248, 85
- Dullemond, C. P., & van Bemmell, I. M. 2005, *A&A*, 436, 47
- Dunlop, J. S., McLure, R. J., Kukula, M. J., et al. 2003, *MNRAS*, 340, 1095
- Efstathiou, A., & Rowan-Robinson, M. 1994, *MNRAS*, 266, 212
- Efstathiou, A., & Rowan-Robinson, M. 1995, *MNRAS*, 273, 649
- Elitzur, M., & Shlosman, I. 2006, *ApJ*, 648, L101
- Elvis, M., Wilkes, B., McDowell, J., et al. 1994, *ApJS*, 95, 1
- Emmering, R. T., Blandford, R. D., Shlosman, I. 1992, *ApJ*, 385, 460
- Fazio, G. G., Hora, J. L., Allen, L. E., et al. 2004, *ApJS*, 154, 10
- Francis, P. J., Hewett, P. C., Foltz, C. B., et al. 1991, *ApJ*, 373, 465
- Frank, J., King, A., Raine, D. 1992, *Accretion Power in Astrophysics*, 2nd edition, Cambridge University Press
- Galliano, E., Pantin, E., Alloin, D., Lagage, P. O. 2005, *MNRAS*, 363, L1
- Gallimore, J. F., Baum, S. A., O'Dea, C. P., Pedlar, A. 1996, *ApJ*, 464, 198
- Gallimore, J. F., Baum, S. A., O'Dea, C. P. 2004, *ApJ*, 613, 794
- Gaskell, C. M., Goosmann, R. W., Antonucci, R. R. J., Whyson D. H., 2004, *ApJ*, 616, 147
- Glass, I. S. 2004, *MNRAS*, 350, 1049
- Gliozzi, M., Sambruna, R. M., Foschini, L. 2007, *ApJ*, 662, 878
- Goodman, J. 2003, *MNRAS*, 339, 937
- Gonzalez-Solares, E. A., Perez-Fournon, I., Rowan-Robinson, M., et al. 2005, *MNRAS*, 358, 333
- Granato, G. L., & Danese, L. 1994, *MNRAS*, 268, 235
- Granato, G. L., Danese, L., Franceschini, A. 1997, *ApJ*, 486, 147

- Grimes, J. A., Rawlings, S., Willott, C. J. 2004, MNRAS, 349, 503
- Groves, B., Dopita, M., Sutherland, R. 2006, A&A, 458, 405
- Greenhill, L. J., Gwinn, C. R., Antonucci, R., Barvainis, R. 1996, ApJ, 472, L21
- Güsten, R., Genzel, R., Wright, M. C. H., et al. 1987, ApJ, 318, 124
- Guhathakurta, P., & Draine, B. T. 1989, ApJ, 345, 230
- Hao, L., Spoon, H. W. W., Sloan, G. C., et al. 2005, ApJ, 625, L75
- Hao, L., Weedman, D. W., Spoon, H. W. W., et al. 2007, ApJ, 655, L77
- Hasinger, G. 2004, Nucl. Phys. B Proc. Supp., 132, 86
- Hasinger, G., Miyaji, T., Schmidt, M. 2005, A&A, 441, 417
- Higdon, S. J. U., Devost, D., Higdon, J. L., et al. 2004, PASP, 116, 975
- Hines, D. C., & Wills, B. J. 1995, ApJ, 448, L69
- Hönig, S. F., Beckert, T., Ohnaka, K., Weigelt, G. 2006, A&A, 452, 459
- Hönig, S. F., Beckert, T., Ohnaka, K., Weigelt, G. 2007, ASPC, 373, 487 (Conference proceedings “The Central Engine of Active Galactic Nuclei”, ed. L. C. Ho and J.-M. Wang, San Francisco: ASP)
- Hönig, S. F., & Beckert, T. 2007, MNRAS, 380, 1172
- Horst, H., Smette, A., Gandhi, P., Duschl, W. J. 2006, A&A, 457, L17
- Houck, J. R., Roellig, T. L., van Cleve, J. et al. 2004, ApJS, 154, 18
- Houck, J. R., Soifer, B. T., Weedman, D., et al. 2005, ApJ, 622, L105
- Huffman, D. R. 1977, AdPhy, 26, 129
- Imanishi, M., Dudley, C. C., Maiolino, R., et al. 2007, ApJS, 171, 72
- Ivezić, Ž., Nenkova, M., Elitzur, M. 1999, User Manual for DUSTY, Univ. of Kentucky internal report, accessible at <http://www.pa.uky.edu/~moshe/dusty/>
- Jaffe, W., Meisenheimer, K., Röttgering, et al. 2004, Nature, 429, 47
- Jaffe, W., Talk at the conference “The Central Engines of AGN”, Xian (China), http://agn06.ihep.ac.cn/main/presentations/Jaffe_agn06.ppt
- Kaspi, S., Smith, P. S., Netzer, H., et al. 2000, ApJ, 533, 631
- Keel, W. C. 1980, AJ, 85, 198
- Keel, W. C. 1983, ApJ, 269, 466

- Kennicutt, R. C. 1992, *ApJS*, 79, 255
- Khachikian, E. Y., & Weedman, D. W., 1974, 192, 581
- Kinkhabwala, A., Sako, M., Behar, E., Kahn, S. M., Paerels, F., et al. 2002, *ApJ*, 575, 732
- Kishimoto, M. 1999, *ApJ*, 518, 676
- Kishimoto, M., Antonucci, R., Blaes, O. 2005, *MNRAS*, 364, 640
- Kishimoto, M., Hönl, S. F., Beckert, T., Weigelt, G. 2007, *A&A*, 476, 713
- Kobayashi, Y., Sato, S., Yamashita, T., Shiba, H., Takami, H. 1993, *ApJ*, 404, 94
- Krips, M., Eckart, A., Neri, R., et al. 2006, *A&A*, 446, 113
- Krist J. E., Golimowski D. A., Schroeder D. J., Henry T. J., 1998, *PASP*, 110, 1046
- Krolik, J. H. 2007, *ApJ*, 661, 52
- Krolik, J. H. & Begelman, M. C. 1988, *ApJ*, 329, 702
- Kukula, M. J., Dunlop, J. S., McLure, R. J, et al. 2001, *MNRAS*, 326, 1533
- Lacy, J. H., Malkan, M., Becklin, E. E., et al., 1982, *ApJ*, 256, 75
- Lacy, M., Storrie-Lombardi, L. J., Sajina, A. et al. 2004, *ApJS*, 154, 166
- Lacy, M., Petric, A. O., Sajina, A., et al. 2007, *AJ*, 133, 186
- Laor, A., & Draine, B. T. 1993, *ApJ*, 402, 441
- La Franca, F., Fiore, F., Comastri, A., et al. 2005, *ApJ*, 635, 864
- Lawrence, A., & Elvis, M. 1982, *ApJ*, 256, 410
- Lawrence, A. 1991, *MNRAS*, 252, 586
- Lawrence, C. R., Zucker, J. R., Readhead, A. C. S., et al. 1996, *ApJS*, 107, 541
- Levenson, N. A., Heckman, T. M., Krolik, J. H., Weaver, K. A., Życki, P. T. 2006, *ApJ*, 648, 111
- Levenson, N. A., Sirocky, M. M., Hao, L. et al. 2007, *ApJ*, 654, L45
- Lohmann, A.W., Weigelt, G., Wirtitzer, B 1983, *Appl. Opt.*, 22, 4028
- Lonsdale, C. J., Smith, H. E., Rowan-Robinson, M., et al. 2003, *PASP*, 115, 897
- Lonsdale, C., Polletta, M. d. C., Surace, J., et al. 2004, *ApJS*, 154, 54
- Lutz, D., Maiolino, R., Spoon, H. W. W., Moorwood, A. F. M. 2004, *A&A*, 418, 465
- Lutz, D., Yan, L., Armus, L., et al. 2005, *ApJ*, 632, L13

- Maiolino, R. & Rieke, G. H. 1995, *ApJ*, 454, 95
- Maiolino, R., Marconi, A., Salvati, M., et al. 2001a, *A&A*, 365, 28
- Maiolino R., Marconi A., Oliva E., 2001b, *A&A*, 365, 37
- Manske, V., Henning, T., Men'shchikov, A. B., *A&A*, 331, 52
- Marco, O., & Alloin, D. 2000, *A&A*, 353, 465
- Marco, O., & Brooks, K. J. 2003, *A&A*, 398, 101
- Marconi, A. et al. 2004, *MNRAS*, 351, 169
- Martínez-Sansigre, A., Rawlings, S., Lacy, M. et al. 2005, *Nature*, 436, 666
- Martínez-Sansigre, A., Rawlings, S., Lacy, M. et al. 2006, *MNRAS*, 370, 1479
- Mathis, J. S., Rumpl, W., Nordsieck, K. H. 1977, *ApJ*, 217, 425
- McLure, R. J. & Dunlop, J. S. 2001, *MNRAS*, 327, 199
- Minezaki, T., Yoshii, Y., Kobayashi, Y., et al. 2004, *ApJ*, 600, L35
- Murray, S. S., Kenter, A., Forman, W. R., et al. 2005, *ApJS*, 161, 1
- Natta, A., & Panagia, N. 1984, *ApJ*, 287, 228
- Nenkova, M., Ivezić, Ž., Elitzur, M. 2002, *ApJ*, 570, L9
- Netzer, H. 1985, *MNRAS*, 216, 63
- Neugebauer G., Green R. F., Matthews K., et al. 1987, *ApJS*, 63, 615
- Ohnaka, K., Driebe, T., Hofmann, K.-H., et al. 2006, *A&A*, 445, 1015
- Owen, F. N., O'Dea, C. P., Keel, W. C. 1990, *ApJ*, 352, 44
- Ohsluga, K. & Umemura, M. 1999, *ApJ*, 521, L13
- Osterbrock, D. E. 1981, *ApJ*, 249, 462
- Osterbrock, D. E., & Martel, A. 1993, *ApJ*, 414, 552
- Pelletier, G. & Pudritz, R. E. 1992, *ApJ*, 394, 117
- Peng, C. Y., Ho, L. C., Impey, C. D., Rix, H.-W. 2002., *AJ*, 124, 266
- Perola, G. C., Puccetti, S., Fiore, F., et al. 2004, *A&A*, 421, 491
- Pier, E. A., & Krolik, J. H. 1992, *ApJ*, 401, 99
- Pier, E. A., & Krolik, J. H. 1993, *ApJ*, 418, 673
- Pier, E. A., Antonucci, R., Hurt, T., Kriss, G., Krolik, J. 1994, *ApJ*, 428, 124

- Polletta, M., Wilkes, B. J., Siana, B., et al. 2006, *ApJ*, 642, 673
- Polletta, M., Weedman, D., Höning, S. F., et al. 2007, *ApJ*, in press (astro-ph/0709.4458)
- Prieto, M. A., Meisenheimer, K., Marco, O., et al. 2004, *ApJ*, 614, 135
- Pringle, J. E. 1996, *MNRAS*, 281, 357
- Quillen, A. C. 2001, *ApJ*, 563, 313
- Reuter, H.-P., Lesch, H. 1996, *A&A*, 310, L5
- Rieke, G. H., Rieke, M. J., Paul, A. E. 1989, *ApJ*, 336, 752
- Rieke, G. H., Young, E. T., Engelbracht, C. W., et al. 2004, *ApJS*, 154, 25
- Rigby, J. R., Rieke, G. H., Donley, J. L., Alonso-Herrero, A., Pérez-González, P. G. 2006, *ApJ*, 645, 115
- Risaliti, G., Elvis, M., Fabbiano, G., Baldi, A., Zezas, A. 2005, *ApJ*, 623, L93
- Risaliti, G., Elvis, M., Fabbiano, G., et al. 2007, *ApJ*, 623, L93
- Rouan, D., Rigaut, F., Alloin, D., et al. 1998, *A&A*, 339, 687
- Roy, A. L., Colbert, E. J. M., Wilson, A. S., Ulvestad, J. S. 1998, *ApJ*, 504, 147
- Ruiz, M., Alexander, D. M., Young, S., et al. 2000, *MNRAS*, 316, 49
- Sajina, A., Yan, L., Armus, et al. 2007, *ApJ*, 704, 713, in press (astro-ph/0704.1765)
- Salpeter, E. E. 1977, *ARA&A*, 15, 267
- Sanders, D. B., Phinney, E. S., Neugebauer, G., et al. 1989, *ApJ*, 347, 29
- Sanders, D. B., & Mirabel, I. F. 1996, *ARA&A*, 34, 749
- Schartmann, M., Meisenheimer, K., Camenzind, M., Wolf, S., Henning, T. 2005, *A&A*, 437, 861
- Schinnerer, E., Eckart, A., Tacconi, L. J., Genzel, R., Downes, D. 2000, *ApJ*, 533, 850
- Schmitt, H. R., Antonucci, R. R. J., Ulvestad, et al. 2001, *ApJ*, 555, 663
- Schödel, R., Ott, T., Genzel, R., et al. 2003, *ApJ*, 596, 1015
- Scoville, N. Z., Evans, A. S., Thompson, R., et al. 2000, *AJ*, 119, 991
- Semenov, D., Henning, T., Helling C., et al. 2003, *A&A*, 410, 611
- Seyfert, C. K. 1943, *ApJ*, 97, 28
- Shakura, N. I., & Sunyaev, R. A. 1973, *A&A*, 24, 337
- Shi, Y., Rieke, G. H., Hines, D. C., et al. 2006, *ApJ*, 653, 127

- Siebenmorgen, R., Haas, M., Krügel, E., Schulz, B. 2005, *A&A*, 436, L5
- Silva, L., Granato, G. L., Bressan, A., Danese, L. 1998, *ApJ*, 509, 103
- Simpson, C. 2005, *MNRAS*, 360, 565
- Sitko, M. L., Sitko, A. K., Siemiginowska, A., Szczerba, R., 1993, *ApJ*, 409, 139
- Spergel, D. N., Verde, L., Peiris, H. V., et al. 2003, *ApJS*, 148, 175
- Spitzer, L., 1978, *Physical processes in the interstellar medium*, Wiley-Interscience, New York
- Spoon, H. W. W., Armus, L., Cami, J., et al. 2004, *ApJS*, 154, 184
- Suganuma, M., Yoshii, Y., Kobayashi, Y., et al., 2006, *ApJ*, 639, 46
- Sturm, E., Lutz, D., Tran, D., et al. 2000, *A&A*, 358, 481
- Sturm, E., Schweitzer, M., Lutz, D., et al. 2005, *ApJ*, 629, L21
- Sturm, E., Hasinger, G., Lehmann, I., et al. 2006, *ApJ*, 642, 81
- Suchkov, A., Krist, J. 1998, Instrument Science Report NICMOS 98-018
- Surace, J. A., Shupe, D. L., Fang, F., et al. 2005, Spitzer Science Center, California Institute of Technology
- Swain, M., Vasisht, G., Akeson, R., et al. 2003, *ApJ*, 596, L163
- Tajer, M., Polletta, M., Chiappetti, L., et al. 2007, *A&A*, 467, 73
- Tozzi, P., Gilli, R., Mainieri, V., et al. 2006, *A&A*, 451, 457
- Tomita, H., Yoshii, Y., Kobayashi, Y., et al. 2006, *ApJ*, 652, L13
- Tomono, D., Doi, Y., Usuda, T., Nishimura, T. 2001, *ApJ*, 557, 637
- Treister, E., & Urry, C. M. 2006, *ApJ*, 652, L79
- Tristram, K., PhD thesis, Heidelberg 2007
- Ueda, Y., Akiyama, M., Ohta, K., Miyaji, T. 2003, *ApJ*, 598, 886
- Unsöld, A., & Baschek, B., “Der neue Kosmos”, 7th edition, Springer Verlag, Heidelberg 2005
- Urrutia, T., Lacy, M., Gregg, M. D., Becker, R. H. 2005, *ApJ*, 627, 75
- Urry, C. M., & Padovani, P. 1995, *PASP*, 107, 803
- Veilleux, S., Kim, D.-C., Peng, C. Y., et al. 2006, *ApJ*, 643, 707
- Véron-Cetty M.-P., Véron P., 2006, *A&A*, 455, 773

- Vollmer, B., Beckert, T., Duschl, W. J. 2004, *A&A*, 413, 949
- Wada, K. & Norman, C. A. 2002, *ApJ*, 566, L21
- Wang, J. X., Jiang, P., Zheng, Z. Y., et al. 2007, *ApJ*, 657, 95
- Weedman, D. W., Polletta, M., Lonsdale, C. J., et al. 2006, *ApJ*, 653, 101
- Weedman, D. W., Le Floch, E., Higdon, S. J. U., Higdon, J. L., Houck, J. R. 2006b, *ApJ*, 638, 613
- Weedman, D. W., Soifer, B. T., Hao, L., et al. 2006c, *ApJ*, 651, 101
- Weigelt, G. 1977, *Optics Comm.*, 21, 55
- Weigelt, G., Wittkowski, M., Balega, et al. 2004, *A&A*, 425, 77
- Weinberger, A. J., Neugebauer, G., Matthews, K. 1999, *AJ*, 117, 2748
- Wilkes, B. J., Schmidt, G. D., Cutri, R. M., et al. 2002, *ApJ*, 564, L65
- Winkler, H., Glass, I. S., van Wyk, F., et al. 1992, *MNRAS*, 257, 659
- Wittkowski, M., Balega, Y., Beckert, T., et al. 1998, *A&A*, 329, L45
- Wittkowski, M., Kervella, P., Arsenault, R., et al. 2004, *A&A*, 418, L39
- Wolf, S. 2003, *ApJ*, 582, 859
- Woo, J.-H., & Urry, C. M. 2002, *ApJ*, 579, 530
- Wu H., Zou Z. L., Xia X. Y., Deng Z. G., 1998, *A&AS*, 132, 181
- Yan, L., Sajina, A., Fadda, D., et al. 2007, *ApJ*, 658, 778
- Young, A. J., Wilson, A. S., Shopbell, P. L. 2001, *ApJ*, 556, 6

This research has made use of the NASA/IPAC Extragalactic Database (NED) which is operated by the Jet Propulsion Laboratory, California Institute of Technology, under contract with the National Aeronautics and Space Administration.

Curriculum Vitae

Name: Sebastian Florian Hönig
Current Affiliation: Max-Planck-Institut für Radioastronomie,
Auf dem Hügel 69, 53121 Bonn

Education

1985 – 1989 Schiller-Grundschule, Eislingen, Germany
1989 – 1998 Erich Kästner Gymnasium, Eislingen, Germany
1998 Abitur
1999 – 2001 Undergraduate studies in physics,
Ruprecht-Karls-Universität Heidelberg, Germany
2001 *Vordiplom* in Physics
2001 – 2004 Graduate studies in physics,
Ruprecht-Karls-Universität Heidelberg, Germany
2004 *Diplom* in Physics
since 2004 PhD student,
Rheinische Friedrich-Wilhelms-Universität, Bonn, in
the IR Interferometry department, Max-Planck-
Institut für Radioastronomie

Research and Teaching

Teaching, 2001 – 2003 Teaching assistant for undergraduate mathematics,
Ruprecht-Karls-Universität Heidelberg
Observations, 2004 Survey for Transneptunian Objects with the 2.2 m
telescope at La Silla, Chile
Diploma thesis, 2004 *Stability in the Multiple Stellar System θ^1 Ori*, Insti-
tut für Theoretische Astrophysik, Heidelberg; Advi-
sor: Prof. Werner Tscharnuter
PhD research, 2004 – 2007 *Clumpy Dust Tori in Active Galactic Nuclei*, Max-
Planck-Institut für Radioastronomie, Bonn; Advisor:
Prof. Gerd Weigelt
Research, since 2006 Private Near-Earth Asteroid survey in the Southern
hemisphere with a 0.36 m telescope on Tahiti
Observations, 2007 VLTI/MIDI Mid-infrared interferometry of the AGN
NGC 7582, Paranal, Chile

Acknowledgments

Some people deserve particular reference. Their help and support was invaluable for the work on this PhD thesis.

Foremost, I would like to thank **Prof. Dr. Gerd Weigelt** for giving me the opportunity, encouragement, and support to work in his group in this very challenging field of research.

I am grateful that **Prof. Dr. Wolfgang Duschl** made the contact to the group in Bonn and helped with suggestions and advise throughout the work on this thesis.

My special thanks go to **Dr. Thomas Beckert** who introduced me to the field of AGN and advised me in all of the projects. His help and patience was priceless.

Many thanks to **Prof. Dr. Pavel Kroupa** for agreeing to be co-referee, as well as **Prof. Dr. Karl Maier** and **Prof. Dr. Clemens Simmer** for being member of the examination committee.

I greatly appreciate the help of **Dr. Keiichi Ohnaka** who provided me with his Monte Carlo code `mc_Sim` and quickly implemented changes whenever I was asking.

I am indebted to **Dr. Makoto Kishimoto**, **Dr. Maria Polletta**, and **Dr. Almudena Prieto** for excellent collaborations. In particular, I would like to thank Maria for inviting me to work on the remarkable type 2 QSOs, Makoto for his suggestions which significantly improved the models, and Almudena for the inspiring discussions on NGC 1068.

Hannes Horst and **Dr. Thomas Beckert** took the burden to thoroughly read the thesis and providing helpful comments.

Several people helped me with fruitful discussions and suggestions. In particular, I would like to thank **Hannes Horst**, **Mark Schartmann**, **Alain Smette**, **Alina Streblyanska**, and **Konrad Tristram**.

Many thanks go to all the people in the group for the nice working atmosphere. I enjoyed the regular coffee chatting with Bérengère, Claudia, Florentin, Nicolas, Peter, Stefan, Sven, and all the others, which was a pleasant distraction.

Finally, life's nothing without family and friends. I want to thank my parents and grandparents for their invaluable, incessant support on my way, as well as Mareike, Katja, Alex, Hannes, Thomas, and Marc for joining my journey.